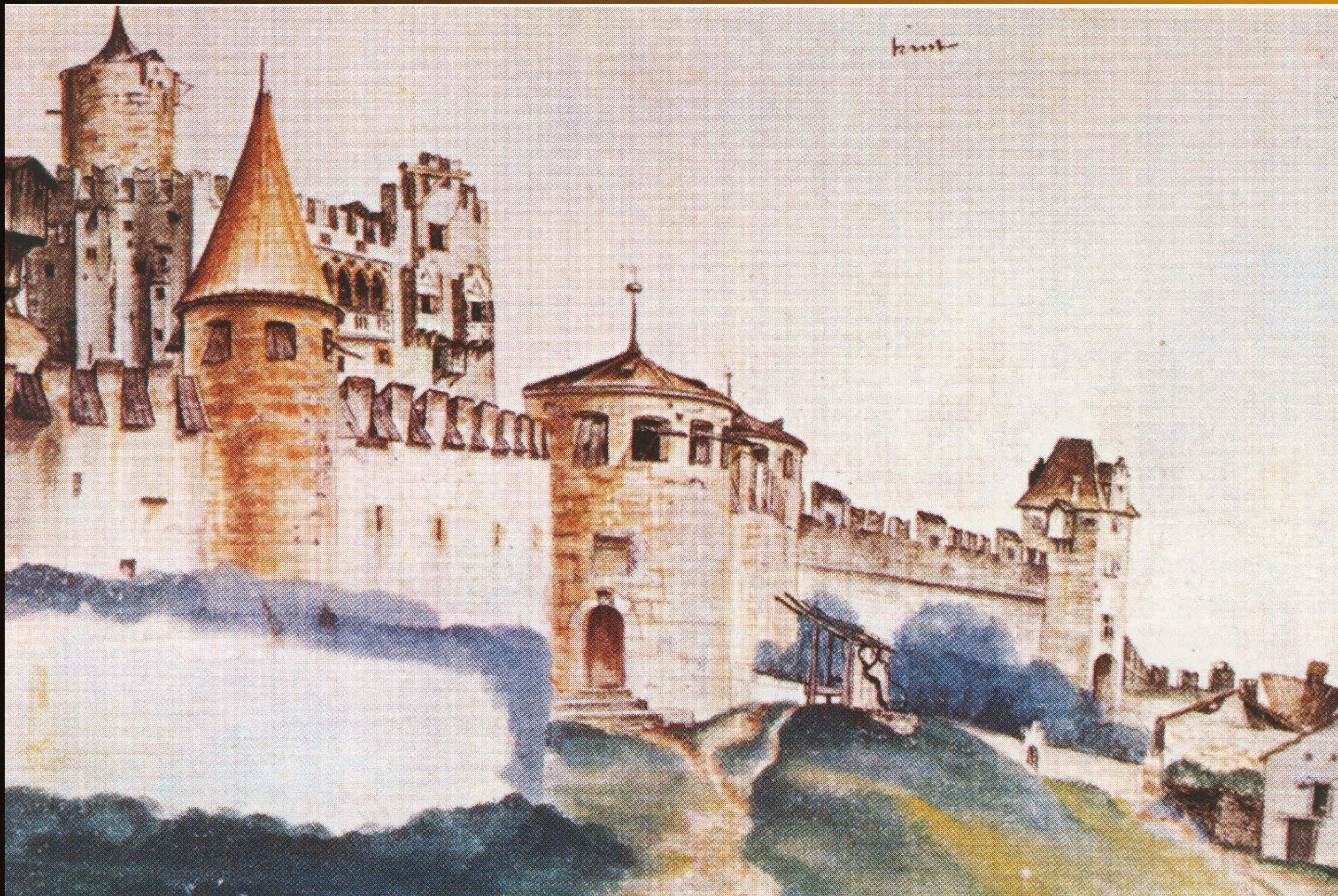




Istituto Nazionale di Fisica Nucleare
LABORATORI NAZIONALI DI FRASCATI

FRASCATI PHYSICS SERIES



LFC22: Strong interactions from QCD
to new strong dynamics at LHC and
Future Colliders

Albrecht Dürer, 1494

**ECT*, TRENTO, ITALY,
AUGUST 29 - SEPTEMBER 2, 2022**

Editors:

Gennaro Corcella, Aldo Deandrea, Stefania De Curtis,
Stefano Moretti, Giulia Pancheri, Roberto Tenchini, Marcel Vos

FRASCATI PHYSICS SERIES

Series Editor

Antonella Antonelli

Technical Editor

Lia Sabatini

Cover by Elisa Santinelli

Volume LXXIII

Istituto Nazionale di Fisica Nucleare – Laboratori Nazionali di Frascati

Divisione Ricerca

Ufficio Biblioteca e Pubblicazioni Scientifiche

P.O. Box 13, I-00044 Frascati Roma Italy

email: library@lists.lnf.infn.it

Copyright © 2022 by INFN

All rights reserved. No part of this publication may be reproduced, stored in a retrieval system or transmitted in any form or by any means, electronic, mechanical, photocopying, recording or otherwise, without the prior permission of the copyright owner.

ISBN 978-88-86409-75-9

**LFC22: Strong interactions from QCD to new
strong dynamics at LHC and Future Colliders**

August 29 - September 2, 2022

CONTENTS

<i>T. Strebler</i>	ATLAS and CMS Physics prospects for High-Luminosity LHC	1
<i>S. Sasikumar</i>	Physics at future linear colliders	7
<i>G. Gaudio</i>	Physics studies at FCC-ee	16
<i>L. Lopez-Honorez, Q. Decant, S. Junius, M.H.G. Tytgat</i>	Dark matter from WIMP to FIMP over three regimes: Cosmology versus Colliders	22
<i>A. Caliva</i>	Highlights of experimental results on heavy-ion physics from ALICE	28
<i>G. Manco</i>	Color sensitive variables for $H \rightarrow b\bar{b}$ tagger	34
<i>G. Stagnitto</i>	Initial-state QED radiation at NLL accuracy for future electron-positron colliders	41
<i>F. Giuli</i>	High precision QCD physics at FCC-ee	47
<i>A. Ghira</i>	Non commutativity between massless and threshold limit in processes with heavy quarks	53
<i>M. Procura</i>	Weighing the top with energy correlators	60
<i>C. Brønnum-Hansen, J. Quarroz, C. Signorile-Signorile, Chen-Yu Wang</i>	Non-factorisable corrections to t -channel single-top production: comparing results for the LHC and FCC	67
<i>R. Aoude</i>	Top pair entanglement in the SMEFT	73
<i>M. Vollmann</i>	Resummation of large electroweak terms for indirect dark matter detection	79
<i>S. Kulkarni</i>	QCD-like strongly interacting dark matter at colliders	87
<i>R. Garani</i>	Phases of condensed dark matter with a Yukawa interaction	94
<i>M. Benzke, T. Hurth</i>	Recent progress on the nonlocal power corrections to the inclusive penguin decays $B \rightarrow X_s \gamma$ and $B \rightarrow X_s \ell\ell$	101
<i>L. Bianchini</i>	Precision measurement of the W boson mass: status and prospects	109

ATLAS and CMS Physics prospects for High-Luminosity LHC

Thomas Strebler

CPPM, Aix-Marseille Université, CNRS/IN2P3, Marseille, France

Abstract

With a start of data-taking scheduled in 2029, the High-Luminosity LHC (HL-LHC) will extend the LHC program to the first half of the 2040's with pp collisions at $\sqrt{s} = 14$ TeV, with an expected integrated luminosity of 3000 fb^{-1} for each of the ATLAS and CMS experiments. Their physics programme will directly benefit from the large luminosity to be collected, improved systematic uncertainties as well as from new trigger and reconstruction techniques made possible thanks to the detector Phase-2 upgrades. The most recent physics prospects from the ATLAS and CMS collaborations are summarized in this contribution, covering in particular Higgs physics, Standard Model precision measurements and Beyond the Standard Model searches.

1 Introduction

The High-Luminosity LHC (HL-LHC) is expected to operate from 2029, with an instantaneous luminosity up to $7.5 \text{ cm}^{-2}\text{s}^{-1}$ and an average number of inelastic proton collisions per bunch crossing ($\langle\mu\rangle$) up to 200, compared to a peak instantaneous luminosity around $2.0 \text{ cm}^{-2}\text{s}^{-1}$ and $\langle\mu\rangle$ up to 55 achieved during the 2022 LHC run. Those data-taking conditions will present unprecedented challenges for the ATLAS and CMS detectors, motivating ambitious detector upgrade programmes ^{1, 2)}, aimed at guaranteeing equivalent or better performance as during the previous LHC runs.

In order to improve the assessment of the physics potential of the HL-LHC dataset and to identify in advance potential limiting factors requiring dedicated efforts, the ATLAS and CMS collaborations are regularly updating prospect physics results for various key HL-LHC analyses. Comprehensive studies of the HL-LHC physics potential were published in 2019 (CERN Yellow Report ³⁾ for the European Strategy update) and in 2022 (Snowmass Energy Frontier Report ⁴⁾ and ATLAS and CMS White

Paper ⁵⁾). Those projections highlight in particular the impact of the 20-fold increase in integrated luminosity (\mathcal{L}) with respect to the Run-2 dataset, which will significantly improve the sensitivity of statistically-limited measurements, with statistical uncertainties reducing as $1/\sqrt{\mathcal{L}}$. In addition, as an increasing amount of measurements will be limited by the systematic uncertainties, an effort to determine realistic HL-LHC estimates for those uncertainties has also been carried out. In the baseline scenario, theory uncertainties are in particular expected to be scaled down by a factor two, both for cross-section and modeling uncertainties, thanks to improved fixed-order calculations and Monte Carlo generators. In addition, uncertainties related to the limited size of Monte-Carlo simulation samples should become negligible, relying on the expected software improvements. Some experimental uncertainties will also be improved thanks to the large HL-LHC dataset, in particular for the statistical components of the uncertainties derived from auxiliary measurements in data, and the luminosity uncertainty is expected to reach 1% for the full HL-LHC dataset.

2 Higgs physics

In the Higgs sector, the HL-LHC dataset will be the opportunity to improve the precision of the measurements of the Higgs boson couplings to other Standard Model (SM) particles, illustrated in Fig. 1a). Couplings to gauge bosons and third-generation fermions are in particular expected to be measured with a precision better than 4%, getting limited by the theory uncertainties. Couplings to second-generation fermions will also be probed with good precision, offering more insight on the structure of the Higgs Yukawa couplings. Higgs boson mass measurements are also expected to reach an unprecedented precision, down to 30 MeV in the $H \rightarrow 4\ell$ channel ⁷⁾, and will start getting limited by systematics uncertainties. Higgs Simplified Template Cross-Sections (STXS) and other differential measurements will also be carried to constrain the kinematics of the Higgs boson and provide model-independent measurements which can be compared to predictions from various physics models. For those measurements, systematics will also start playing an important role, except at high transverse momentum or for sub-dominant modes.

One of the key measurements to be carried at HL-LHC concerns the Higgs self-coupling, which will improve our understanding of the Higgs potential and of the electroweak symmetry breaking. The main sensitivity for this measurement will be provided through the search for di-Higgs (HH) production, complemented by constraints from single-Higgs measurements. The latest combined ATLAS and CMS projection ³⁾, covering several HH channels, was highlighting an expected 4σ significance for the observation of the HH production and a 50% uncertainty for the Higgs self-coupling modifier. Since then, updated projections from ATLAS and CMS, benefiting from improvements developed in the context of Run 2 analyses, have been released ⁵⁾. Those updated numbers bring strong confidence that a 5σ observation could be achieved combining 3000 fb^{-1} datasets from ATLAS and CMS.

3 Standard Model

Beyond the study of the Higgs sector, the ATLAS and CMS physics programmes for HL-LHC encompass many precision measurements related to the electroweak sector, top quark properties, QCD or B -physics. The combination of such measurements as inputs for Standard Model Effective Field Theory global fits ⁸⁾ could then shed light on some potential deviations from the SM predictions associated with Beyond-the-Standard-Model (BSM) particles beyond the mass scales accessible with the LHC.

Vector boson scattering (VBS) processes are quite sensitive to potential BSM effects, in particular

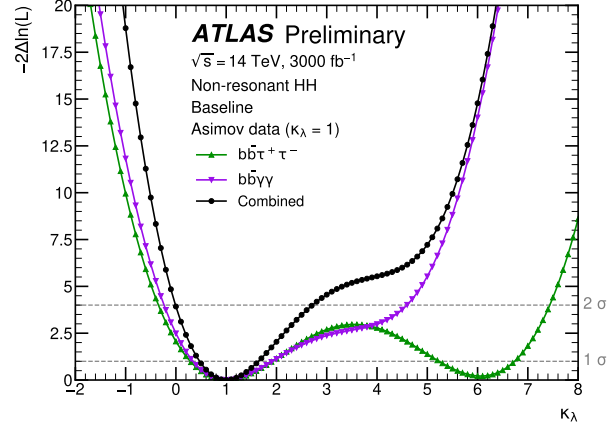
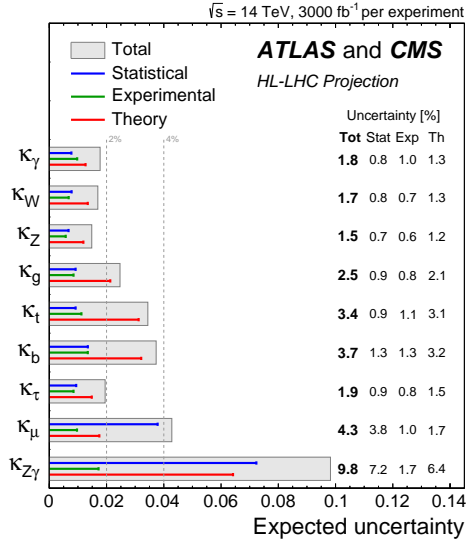


Figure 1: *a) Expected uncertainties on the Higgs coupling modifier parameters (κ), for the combination of ATLAS and CMS HL-LHC extrapolations ³⁾. *b) Likelihood distributions as a function of the Higgs self-coupling modifier κ_λ for the latest ATLAS HL-LHC projection of the $HH \rightarrow b\bar{b}\tau^+\tau^-$ and $HH \rightarrow b\bar{b}\gamma\gamma$ results and their combination ⁶⁾.**

for the case of longitudinally-polarized vector bosons. In the SM, this process is unitarized thanks to the presence of Higgs boson contributions, and deviations from this would indicate the presence of BSM physics. The cross-section for the longitudinally-polarized state is small (6-7% of the total cross-section), making this a challenging but important part of the HL-LHC physics program. Based on several sets of projection results ⁵⁾, a combination of ATLAS and CMS data, whose sensitivity is driven by leptonic final states, is expected lead to an observation of the same-sign longitudinal WW scattering at HL-LHC, illustrated in Fig. 2a).

Precision electroweak measurements will also be carried at HL-LHC. The electroweak mixing angle $\sin^2\theta_{eff}$ is for instance expected to be measured through the forward-backward asymmetry in di-lepton events with a unprecedented precision ⁵⁾. A small dataset of 1 fb^{-1} collected at low pileup could also be exploited to improve the precision of the W mass measurement ¹⁰⁾, benefiting in particular from the improved PDF determination expected with the HL-LHC dataset, as illustrated in Fig. 2b). An uncertainty as small as 5 MeV could thus be achieved. As for the top quark, the best precision in its mass measurement is expected to be achieved through the kinematic reconstruction of lepton+jets $t\bar{t}$ events, with a precision of 170 MeV on the MC mass parameter dominated by theoretical modeling uncertainties. Alternative methods, impacted by different systematic uncertainties, could further improve the precision of this measurement when combined ¹¹⁾. Finally, measurements of the top-quark pole mass, better defined theoretically, can be achieved thanks to $t\bar{t}$ cross-section measurements and could reach an uncertainty better than 500 MeV ¹²⁾.

Precision measurements in the QCD sector will also represent major components of the HL-LHC physics programme. Thanks to the large amount of events collected, the reach of differential jet and photon cross-section measurements will be significantly increased, which will directly benefit to the determination of proton PDFs, since large differences can be observed between different PDF predictions

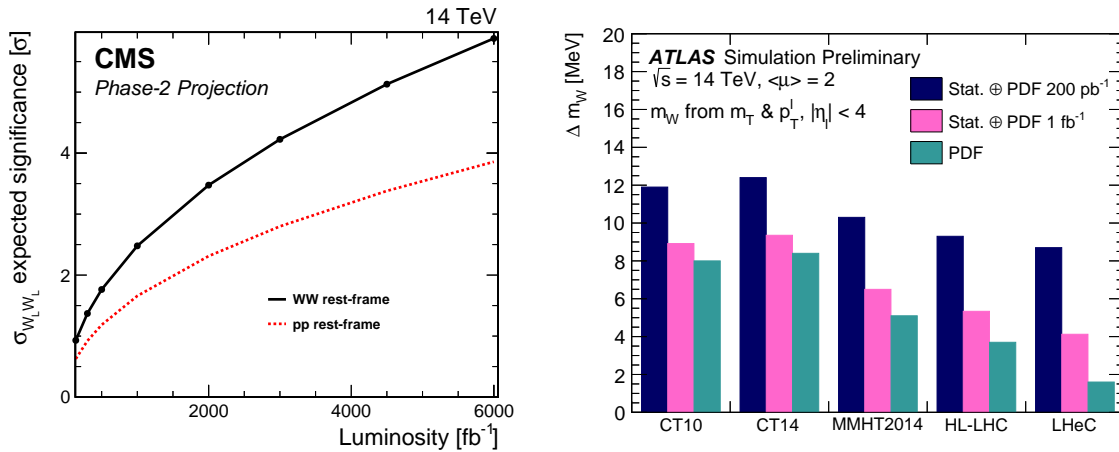


Figure 2: a) *Expected significance for the VBS $W_L^\pm W_L^\pm$ process as a function of the integrated luminosity obtained with the latest CMS projection* ⁹⁾. b) *W mass measurement uncertainty expected by ATLAS for 200 pb⁻¹ and 1 fb⁻¹ of low pileup data collected at $\sqrt{s} = 14$ TeV, for difference PDF predictions and uncertainties* ¹⁰⁾.

at high p_T ¹³⁾. The precision of the gluon PDFs will also be strongly improved thanks to differential $t\bar{t}$ cross-section measurements ¹⁴⁾.

4 Beyond the Standard Model

An important set of BSM projection results from ATLAS and CMS, covering a large variety of scenarios, has been summarized in ⁵⁾ and a small selection of those results is presented here. Among all of the existing BSM models, many predict heavy resonances manifesting as high-mass excesses in the tail of invariant mass distributions. Those can for instance correspond to heavy gauge bosons, excited leptons or heavy Majorana neutrinos. The corresponding searches will be continued at HL-LHC, with the best sensitivities typically achieved in leptonic channels. Thanks to the increase in the center-of-mass energy and the large luminosity, HL-LHC will improve the sensitivity of those searches towards weaker couplings and higher masses, as illustrated in Fig. 3a) with limits expected to reach 7 TeV for Z' bosons predicted in the Sequential Standard Model ¹⁵⁾.

Run 2 Supersymmetry (SUSY) searches have already set stringent limits on squark and gluino production in scenarios with large mass differences between the SUSY particles. On the other hand, processes with smaller cross-sections, like the production of electroweakinos, will directly benefit from the large HL-LHC dataset. New analysis techniques can also significantly boost the sensitivity of scenarios with compressed mass spectrum. The new capabilities offered by the Phase-2 detector upgrades and dedicated reconstruction algorithms will also benefit to the searches for long-lived particles, predicted in a wide range of BSM models. The sensitivity to long-lived dark photons decaying into muons and produced in Higgs boson decays ¹⁶⁾, which can be improved thanks to optimized new muon trigger algorithms, is for instance illustrated in Fig. 3b).

Dark matter (DM) searches will also be carried over a large variety of final states. As DM particles are not expected to interact with the detector, those searches are typically targeting production modes in

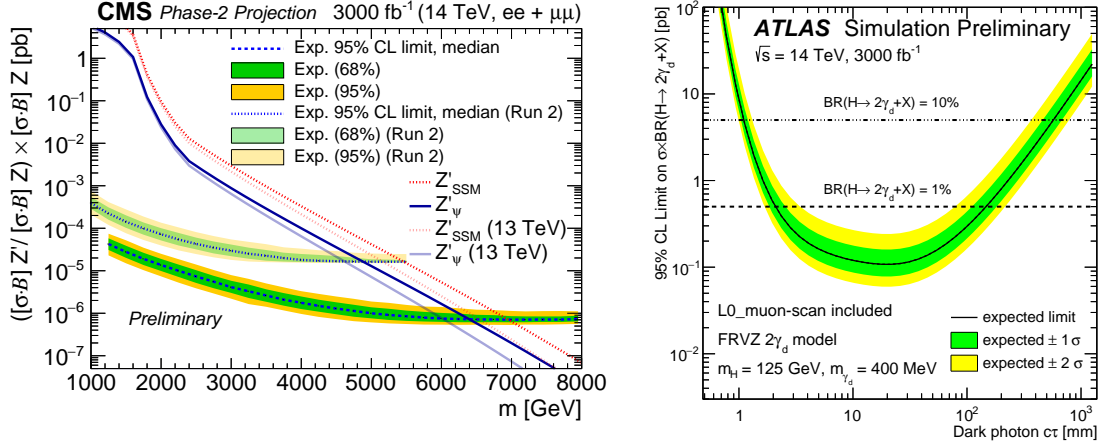


Figure 3: a) *Expected limits in the search for a heavy Z' boson for the full CMS HL-LHC dataset, compared to the expected limits for the CMS Run 2 analysis* ¹⁵⁾. b) *Expected HL-LHC ATLAS limits in the search for dark photons decaying into muons, through $H \rightarrow 2\gamma_d + X$ decays as a function of the γ_d lifetime, considering 45% dark photon branching ratio to muons* ¹⁶⁾.

association with SM detectable particles, where the DM presence can be inferred through a large amount of missing transverse energy. Interpretations are often carried in simplified models, with a BSM boson coupling to SM particles and decaying into DM particles. For those searches as well, large improvements are expected thanks to the large HL-LHC dataset and complementary limits with respect to direct detection experiments can be derived ¹⁷⁾.

5 Conclusion

The HL-LHC data-taking will represent an unprecedented challenge for the ATLAS and CMS experiments, considering the major detector upgrades scheduled, the updates required to face the large pile-up in the object reconstruction and identification algorithms and the huge amount of data to be analysed, all of this to be prepared in parallel to the Run 3 data-taking. A major effort from the collaborations has therefore been initiated to make this a success, as some strong positive impact is expected for their physics programmes. The sensitivity of HL-LHC analyses will in particular directly benefit from the large 3000 fb^{-1} luminosity expected to be collected by each experiment, the improved systematic uncertainties and the new trigger and reconstruction techniques possible thanks to the detector upgrades. Thanks to those improvements, the properties of the Higgs boson and other Standard Model properties will be measured with an unprecedented precision, while searches for BSM scenarios will be able to probe unexplored regions of phase space, either at high mass or in challenging final states. Flavor and heavy-ion physics, unfortunately not covered in this report, will also represent a large fraction of the new physics results expected during the HL-LHC phase.

References

1. CMS Collaboration, CMS Phase II Upgrade Scope Document, CERN-LHCC-2015-019
2. ATLAS Collaboration, ATLAS Phase-II Upgrade Scoping Document, CERN-LHCC-2015-020
3. A. Dainese et al., Report on the Physics at the HL-LHC, and Perspectives for the HE-LHC, CERN Yellow Report CERN-2019-007
4. M. Narain et al., The Future of US Particle Physics - The Snowmass 2021 Energy Frontier Report, FERMILAB-FN-1219-PPD-T
5. ATLAS and CMS Collaborations, Snowmass White Paper Contribution: Physics with the Phase-2 ATLAS and CMS Detectors, ATL-PHYS-PUB-2022-018, CMS PAS FTR-22-001
6. ATLAS Collaboration, Projected sensitivity of Higgs boson pair production combining the $b\bar{b}\gamma\gamma$ and $b\bar{b}\tau^+\tau^-$ final states with the ATLAS detector at the HL-LHC, ATL-PHYS-PUB-2022-005
7. CMS Collaboration, Projection of the Higgs boson mass and on-shell width measurements in $H \rightarrow ZZ^* \rightarrow 4\ell$ decay channel at the HL-LHC, CMS-PAS-FTR-21-007
8. J. de Blas et al., Global SMEFT Fits at Future Colliders, arXiv:2206.08326 [hep-ph]
9. CMS Collaboration, Prospects for the measurement of vector boson scattering production in leptonic $W^\pm W^\pm$ and WZ diboson events at $\sqrt{s} = 14$ TeV at the High-Luminosity LHC, CMS-PAS-FTR-21-001
10. ATLAS Collaboration, Prospects for the measurement of the W -boson mass at the HL- and HE-LHC, ATL-PHYS-PUB-2018-026
11. CMS Collaboration, ECFA 2016: Prospects for selected standard model measurements with the CMS experiment at the High-Luminosity LHC, CMS-PAS-FTR-16-006
12. R. Schwienhorst et al., Report of the Topical Group on Top quark physics and heavy flavor production for Snowmass 2021, arXiv:2209.11267 [hep-ph]
13. ATLAS Collaboration, Prospects for jet and photon physics at the HL-LHC and HE-LHC, ATL-PHYS-PUB-2018-051
14. CMS Collaboration, Projection of differential $t\bar{t}$ production cross section measurements in the e/μ +jets channels in pp collisions at the HL-LHC, CMS-PAS-FTR-18-015
15. CMS Collaboration, Sensitivity projections for a search for new phenomena at high dilepton mass for the LHC Run 3 and the HL-LHC, CMS-PAS-FTR-21-005
16. ATLAS Collaboration, Search prospects for dark-photons decaying to displaced collimated jets of muons at HL-LHC, ATL-PHYS-PUB-2019-002
17. ATLAS Collaboration, ATLAS sensitivity to dark matter produced in association with heavy quarks at the HL-LHC, ATL-PHYS-PUB-2018-036

PHYSICS AT FUTURE LINEAR COLLIDERS

Swathi Sasikumar

Max-Planck-Institute for Physics, Munich

Abstract

The International Linear Collider (ILC) and the Compact Linear Collider (CLIC) are the two proposed e^+e^- linear colliders operating at different centre-of-mass energies and with at least one of the beams polarised. The experiments at these facilities provide a platform to perform high-precision measurements of Standard Model observables and searches for new particles complementing the HL-LHC programme. In this contribution, different studies of the two linear colliders are discussed. Experiments at linear e^+e^- colliders, with a relatively clean environment compared to hadron colliders, can perform precision measurements of electroweak and Higgs boson and top quark production processes. In this contribution, the focus is on the analysis of single Higgs production, double Higgs production, and top-Yukawa coupling.

1 Introduction

In the history of particle physics, e^+e^- colliders have played complementary roles in shedding light on to the properties of elementary particles. The prediction of top mass at LEP experiments had a key role in helping discover the top quark at Tevatron in the predicted mass range ^{1, 2)}. Similarly, the discovery of gluon at PETRA ^{3, 4)}, precise measurement of Z boson at LEP and the SLC ⁵⁾ have made very important contributions to particle physics. After the discovery of Higgs boson at the LHC experiments ⁶⁾, an e^+e^- collider can perfectly compliment the hadron collider to make precision measurements of the Higgs boson. Moreover, at higher energies, an e^+e^- collider can provide an environment to make precise measurements of top quark mass and understand top-Yukawa coupling as well as top-electroweak coupling.

The International Linear Collider (ILC) and Compact Linear Collider (CLIC) are two proposed e^+e^- linear colliders. The ILC is a 20 km (31 km for 500 GeV) machine which has a tunable centre-of-mass energy between 250-500 GeV (upgradable to 1 TeV) whereas the CLIC (50 km) can operate at a centre-of-mass energy of 380 GeV

to 3 TeV. Both the electron and positron beams are polarised for the ILC as $P(e^-) = \pm 80\%$ and $P(e^+) = \pm 30\%$. CLIC has its electron beam polarised to $\pm 80\%$. The schematic pictures of both the colliders are given in figure 1.

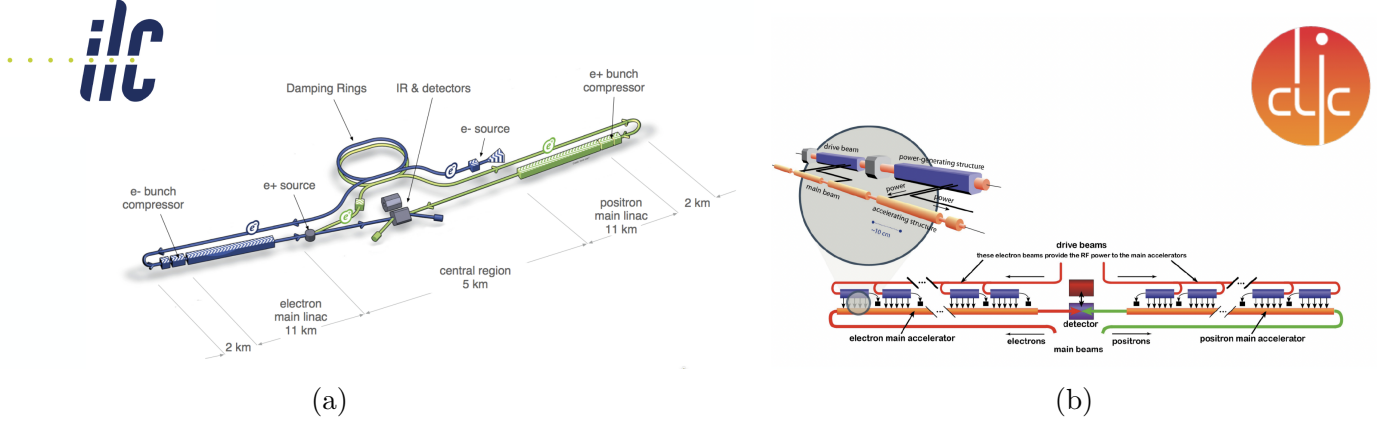


Figure 1: (a) The schematic design of the International Linear Collider for 500 GeV machine ⁷⁾. (b) The schematic design for the Compact Linear Collider ⁸⁾.

2 Advantages of a linear e^+e^- collider

Being an e^+e^- collider, ILC and CLIC mainly have electroweak production and therefore very clean physics environment. The significantly smaller amount of background allows a 'no trigger' policy on the events produced. This means, all the produced events can be included in the analysis and no sample is discarded. Moreover, the colliding particles being fundamental particles, e^+e^- colliders have a very well defined centre-of-mass energy of $\sqrt{s} = 2E_{beam}$. This allows the use of kinematic information and thus gives the opportunity to make model-independent measurements.

Linear colliders can provide access to a center-of-mass energy well above what can be reached in practical circular machines. Another important advantage of a linear collider is that the electron and positron beams can be polarised. Polarisation enables reducing the background and enhancing the signal as required. A detailed review of the benefits of beam polarisation for the physics reach of ILC can be found in ⁹⁾ and ¹⁰⁾.

3 Single Higgs Production

One of the most important analyses planned at the e^+e^- colliders is the Higgs analysis. The precise measurement of Higgs decay branching ratios is key to probing new physics in the Higgs sector. The e^+e^- colliders serve as a Higgs factory at a centre-of-mass energy of 250 GeV. Some of the important processes for the production of single Higgs can be seen in Fig. 2a. Single Higgs is produced mainly through higgstrahlung, gauge boson fusion, and top-Yukawa coupling. Higgstrahlung is found to be the dominant process around 250 GeV ¹¹⁾ whereas above 350 GeV processes like gauge boson fusion starts gaining significance.

The e^+e^- colliders have an initial state with well-defined four-momentum. This allows the identification of Higgs bosons in higgstrahlung process using the mass recoiling against an identified Z boson, without any reference to the decay products of the Higgs. At 250 GeV, ILC can produce up to half a million Higgs bosons that are completely unbiased with respect to Higgs decay. Using such a sample precise measurements of Higgs boson properties e.g. partial cross-section to different Higgs decay modes can be made. Some of these measurements

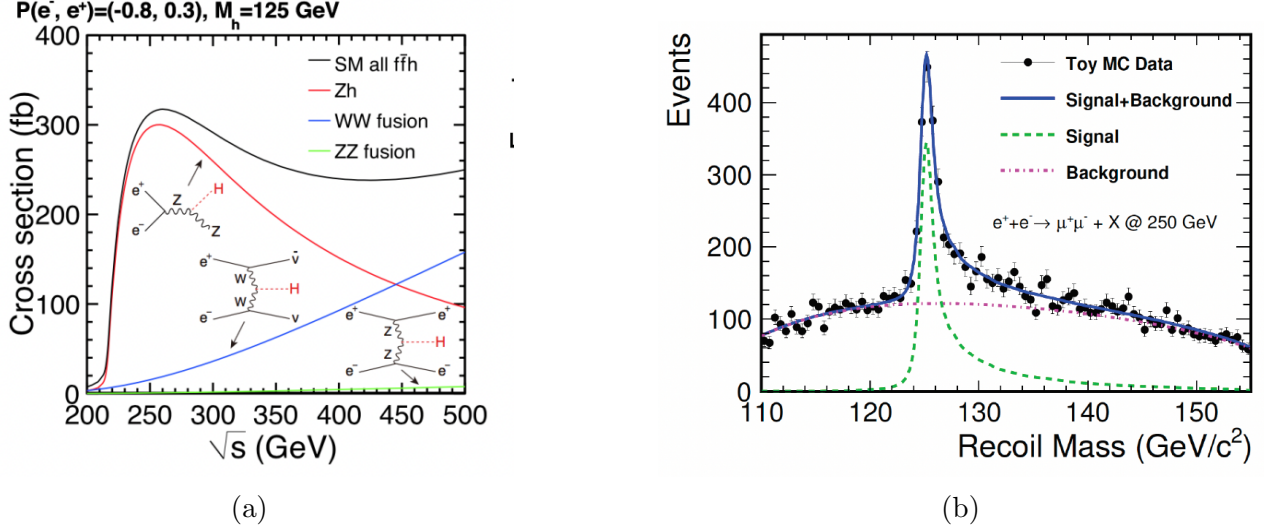


Figure 2: (a) Cross sections for major Higgs production processes as a function of center-of-mass energy ¹¹⁾. (b) Recoil mass spectrum against $Z \rightarrow \mu^+\mu^-$ for signal $e^+e^- \rightarrow ZH$ and SM background at 250 GeV ¹²⁾.

strongly depend on the Higgs boson mass which can be measured very precisely using the recoil technique. Also, since the identification of the Higgs boson does not depend on the decay mode, it is also possible to measure the total higgstrahlung production cross-section at the ILC. The recoil mass is measured as:

$$m_{rec}^2 = (\sqrt{s} - E_Z)^2 - p_z^2 \quad (1)$$

where m_{rec} is the recoil mass, \sqrt{s} is the centre-of-mass energy, E_Z and p_z is the energy and momentum of the identified Z boson. The identified Z boson in a higgstrahlung event can decay to hadrons or to charged leptons. A study for the ILC showed that for a higgstrahlung process at $\sqrt{s} = 250$ GeV and a luminosity of 2 ab^{-1} where Z decays leptonically, the precision on the HZ cross-section can be achieved as $\Delta\sigma(HZ)/\sigma(HZ) = 1.0\%$ ¹²⁾. The higgstrahlung process where Z decays hadronically have a ten times higher cross-section than the leptonic decays ¹³⁾. However, at 250 GeV, the HZ production is not far above the threshold and therefore the recoil mass distribution is relatively closer to the kinematic limit. This region is populated by processes like $e^+e^- \rightarrow qq\bar{q}\bar{q}$ (from $e^+e^- \rightarrow ZZ$ or $e^+e^- \rightarrow WW$) with large cross sections. Separation of signal from these backgrounds is very challenging especially when Higgs boson decays hadronically too. An analysis at CLIC shows the measurement of Higgs mass and precision on HZ cross section using higgstrahlung process at different centre-of-mass energies. This study shows that the best sensitivity for the precision study is obtained at 350 GeV since the HZ production is further from the threshold. This provides better separation of signal from the most challenging backgrounds. The summary of the statistical precision achievable on $\sigma(HZ)$ can be seen in table 1.

The Higgs mass can also be directly reconstructed from its decay products, providing complementary measurements. The majority of Higgs bosons decay hadronically, with the dominant branching fractions corresponding to $H \rightarrow b\bar{b}$, $H \rightarrow c\bar{c}$ and $H \rightarrow g\bar{g}$. The separation of these processes strongly relies on jet flavor tagging. The jet flavor tagging algorithm at ILC, called as LCFIplus, has achieved an excellent b- and c- tagging performance in full simulation studies of the ILDCONCEPT at ILC ¹⁶⁾. At a centre-of-mass energy $\sqrt{s} = 250$ GeV and a nominal luminosity of 2 ab^{-1} , the application of the LCFIplus algorithm to the hadronically decaying Higgs boson allows the measurement of the partial cross-section $\sigma_{ZH} \times BR(H \rightarrow b\bar{b})$ to 0.7% and $\sigma_{ZH} \times BR(H \rightarrow c\bar{c}, g\bar{g})$ to around 4 %

\sqrt{s} [GeV]	$\mathcal{L}_{\text{int}}[\text{fb}^{-1}]$	$\sigma(HZ)[\text{fb}]$	$\Delta\sigma(ZH)[\%]$
250	1000	136	2.58
350	1000	93	1.27
420	1000	68	1.86

Table 1: The statistical precision achievable on $\sigma(HZ)$ for different centre-of-mass energies ¹³⁾.

precision both the major polarization combinations ¹⁵⁾. The identification of $H \rightarrow ss$ decays presents a significant challenge due to its subtle signature and small expected branching ratio.

For the processes where Higgs decays leptonically, the measurements can be performed if the branching ratios are similar to as predicted in the Standard Model. An ILC study for a centre-of-mass energy 250 GeV showed that the partial cross-section $\sigma(ZH) \times \text{BR}(H \rightarrow \tau\tau)$ can be measured with a precision less than 2% ¹⁷⁾. However, for the $\mu\mu$ decay of Higgs, the small branching ratio of $H \rightarrow \mu\mu$ limits the statistics available at ILC. Nevertheless, the partial cross-section $\sigma(ZH) \times \text{BR}(H \rightarrow \mu\mu)$ can still be measured with a precision of 17% for combined 250 GeV and 500 GeV results ¹⁸⁾.

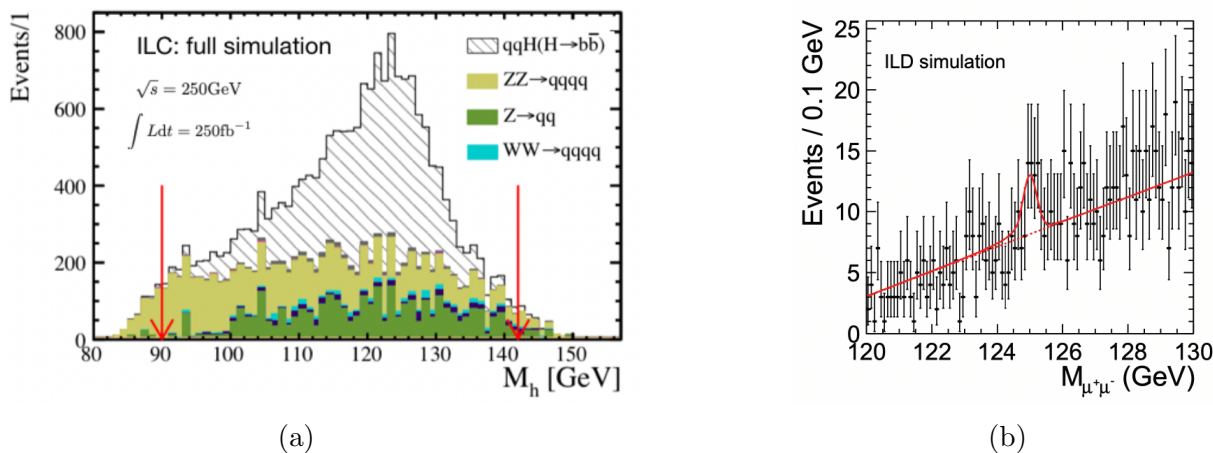


Figure 3: (a) Comparison of signal and backgrounds from ILC full simulation for the measurement of the $\sigma \times \text{BR}$ for $H \rightarrow b\bar{b}$, for 250 fb^{-1} of ILC data at 250 GeV ¹⁶⁾. (b) Data from pseudo-experiment fitted by a Gaussian to extract its mean and width ¹⁸⁾.

4 Di-Higgs production at linear lepton colliders

At a centre-of-mass energy of at least 500 GeV, the self-interaction of the Higgs boson, particularly, the triple Higgs coupling λ , can be probed directly by analysing the Higgs boson pairs. The di-Higgs production at e^+e^- colliders happen through two important processes e.g. $e^+e^- \rightarrow ZHH$ (double higgstrahlung) and $e^+e^- \rightarrow \nu\bar{\nu}HH$ (WW fusion). The cross-section for these processes as a function of the centre-of-mass energies can be seen in figure 4a.

The prospects of measuring double Higgs production through these two reactions have been studied at the ILC for data fully simulated for the ILD detector. These studies were conducted both for $\sqrt{s} = 500 \text{ GeV}$ ¹⁹⁾ and $\sqrt{s} = 1 \text{ TeV}$ ²⁰⁾. It was found that, if the Higgs self-coupling value stays as that predicted by the Standard

Model, then the double higgstrahlung can be observed at a centre-of-mass energy of 500 GeV with a significance of 8σ combining the $HH \rightarrow b\bar{b}b\bar{b}$ and $HH \rightarrow b\bar{b}WW^*$ channels. This results in the measurement of λ with a precision of 27%. With the improvements in the detector that are relevant for these measurements and with the inclusion of $HH \rightarrow \tau^+\tau^-b\bar{b}$ it has been estimated that the precision on λ can be improved to 21-22%¹⁹⁾. Also, the inclusion of double Higgs production from WW fusion at 1 TeV can improve the relative precision on λ to 10%.

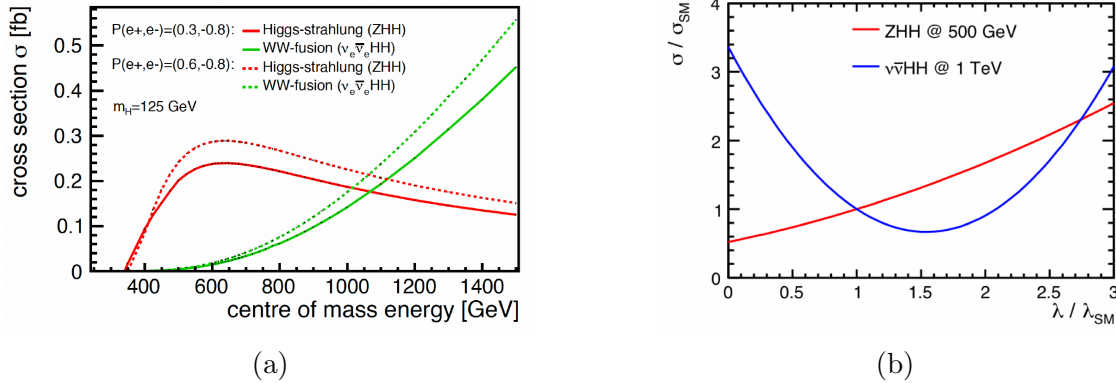


Figure 4: (a) Double-Higgs production cross sections of ZHH and WW fusion as a function of centre-of-mass energies for two different beam polarisation. (b) Precision of production cross sections for WW fusion and double higgstrahlung as a function of Higgs self-coupling λ normalised to λ_{SM} ²¹⁾

The most important benefit of an e^+e^- collider that can operate at a centre-of-mass energy of 500 GeV and above is that both the double Higgs production processes can be obtained. This is significant in the case where the value of λ is different from that predicted by the Standard Model. The precision of the production cross sections for WW fusion and double higgstrahlung as a function of Higgs self-coupling λ normalised to λ_{SM} is given in figure 4b. As can be seen, the cross-section for ZHH increases with an increase in triple Higgs coupling (λ) whereas the cross-section for the WW fusion process decreases. If the Higgs self-coupling deviates from the Standard Model, the two channels would interfere with the Standard Model effects. At the ILC, no matter which signs λ turns out to be, one of the possible reactions will increase in cross-section and reflect this improved sensitivity.

At proton colliders, this is however not the case. The dominant double Higgs production $gg \rightarrow HH$ is a fusion process with destructive interference. And the double Higgstrahlung process has a very small cross-section as compared to e^+e^- colliders. Therefore, unlike at the ILC, LHC can only have one process to measure the self-coupling. The ILC on the other hand can guarantee a measurement of the self-coupling at the level of at least 30% for whatever the value of self-coupling actually might be, combining the results from two different channels complimentary to each other. Figure 5 shows the impact of this synergy as compared to an extrapolation of the uncertainty projections from the ATLAS collaboration²²⁾ to non-Standard Model values of λ .

5 Top Quark Mass

The top quark mass is one of the important fundamental measurements to be experimentally determined. Direct measurements of top quark mass at hadron colliders could reach a precision of 600 MeV at the LHC^{26, 27)} and Tevatron²⁸⁾. Whereas, the top quark mass measurements at HL-LHC are expected to reach an experimental precision of a few hundred MeV²⁹⁾. An electron-positron collider that can produce top quark pairs has an excellent potential to measure the top quark mass with even better precision. Several studies of top threshold scan have

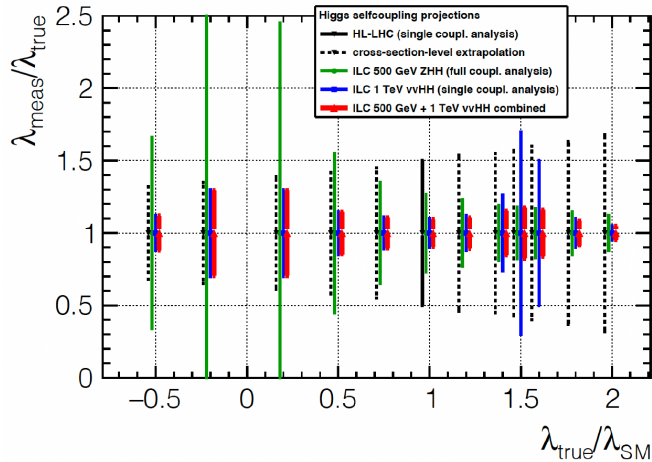


Figure 5: Expected uncertainties in the determination of the Higgs self-coupling at the HL-LHC and the ILC as a function of λ/λ_{SM} (19, 22).

been performed by several groups (30, 31, 32, 33). A simulated scan of top quark threshold in (30) is shown in Figure 6.

A statistical uncertainty of ~ 30 MeV was estimated in a study performed at CLIC with the l +jets channel with an integrated luminosity of 500 fb^{-1} at $\sqrt{s} = 380 \text{ GeV}$ (30).

6 Top Yukawa Coupling

The top quark is the particle that has the strongest coupling to the Higgs boson. Therefore it is very important to understand why the top-Yukawa coupling is the strongest among all the others. At the ILC, both direct and indirect probe of the top quark is possible. The main processes to access top quark at ILC are $e^+e^- \rightarrow t\bar{t}$ at $2m_t$, $e^+e^- \rightarrow t\bar{t}H$ and $e^+e^- \rightarrow t\bar{t}\nu_e\bar{\nu}_e$. The $t\bar{t}$ threshold scan offers an indirect measurement of top Yukawa coupling with a precision of 4% (23). To measure the top-Yukawa coupling directly, it is required that the centre-of-mass energy is at least 500 GeV. With a rise of the centre-of-mass energy further to 550 GeV the cross-section for $t\bar{t}H$ rises sharply by a factor of ~ 4 and the measurement of $t\bar{t}H$ coupling by a factor of two. Several studies have been performed on this for centre-of-mass energies ranging from 500 GeV - 1.4 TeV (23, 24, 25). For a centre-of-mass energy of 550 GeV and a nominal luminosity of 4 ab^{-1} , the top-Yukawa coupling can be measured with a precision of 2.8 %. With the increase in the centre-of-mass energy to 1 TeV and the luminosity to 8 ab^{-1} , the precision improves to 1 %.

7 Conclusion

This paper gives a very brief review of different kinds of studies at e^+e^- linear colliders, mainly for the studies conducted at the ILC. It can be seen that substantial improvements with respect to the hadron colliders are possible at the ILC for the discussed topics. Precise measurements of single Higgs and Higgs self-coupling are possible where especially the model-independent approach gives better possibilities. Along with precision measurements, a search for new particles in the electroweak scale may also be possible at the ILC.

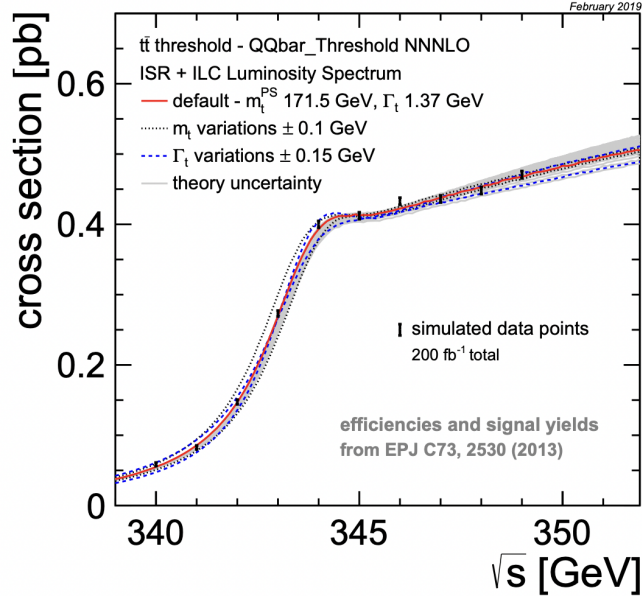


Figure 6: A simulated top quark threshold scan with an integrated luminosity of 200 fb^{-1} . The bands around the central cross section curve show the dependence of the cross section on the top quark mass and width ³⁰).

References

1. Abe, F. Observation of Top Quark Production in $\bar{p}p$ Collisions with the Collider Detector at Fermilab. *Phys. Rev. Lett.* **74**, 2626-2631 (1995,4), <https://link.aps.org/doi/10.1103/PhysRevLett.74.2626>.
2. Abachi, S. Observation of the Top Quark. *Phys. Rev. Lett.* **74**, 2632-2637 (1995,4), <https://link.aps.org/doi/10.1103/PhysRevLett.74.2632>.
3. Barber, D. Discovery of Three-Jet Events and a Test of Quantum Chromodynamics at PETRA. *Phys. Rev. Lett.* **43**, 830-833 (1979,9), <https://link.aps.org/doi/10.1103/PhysRevLett.43.830>.
4. Al, C. Evidence for gluon bremsstrahlung in ee annihilations at high energies. *Physics Letters B.* **86**, 418-425 (1979), <https://www.sciencedirect.com/science/article/pii/0370269379908694>.
5. The ALEPH Collaboration, The DELPHI Collaboration, The L3 Collaboration, The OPAL Collaboration, The SLD Collaboration, The LEP Electroweak Working Group, Electroweak, T. & Groups, H. Precision Electroweak Measurements on the Z Resonance. *Physics Reports.* **427**, 257-454 (2006,5), <http://arxiv.org/abs/hep-ex/0509008>, arXiv: hep-ex/0509008.
6. Aad, G. Combined Measurement of the Higgs Boson Mass in pp Collisions at $\sqrt{s} = 7$ and 8 TeV with the ATLAS and CMS Experiments. *Phys. Rev. Lett.* **114**, 191803 (2015,5), <https://journals.aps.org/prl/abstract/10.1103/PhysRevLett.114.191803>.
7. Adolphsen, C. The International Linear Collider Technical Design Report - Volume 3.II: Accelerator Baseline Design. *ArXiv:1306.6328 [physics]*. (2013,6), <http://arxiv.org/abs/1306.6328>, arXiv: 1306.6328.

8. Linssen, L., Miyamoto, A., Stanitzki, M. & Weerts, H. Physics and Detectors at CLIC: CLIC Conceptual Design Report. (arXiv,2012), <https://arxiv.org/abs/1202.5940>.
9. Fujii, K. The role of positron polarization for the initial 250 GeV stage of the International Linear Collider. *ArXiv:1801.02840 [hep-ex, Physics:hep-ph]*. (2018,1), <http://arxiv.org/abs/1801.02840>, arXiv: 1801.02840.
10. Moortgat-Pick, G. The role of polarized positrons and electrons in revealing fundamental interactions at the Linear Collider. *Physics Reports*. **460**, 131-243 (2008,5), <http://arxiv.org/abs/hep-ph/0507011>, arXiv: hep-ph/0507011.
11. Baer, H., Barklow, T., Fujii, K., Gao, Y., Hoang, A., Kanemura, S., List, J., Logan, H., Nomerotski, A., Perelstein, M., Peskin, M., Pöschl, R., Reuter, J., Riemann, S., Savoy-Navarro, A., Servant, G., Tait, T. & Yu, J. The International Linear Collider Technical Design Report - Volume 2: Physics. *ArXiv:1306.6352 [hep-ph]*. (2013,6), <http://arxiv.org/abs/1306.6352>, arXiv: 1306.6352.
12. Yan, J., Watanuki, S., Fujii, K., Ishikawa, A., Jeans, D., Strube, J., Tian, J. & Yamamoto, H. Measurement of the Higgs boson mass and $e^+e^- \rightarrow ZH$ cross section using $Z \rightarrow \mu^+\mu^-$ and $Z \rightarrow e^+e^-$ at the ILC. *Phys. Rev. D*. **94**, 113002 (2016).
13. Thomson, M. A. Model-independent measurement of the $e^+e^- \rightarrow HZ$ cross section at a future e^+e^- linear collider using hadronic Z decays. *Eur. Phys. J. C*. **76**, 72 (2016), <https://doi.org/10.1140/epjc/s10052-016-3911-5>.
14. Aryshev, A. The International Linear Collider: Report to Snowmass 2021. (arXiv,2022), <https://arxiv.org/abs/2203.07622>.
15. Ono, H. & Miyamoto, A. A study of the measurement precision of the Higgs boson branching ratios at the International Linear Collider. *Eur. Phys. J. C*. **73**, 2343 (2013).
16. The ILD Collaboration International Large Detector: Interim Design Report. (arXiv,2020), <https://arxiv.org/abs/2003.01116>.
17. Kawada, Shin-ichi, Fujii, Keisuke, Suehara, Taikan, Takahashi, Tooru & Tanabe, Tomohiko A study of the measurement precision of the Higgs boson decaying into tau pairs at the ILC. *Eur. Phys. J. C*. **75**, 617 (2015), <https://doi.org/10.1140/epjc/s10052-015-3854-2>.
18. Kawada, Shin-ichi, List, Jenny & Berggren, Mikael Prospects of measuring the branching fraction of the Higgs boson decaying into muon pairs at the International Linear Collider. *Eur. Phys. J. C*. **80**, 1186 (2020), <https://doi.org/10.1140/epjc/s10052-020-08729-7>.
19. Duerig, C. Measuring the Higgs self-coupling at the International Linear Collider.(2016).
20. Tian, J. Study of Higgs self-coupling at the ILC based on the full detector simulation at $\sqrt{s} = 500$ GeV and $\sqrt{s} = 1$ TeV. *3rd Linear Collider Forum*. pp. 224-247 (2013).
21. Higgs Projections using the ILD at the ILC, Junping Tian, ALCW15.
22. Measurement prospects of the pair production and self-coupling of the Higgs boson with the ATLAS experiment at the LH-LHC, ATLASCollaboration.

23. Yonamine, R., Ikematsu, K., Tanabe, T., Fujii, K., Kiyo, Y., Sumino, Y. & Yokoya, H. Measuring the top Yukawa coupling at the ILC at $\sqrt{s}=500$ GeV. *Phys. Rev. D.* **84** pp. 014033 (2011)
24. Abramowicz, H. & Others Higgs physics at the CLIC electron-positron linear collider. *Eur. Phys. J. C.* **77**, 475 (2017).
25. Price, T., Roloff, P., Strube, J. & Tanabe, T. Full simulation study of the top Yukawa coupling at the ILC at $\sqrt{s}=1$ TeV. *Eur. Phys. J. C.* **75**, 309 (2015).
26. Aaboud, M. et al. Measurement of the top quark mass in the $t\bar{t} \rightarrow \text{lepton}+\text{jets}$ channel from $\sqrt{s}=8$ TeV ATLAS data and combination with previous results. *Eur. Phys. J. C.* **79**, 290 (2019).
27. ATLAS, T., CDF, CMS & D0 Collaborations First combination of Tevatron and LHC measurements of the top-quark mass. *ArXiv E-prints*. pp. earXiv:1403.4427 (2014,3).
28. Tevatron Electroweak Working Group, T. & Aaltonen, T. Combination of CDF and D0 results on the mass of the top quark using up 9.7 fb^{-1} at the Tevatron. (2016,8).
29. Azzi, P. & Al. Standard Model Physics at the HL-LHC and HE-LHC. (2019,2).
30. Zarnecki, A. Top-quark physics at CLIC. *PoS. EPS-HEP2019* pp. 626 (2020).
31. Seidel, K., Simon, F., Tesar, M. & Poss, S. Top quark mass measurements at and above threshold at CLIC. *Eur. Phys. J. C.* **73**, 2530 (2013).
32. Horiguchi, T., Ishikawa, A., Suehara, T., Fujii, K., Sumino, Y., Kiyo, Y. & Yamamoto, H. Study of top quark pair production near threshold at the ILC. (2014).
33. Martinez, M. & Miquel, R. Multiparameter fits to the t anti-t threshold observables at a future e+ e- linear collider. *Eur. Phys. J. C.* **27** pp. 49-55 (2003).

Physics studies at FCC-ee

Gabriella Gaudio, on behalf of the FCC-ee group
INFN Pavia, via Bassi 6, 27100 Pavia, Italy

Abstract

An overview of the physics study program at the FCC-ee is given in the following. The key elements on which the physics program is based are reported, together with a summary of some of the most important measurements that can be addressed. In order to fulfil the studies described, physics benchmarks have been chosen, which have an impact on the design of the experiments. A description of those experiments are also reported in the following, with their distinctive characteristics.

1 Introduction

FCC-ee will be able to provide to the particle physics community a machine with an unprecedented potential for physics measurements and discovery. The richness of this physics program is based on a few key points, namely:

- Dedicated working points at specific centre-of-mass energies
- High statistics
- Precise center-of-mass energy determination
- Clean environment

A staged physics programs with 4 working points is foreseen, as detailed in tab. 1. They include a “Tera-Z” sample for very high precision measurements, a scan at the WW and the $t\bar{t}$ thresholds for either W boson or top quark mass and width measurements, runs at HZ peak for Higgs precision physics. As shown in tab. 1, the statistics which will be collected in each of the data taking periods is huge. This will

Table 1: *Working points foreseen at the FCC-ee.*

Working point	Z, years 1-2	Z later	WW	HZ	$t\bar{t}$	
\sqrt{s} (GeV)	88,91,94		157,163	240	340-350	365
Lumi/IP ($10^{34} cm^{-2} s^{-1}$)	115	230	28	8.5	0.95	1.55
Lumi/year (ab^{-1} , 2 IP)	24	48	6	1.7	0.2	0.34
Physics Goal (ab^{-1})	150		10	5	0.2	1.5
Run time (years)	2	2	2	3	1	4
Number of events	5×10^{12} Z		10^8 WW	10^6 HZ + 25k WW \rightarrow H	10^6 $t\bar{t}$ + 200k HZ + 50k WW \rightarrow H	

allow the statistical errors to be reduced, and, in turn to reduce also the systematic ones. In fact, the availability of a large sample will allow to select high purity samples of data for dedicated study on detector performances, thus improving the associated error. As it will be described in the next paragraph, the large data sample will allow also to perform an extremely precise global consistency check of the Standard Model (SM), through measurements of the electroweak precision observables. Beside that, reduction of the errors and large statistics, will allow for checking deviations from SM prediction, providing a tool to get hints from Beyond SM physics.

Another key element of the FCC-ee physics program is the precise center-of-mass energy determination. The transverse beam polarization provides, indeed, beam energy calibration through resonant depolarization. In fact, the spin tuning is related to the beam energy, as described in eq. 1:

$$\nu = \frac{g_e - 2}{2} \frac{E}{mc^2} = \frac{E_b}{0.44065686(1)} \quad (1)$$

As described in tab. 1, the luminosity that will be reached at FCC-ee will be much higher compared to the one of LEP. On the other hand, the number of bunches will be comparatively much higher, which in the end will contribute with a level of beam intensity per bunch similar to what obtained at LEP. Indeed, the occupancy foreseen in a typical vertex detector by the simulation is found to be of the order of 10^{-5} at the Z-pole and a few 10^{-4} at 365 GeV. These two elements contributes to the cleanness of the FCC-ee detector environment, which is another key elements of the future experiments which will contribute to the physics reach capability.

2 Physics Studies

An executive summary of the physics measurements which are foreseen at the Future Circular Collider is reported in Fig. 1 ²⁾. The two energy working points at the Z peak and the WW thresholds will allow for high statistics measurements. This will push the limits of the “intensity frontier” to unprecedented capability of improving the knowledge of the Electroweak Precision Observable (EWPO) at higher precision. The expected precision on the EWPO measurements is at the per mille level or even lower, for both statistical and systematic errors. The working point at the Higgs mass and the $t\bar{t}$ thresholds will improve our knowledge on the properties of this two particles. The W boson mass is expected to be known with a precision of few tenths of keV, while a few tens of MeV precision is expected for the top mass measurements. Once also the Higgs mass and couplings measurements will be improved beyond the current and foreseen reach of the HL-LHC, the SM prediction of several observables sensitive to electroweak radiative corrections become very well defined. Any deviation could indicate new physics.

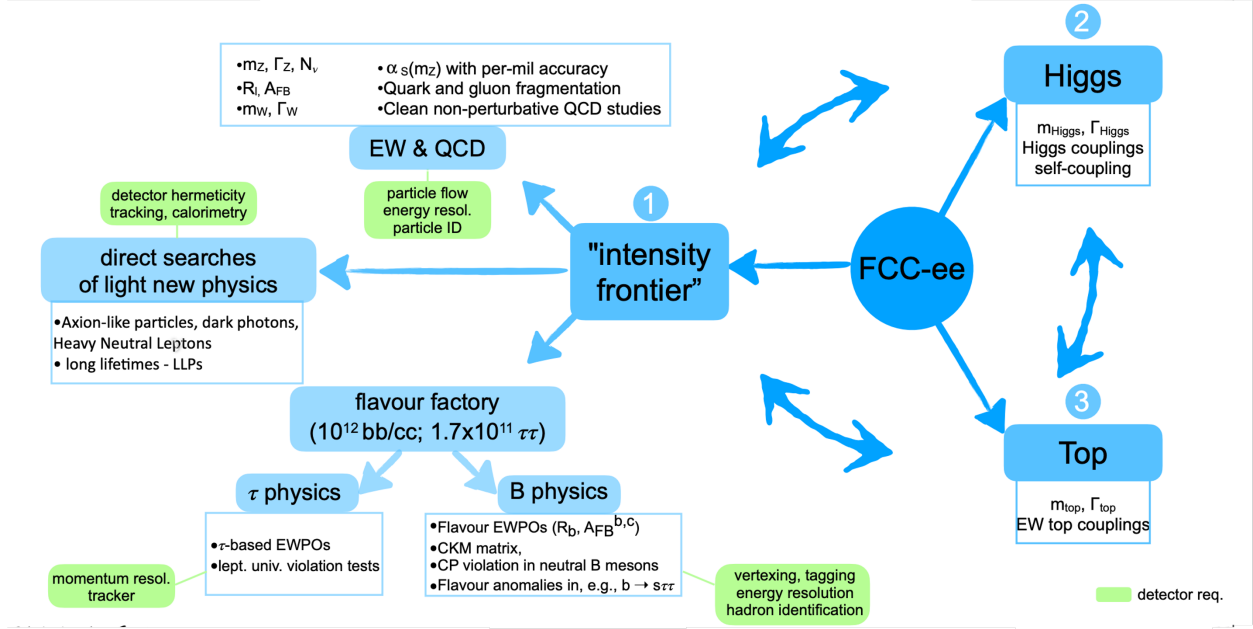


Figure 1: Overview of the physics potential at the FCC-ee.

The theoretical prediction of these quantities with a matching precision is an incredible challenge and work is going on to avoid this to be a limiting factor ³⁾. The expected confidence level obtained from the global fit in the (m_t, m_W) plane is shown in Fig. 2 left. As an example, the expected precision on the W-boson mass, at present is dominated by the uncertainty on the top mass of about 6 MeV, compared to theoretical uncertainty of 4 MeV. The FCC-ee will be able to measure the top mass at better than a MeV precision, leaving the theoretical uncertainty as the dominant one, if not reduced.

The FCC-ee measurements will also allow flavour physics to be constrained, both for the τ leptons and B hadrons. In particular FCC-ee will combine advantages of both the LHCb and the Belle2 experiments allowing for CP violation studies possible for very rare B-decays.

The preferred channel for Higgs production at the FCC-ee will be the Higgs-strahlung process. The measurement of the Higgs couplings in a model independent way can be obtained through the leptonic decay of the accompanying Z boson, as described in Fig. 2 right. An important parameter in this context is the recoil mass:

$$m_{recoil}^2 = (\sqrt{s} - E_{ll})^2 - p_{ll}^2 = s - 2E_{ll}\sqrt{s} + m_{ll}^2 \quad (2)$$

which is affected by the beam energy spread and the momentum resolution.

Besides the measurements described so far, also the searches Beyond the Standard Model (BSM) will be of great interest at the FCC-ee. In fact, both direct searches and indirect measurements will provide important hints in this field. Direct search can address evidence of particles such as Long Lived Particles with displaced vertices, rare or forbidden decays, axion-like particles and massive neutrinos. On the other hand, as mentioned before, high precision and high statistics will allow for new physics discovery as deviation from Standard Model expectation. Also particles with too high mass and/or with too feeble couplings can still contribute to loops or modify branching ratios. Moreover precise information on the parameters provides guidance to models to interpret deviations. It is worth mentioning that, in the BSM

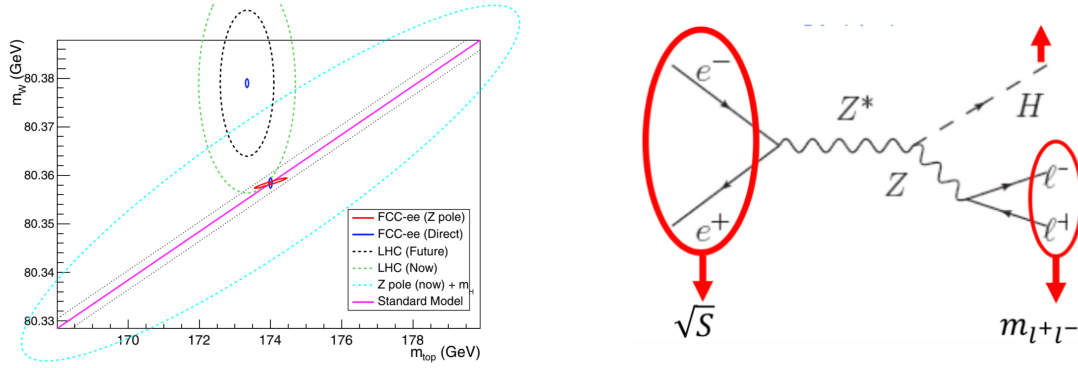


Figure 2: **Left:** Contours of 68% and 95% confidence level obtained from fits of the standard model to the precision measurements available to date, in the (m_t, m_W) plane and to the electroweak precision measurements offered by the FCC-ee, under the assumption that all relevant theory uncertainties can be reduced to match the experimental uncertainties. **Right:** Feynman diagram for the Higgs-strahlung process and the recoil mass calculation. See text for details.

more than in other researches, the integrated program of FCC-ee and FCC-hh will allow to cope with BSM search in a better and more efficient way.

There are also a number of additional or complementary studies which are not reported in the present paper. See ¹⁾ for further details.

3 Detector Concept and Performance Requirements

The physics studies that has been identified proceed in parallel to the proposal of detector concepts. Those proto-experiments foresee sub-detectors which are able to detect and measure the decay products of the particles of interest. Each proto-experiment is based on different and complementary characteristics.

The CLD layout (see Fig. 3 left) is inspired by the design for the Linear Collider detector, which is optimised for the Particle Flow reconstruction. For this reason, it features an all-silicon vertex detector which allows for high precision track and momentum measurements. The silicon tracker complements the Silicon-Tungsten Electromagnetic Calorimeter and the Scintillator-Steel Hadronic calorimeter, both

Table 2: *Required performance for the different sub-detectors, with associated benchmark physics process and measurements.*

Physics Process	Measured Quantity	Critical Detector	Required Performance
$ZH \rightarrow \ell^+ \ell^- X$	Higgs mass, cross section	Tracker	$\Delta(1/p_T) \sim 2 \times 10^{-5}$
$H \rightarrow \mu^+ \mu^-$	$\text{BR}(H \rightarrow \mu^+ \mu^-)$		$\oplus 1 \times 10^{-3} / (p_T \sin \theta)$
$H \rightarrow b\bar{b}, c\bar{c}, gg$	$\text{BR}(H \rightarrow b\bar{b}, c\bar{c}, gg)$	Vertex	$\sigma_{r\phi} \sim 5 \oplus 10 / (p \sin^{3/2} \theta) \mu\text{m}$
$H \rightarrow q\bar{q}, VV$	$\text{BR}(H \rightarrow q\bar{q}, VV)$	ECAL, HCAL	$\sigma_E^{\text{jet}} / E \sim 3 - 4\%$
$H \rightarrow \gamma\gamma$	$\text{BR}(H \rightarrow \gamma\gamma)$	ECAL	$\sigma_E \sim 16\% / \sqrt{E} \oplus 1\% \text{ (GeV)}$

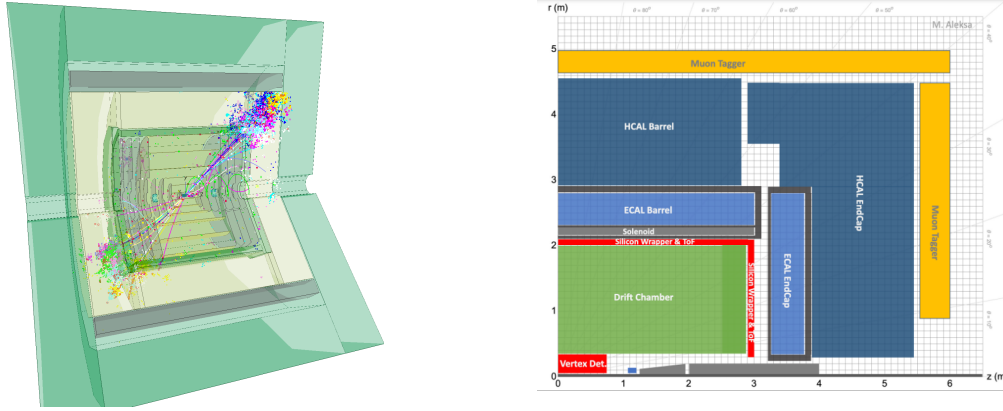


Figure 3: **Left:** Drawing of the CLD detector with a simulated 2-jet events. **Right:** Cut-out view of the newly proposed LAr based proto-experiment.

characterised by high granularity. Both calorimeters are immersed in a 2 T superconducting solenoid, required to open up as much as possible the energy deposits in the calorimeter and thus reducing the confusion term.

A complementary approach has been proposed by the IDEA proto-experiment, shown in Fig. 4 left, which is characterised by an ultra light drift chambers and a dual-readout ⁴⁾ calorimeter. Motivation for proposing an almost transparent inner detectors come from the fact that particles produced in the ZH events have a rather small p_T , therefore one needs to reduce as much as possible the effect of the multiple scattering for optimal resolution, as it is shown in Fig. 5 left.

The baseline option for the IDEA detector includes a longitudinally unsegmented fibre sampling

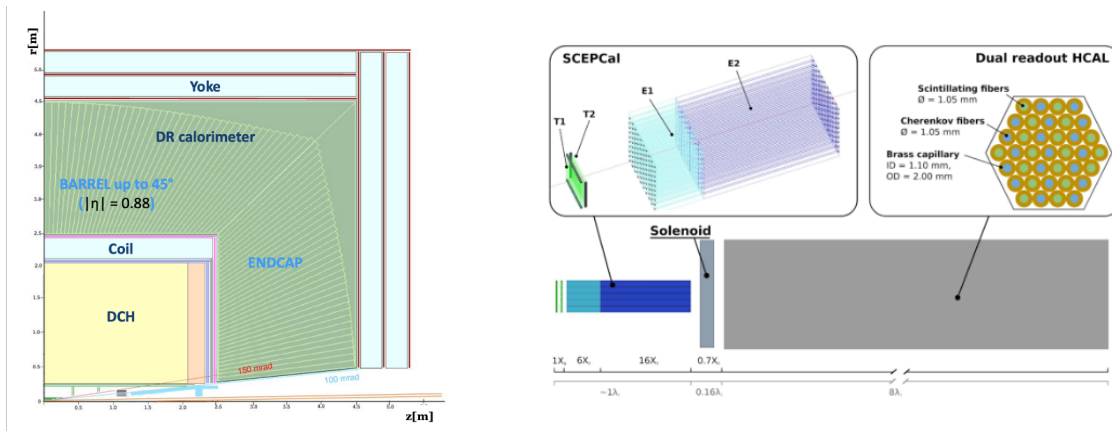


Figure 4: **Left:** Cut-out view of the IDEA proto-experiment **Right:** Representation of the crystal option layout for the IDEA dual readout calorimeter

calorimeter, based on dual-readout technique. It allows to sample the showers with both scintillating and Cherenkov fibres, to improve the hadronic energy resolution. This type of calorimeter works at the same time as an electromagnetic calorimeter. In this case, as a sample calorimeter it can guarantee an

energy resolution of about $15\%/\sqrt{E}$ with an optimal position and angular resolution. On the other end, for flavour physics studies an outstanding electromagnetic energy resolution is required. In this case a crystal option ⁵⁾, with dual readout capability, is also foreseen in the IDEA proposal. The layout of such an option is represented in Fig. 4 right.

While the two proto-experiments described above have been included in the CDR for FCC ¹⁾, more recently a third option has been proposed. It combines a drift chamber, as in the IDEA proposal, with a Liquid Noble gas Electromagnetic Calorimeter and an high granular Hadron Calorimeter based on tiles, as for the ATLAS experiment at the LHC. A layout of such a proposal is presented in Fig. 3 right.

A summary of the main physic processes to be measured, together with the detector which is mainly

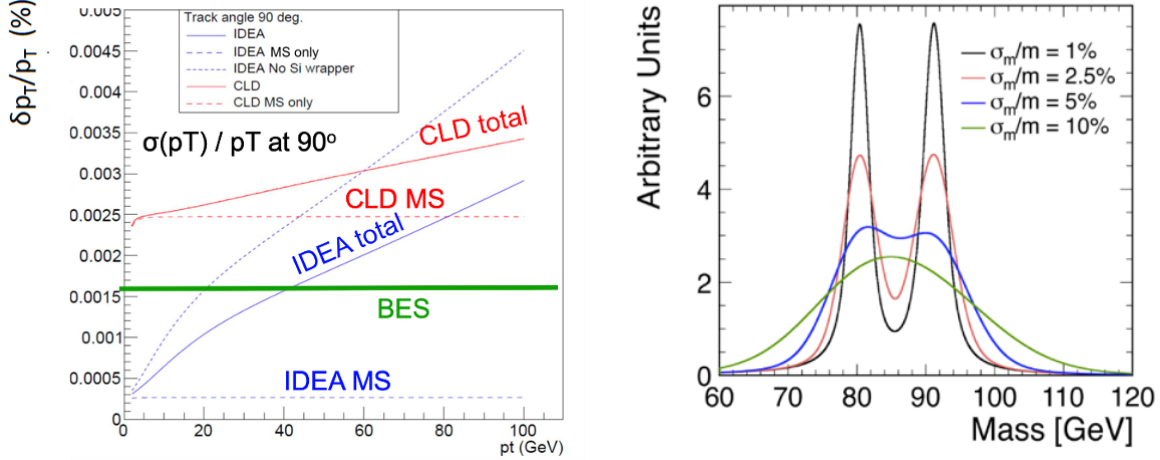


Figure 5: **Left:** Momentum resolution for tracks at 90 in the CLD and IDEA detectors. **Right:** Effect of the mass resolution on the capability for W and Z mass discrimination in an hadronic calorimeter.

involved in the measurement and the required performance is reported in table tab. 2. Beside the requirement already mentioned before on the momentum resolution, it worth noticing the request of 3-4% on the resolution of the jet energy, which is needed to correctly reconstruct and separate jet coming from Z, W and H bosons. The effect of such resolution is shown in Fig. 5 right.

References

1. “FCC-ee: The Lepton Collider”, Eur. Phys. J. Spec. Top. 228 (2019)
2. C. Grojean “FCC Physics Case: the once, the now, the future” FCC Week Paris, May 2022 https://indico.cern.ch/event/1064327/contributions/4893259/attachments/2452515/4432967/Grojean_FCCWeek_2022.05.30_eu.pdf
3. Heinemeyer, S., Jadach, S. Reuter, J. “Theory requirements for SM Higgs and EW precision physics at the FCC-ee”. Eur. Phys. J. Plus 136, 911 (2021).
4. S. Lee et al. Dual-readout calorimetry *American Physical Society (APS)* **2** 90 (2018)
5. M. Lucchini et al, New perspectives on segmented crystal calorimeters for future colliders *IOP Publishing* **15** (2020)

Dark matter from WIMP to FIMP over three regimes: Cosmology versus Colliders

Laura Lopez-Honorez^{1,2}, Quentin Decant¹, Sam Junius^{1,2,3} and Michel H.G. Tytgat¹

¹ *Service de Physique Théorique, Université Libre de Bruxelles, C.P. 225, 1050 Brussels, Belgium.*

² *Theoretische Natuurkunde & The International Solvay Institutes,*

³ *Inter-University Institute for High Energies, Vrije Universiteit Brussel, Pleinlaan 2, 1050 Brussels, Belgium.*

Abstract

Dark matter models can give rise to specific signatures at particle physics experiments or in cosmology. The details of the cosmological history can also influence the new physics signals to be expected at e.g. collider experiments. In these proceedings, we briefly summarize the case of dark matter weakly to feebly coupled to Standard Model fermions through t -channel portal dividing the discussion into three main regimes. We also underline the interplay between cosmology and particle physics.

1 Introduction

Cosmological observations imply that around 80% of the total matter content in our universe is made up of dark matter (DM).¹⁾ Despite substantial effort, searches in colliders, direct, and indirect experiments have so far not yielded any clear hints of interactions other than gravitational between the DM and the Standard Model (SM) particles. Weakly interacting massive particles (WIMP), produced through dark matter annihilation or co-annihilation driven freeze-out (FO) still agree with such absence of DM signal in, sometimes large, parts of their parameter space. On the other hand, feebly interacting dark matter particles (FIMP), more feebly coupled to the SM than WIMP, can easily evade WIMP searches. Here we first briefly review the possible mechanisms for DM production in the early universe, from WIMP to FIMP, going through DM (co-)annihilation, mediator annihilation and conversion driven FO, freeze-in (FI) and SuperWIMP (SW) mechanisms. We discuss then possible probes of dark matter including signatures in particle physics detectors and cosmology.

For concreteness, we focus here on top-philic and leptophilic dark matter, χ , in the form of a real scalar singlet or a Majorana fermion. We consider a DM coupling through a Yukawa type of interaction to a right-handed SM fermion f_R , being a top t_R or a light lepton ℓ_R , and a new charged dark sector

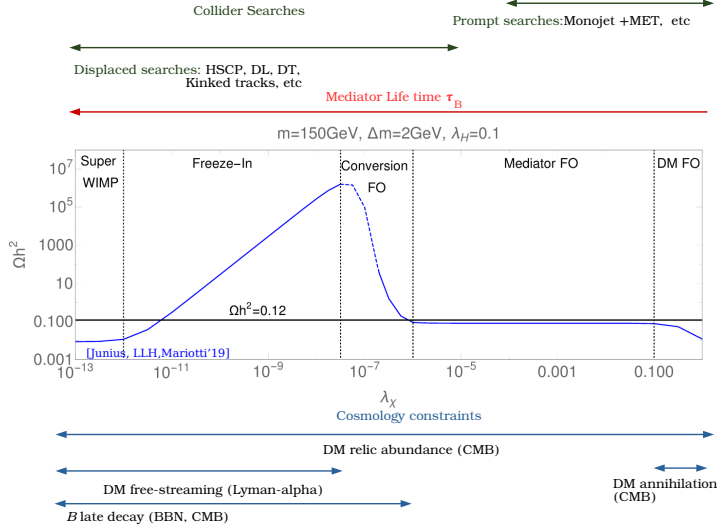


Figure 1: *DM abundance and production mechanisms as a function of the coupling for a compressed DM-mediator mass spectrum in a leptophilic scenario, see ²⁾ as well as ³⁾. As a guide for the eye, we show with arrows, above and below the plot, the range of couplings that may be probed at colliders and with cosmology data.*

bath particle, B . The lagrangian of the interaction reads:

$$\mathcal{L} \supset \lambda_\chi \Phi_B \bar{\chi} f_R + h.c. \quad \text{or} \quad \mathcal{L} \supset \lambda_\chi \chi \bar{\Psi}_B f_R + h.c. \quad (1)$$

where $B = \Phi_B (\Psi_B)$ denotes a charged scalar (fermion) bath particle. This particle is always in thermal contact with the SM in the early universe because of its gauge couplings and plays the role of the DM-SM mediator of interaction. We also assume that both dark sector particles B and χ are odd under a Z_2 symmetry while the SM particles are even. This ensures the DM stability. These type of DM scenarios are sometimes referred to as t -channel DM or vector-like portal to DM in the case of a WIMP and a scalar DM candidate, respectively. Let us emphasize that even though they correspond to rather minimal extensions of the SM, their DM phenomenology is very rich and has been investigated in multiple works.¹ Figure 1 illustrates the interplay between cosmology and colliders for a fermion leptophilic DM coupling to a muon as a function of the coupling λ_χ . The plot from ²⁾ shows the evolution of the DM relic abundance Ωh^2 as a function of λ_χ for a fixed value of the DM mass $m_\chi = 150$ GeV, and a small mass splitting of 2 GeV between the mediator B and the DM. A qualitatively similar result could be obtained for top-philic DM. By varying λ_χ between $\sim \mathcal{O}(1)$ and 10^{-14} , we go from WIMP production through DM annihilation FO to FIMP production through SW. Above and below the plot, the green and blue arrows indicate for which typical range of λ_χ colliders and cosmology probes may test the DM model. In what follows, we separate the discussion in three different regimes.

¹We apologize for the impossibility to cite all of the relevant works in these proceedings given the page number constraints. A more extended list of references on t -channel scenarios and the corresponding DM bounds from colliders, cosmology, etc can be found in the reference papers cited here.

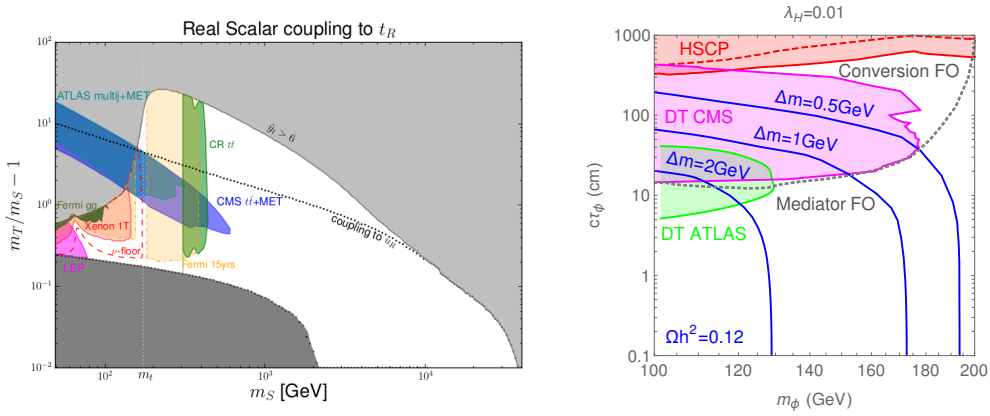


Figure 2: *Viable parameter space and constraints for top-philic scalar DM from DM (co-)annihilations driven freeze-out (Left) ⁴⁾ and leptophilic fermionic DM coupling to $f_R = \mu_R$ from mediator annihilations and conversion driven freeze-out (Right) ²⁾.*

2 WIMP from DM (co-)annihilation freeze-out

Vanilla WIMP DM is in chemical and kinetic equilibrium with the SM plasma in the early universe and decouples chemically, or freezes-out, when the rate of DM annihilations becomes too slow compared to the expansion rate of the universe. In the latter case one expects the DM relic abundance to be inversely proportional to the DM annihilation cross-section: $\Omega h^2 \sim \langle \sigma v \rangle_{\chi\chi}^{-1}$. This implies that Ωh^2 should decrease for increasing values of the coupling as visible in the right corner of Fig. 1. For the models considered here one would thus expect that $\Omega h^2 \sim \lambda_\chi^{-4}$ for annihilations through t -channel exchanges of the mediator B and a pair of fermions in the final state. Also, the presence of the mediator allows to account for the right DM abundance for small couplings $\lambda_\chi < 0.1$ and compressed spectra. In the latter cases, the DM relic abundance can become driven by co-annihilations (or mediator annihilations) with $\Omega h^2 \sim \langle \sigma v \rangle_{B\chi} \sim g^2 \lambda_\chi^2$ (or $\Omega h^2 \sim \langle \sigma v \rangle_{BB} \sim g^4$), where g denotes the gauge coupling of the mediator B . This is well visible in Fig. 1 around $\lambda_\chi \sim 0.1$ where the relic abundance becomes less and less sensitive to λ_χ for decreasing values of the latter. Naively, the main indirect dark matter signatures would be expected to come from DM annihilations into leptons or quarks. Let us emphasize though that, for Majorana or real scalar dark matter, the annihilation into a pair of light fermions is either p -wave or d -wave chirally suppressed and radiative processes, such as virtual internal Bremsstrahlung or loop induced annihilations into vector bosons, may leave the most promising signatures in indirect searches through gamma ray lines or even drive the dark matter relic abundance in the case of scalar DM, see e.g. ⁵⁾.

In the left panel of Fig. 2 we show the viable parameter space of a top-philic scalar DM obtained in ⁴⁾ in the relative mass splitting $m_B/m_\chi - 1$ versus dark matter mass plane. In the white region, the right abundance is obtained for couplings $\lambda_\chi \sim 10^{-2} - \mathcal{O}(1)$ through (co-)annihilation FO while, for the lowest values of the relative mass splitting, FO through mediator annihilations is giving the DM abundance for even more suppressed values of λ_χ . In the WIMP top-philic scenario, collider searches for prompt signatures (ATLAS and CMS in blue and LEP in pink) provide complementary constraints to direct dark matter searches in red and indirect dark matter searches in yellow and green. Still, a very large part of the viable parameter space remains unconstrained, even when updated constraints

from LHC are taken into account. Notice that a detailed treatment of radiative corrections to vector-like portal DM necessary for this analysis was provided in ⁶⁾. A review article on WIMP t -channel fermion DM can be found in ⁷⁾. Also notice that it is actually possible to get the right relic abundance of DM in the bottom dark gray zone through conversion driven FO introduced in ⁸⁾. This is addressed in the next section.

3 FIMP from DM mediator and conversion driven freeze-out

The fact that the relic abundance can be driven by co-annihilations and or, even more importantly, mediator annihilations is based on the assumption that the rate of $B \leftrightarrow \chi$ conversions is fast enough to keep DM in chemical equilibrium with the bath. For leptophilic DM, in Fig. 1, this assumption breaks when the relic abundance begins to increase again for decreasing values of λ_χ around 10^{-6} . Notice that such a small coupling implies the possibility to produce a long lived bath particle, coupled through gauge interactions, at colliders and potentially give rise to displaced signatures. In the case of mediator annihilation driven FO, arising for $\lambda_\chi \sim 10^{-6} - 10^{-2}$, the B annihilations and the relative mass splitting set the DM relic abundance. Ωh^2 shows no dependence in λ_χ . When $\lambda_\chi < 10^{-6}$, $B \leftrightarrow \chi$ conversions are no longer fast enough to convert DM back to bath particles efficiently and $n_\chi > n_\chi^{\text{eq}}$ before FO. The smaller the coupling, the slower are the conversions and the larger is n_χ at FO. This is the reason why Ωh^2 increases with decreasing λ_χ . This mechanism for setting the FIMP relic abundance has been dubbed conversion driven FO ⁸⁾.

Here we show the viable parameter space for a leptophilic fermion DM coupling to μ_R in the left panel of Fig. 2, see ²⁾, in the plane of the lifetime of the scalar bath particle $B = \Phi_B$, denoted as τ_ϕ , as a function of its mass, denoted as m_ϕ . Going to the upper part of the plot we are considering long lived Φ_B , with decay lengths of few centimeters or more. This corresponds to lower values of λ_χ and more compressed spectra. The relic abundance is driven by conversions (mediator annihilations) above (below) the gray dashed line. We directly see that the full viable parameter space for such production mechanism is already well constrained by displaced searches at colliders looking for heavy stable charged particles (HSCP) and disappearing tracks (DT), with the final leptons being too soft to be detected.

4 FIMP from freeze-in and superWIMPs

As can be seen in Fig. 1, another change in the relic abundance behaviour happens for even smaller couplings around $\lambda_\chi \sim \text{few} \times 10^{-8}$. At that point, the DM can not be expected to have ever been near kinetic or chemical equilibrium with the bath. The relic abundance then decreases with decreasing values of the coupling. This is the typical behaviour of DM production from FI through B decays. In the latter case, $\Omega h^2 \propto R_\Gamma$, where $R_\Gamma \sim M_p \Gamma_B / m_B^2$ is directly proportional to the bath particle decay rate with $\Gamma_B \propto \lambda_\chi^2$, i.e. $\Omega h^2 \propto \lambda_\chi^2$. The DM abundance is then set when the bath particle becomes non-relativistic and its number density becomes Boltzmann suppressed. In contrast, for $\lambda_\chi < 10^{-12}$, the DM abundance becomes again independent of λ_χ . This happens when the mediator lifetime is so long that it essentially decays after B chemical decoupling. In the latter case, for the models under study, the relic abundance is set by the so-called superWIMP mechanism and $\Omega_\chi = m_\chi / m_B \times \Omega_B$, i.e. the final DM relic abundance is independent of λ_χ . In practice, a combination of FI and SW production can also contribute to the DM abundance.

This is illustrated in the left panel of Fig. 3, where we show the viable parameter space for top-philic fermionic dark matter in the plane of $\Delta m = m_B - m_\chi$ as a function of λ_χ from ⁹⁾. The right FIMP relic

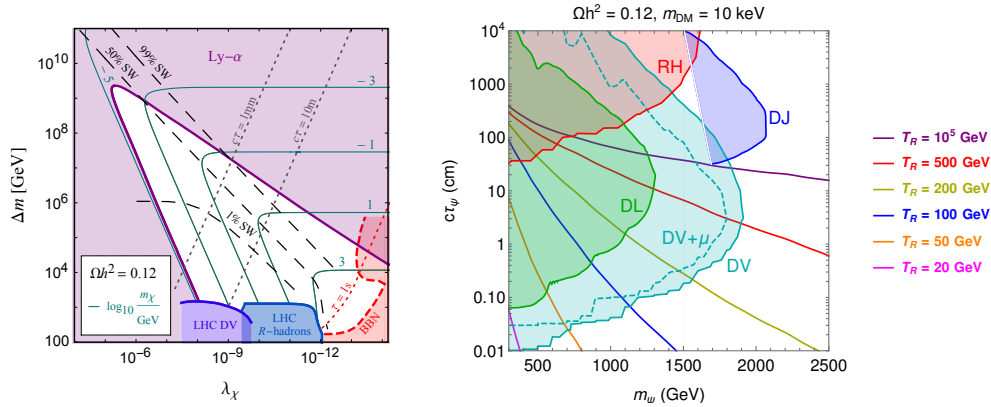


Figure 3: FIMP viable parameter space and constraints for top-philic DM in the case of fermion DM from FI and SW (left)⁹⁾ and of scalar DM from FI allowing for an early matter-dominated era (right)¹⁰⁾.

abundance is obtained along the cyan lines for different DM masses. The dashed black lines inform on the relative contribution of FI and SW to $\Omega_\chi h^2$. The colored areas are excluded by cosmological constraints (magenta for Lyman- α , and red for Big Bang Nucleosynthesis) and collider constraints (from displaced vertices, in purple, and R-hadrons searches, in blue). In⁹⁾ Lyman- α forest constraints on thermal warm DM were carefully re-interpreted to put generic constraints on free-streaming FIMPs excluding $m_\chi < 15$ keV for FI and masses as large as few GeV for SW. Very interestingly the left panel of Fig. 3 shows the nice interplay between collider and cosmology to corner the viable parameter space of FIMPs.

Now all the above results have been obtained assuming a standard cosmological history. In particular, it was assumed that the DM was produced in a radiation dominated era. When considering an early matter dominated era, with e.g. a low reheating temperature T_R , the relic abundance of dark matter can be diluted due to late time entropy injection. Interestingly for FI, this implies larger values of λ_χ or equivalently shorter B lifetimes/decay lengths. As a result, a larger part of the parameter space of FI scenarios can be tested at colliders through displaced searches. This is illustrated in the right panel of Fig. 3 from¹⁰⁾ in the case of a top-philic scalar DM scenario in the plane of the lifetime of the fermionic bath particle as a function of its mass, denoted with τ_Ψ and m_Ψ , respectively. The colored areas are excluded by displaced vertices +MET (DV) in light blue, delayed jet (dark blue) and R-hadron searches (red). The continuous colored lines serve as a rough estimate of the Lyman- α constraints for reheating temperatures between 20 GeV and 10^5 GeV. The surface below these lines would be excluded. As visible from the plot, with low $T_R = 20$ GeV displaced searches are much more efficient to exclude and probe in the future the small decay length parameter space. This illustrates yet another interesting interplay between cosmology and collider experiments. Also notice that in¹⁰⁾ a classification of DM scenarios for three-body interactions between DM, B and SM particles was proposed and a systematic analysis of prospects for detection at colliders through displaced signatures is provided.

5 Conclusions

Despite substantial experimental efforts dedicated to the search for DM, no indisputable signature of DM has been found in (astro-)particle physics experiments. In these proceedings we show that, even in a very simple t -channel portal DM set up, a plethora of production mechanisms are possible and a variety of DM

probes are necessary to pin point correctly the nature of dark matter. In the case of FIMPs in particular, we underline the very nice interplay that exists between cosmological probes, cosmological history and collider physics. It is also worth mentioning that in all cases, from WIMP to FIMP, a sometimes large part of the parameter space is still viable and potentially testable through specific signatures in colliders (with e.g. displaced signals), astro-particle physics experiments (with line like gamma-ray signals) and cosmology (with unconventional small-scale structure evolution). It is only combining all possible probes of DM that we can hope to conclusively test the DM nature.

6 Acknowledgements

We would like to thank all our collaborators for the work presented in these proceedings and LLH thank the organisers of the LFC22 meeting for the very nice workshop. LLH and QD have been supported by the Fonds de la Recherche Scientifique F.R.S.-FNRS through a research associate position and a FRIA PhD grant. LLH acknowledges support of the ARC program of the Federation Wallonie-Bruxelles. LLH, QD and SJ have been supported by the FNRS research grant number F.4520.19. SJ has also been supported by ULB and HEP VUB. The work of MT is supported by the F.R.S.-FNRS under the Excellence of Science (EoS) project No. 30820817 - be.h “The H boson gateway to physics beyond the Standard Model”. All co-authors acknowledge support of the IISN convention No. 4.4503.15.

References

1. N. Aghanim et al. Planck 2018 results. VI. Cosmological parameters. *Astron. Astrophys.*, 641:A6, 2020. [Erratum: *Astron.Astrophys.* 652, C4 (2021)].
2. Sam Junius, Laura Lopez-Honorez, and Alberto Mariotti. A feeble window on leptophilic dark matter. *JHEP*, 07:136, 2019.
3. Sam Junius, Searching for feebly interacting dark matter at colliders and beam-dump experiments, *ULB-VUB PhD thesis* [arXiv:2212.09432 [hep-ph]].
4. S. Colucci, B. Fuks, F. Giacchino, L. Lopez Honorez, M. H. G. Tytgat, and J. Vandecasteele. Top-philic Vector-Like Portal to Scalar Dark Matter. *Phys. Rev. D*, 98:035002, 2018.
5. Federica Giacchino, Laura Lopez-Honorez, and Michel H. G. Tytgat. Scalar Dark Matter Models with Significant Internal Bremsstrahlung. *JCAP*, 10:025, 2013.
6. S. Colucci, F. Giacchino, M. H. G. Tytgat and J. Vandecasteele, Radiative corrections to vectorlike portal dark matter, *Phys. Rev. D* **98** (2018) no.11, 115029
7. Mathias Garny, Alejandro Ibarra, and Stefan Vogl. Signatures of Majorana dark matter with t-channel mediators. *Int. J. Mod. Phys. D*, 24(07):1530019, 2015.
8. Mathias Garny, Jan Heisig, Benedikt Lülfi, and Stefan Vogl. Coannihilation without chemical equilibrium. *Phys. Rev. D*, 96(10):103521, 2017.
9. Quentin Decant, Jan Heisig, Deanna C. Hooper, and Laura Lopez-Honorez. Lyman- α constraints on freeze-in and superWIMPs. *JCAP*, 03:041, 2022.
10. Lorenzo Calibbi, Francesco D’Eramo, Sam Junius, Laura Lopez-Honorez, and Alberto Mariotti. Displaced new physics at colliders and the early universe before its first second. *JHEP*, 05:234, 2021.

Highlights of experimental results on heavy-ion physics from ALICE

Alberto Calivà

Physics Department “E.R. Caianiello”, University of Salerno, and National Institute of Nuclear Physics (INFN), Via Giovanni Paolo II, 132, 84084 Fisciano (Italy)

Abstract

The heavy-ion physics program of the ALICE Collaboration is very rich and covers the study many different observables that provide complementary information on the properties of the quark-gluon plasma. In this contribution, recent experimental highlights from the ALICE Collaboration on charmonium states, open heavy flavor, jet physics, light-flavor hadron production and electromagnetic probes, measured in different collision systems, are presented.

1 Heavy Quarkonia

Quarkonia are flavorless mesons made of heavy quark-antiquark pairs. Charm and bottom quarks are created in the early stages of the collision in hard parton-parton scattering processes. These particles then travel through the hot and dense QCD medium losing a fraction of their energy in collisions with other partons and (mostly) by gluon radiation. The energy loss effects can be quantified by the nuclear modification factor R_{AA} , defined as the ratio of the measured quarkonium yield in heavy-ion collisions and the $\langle N_{\text{coll}} \rangle$ -scaled yield measured in pp collisions at the same energy, where $\langle N_{\text{coll}} \rangle$ is the average number of binary nucleon-nucleon collisions. The R_{AA} of inclusive J/ψ measured at mid-rapidity is shown as a function of the average number of participant nucleons ($\langle N_{\text{part}} \rangle$) in Fig. 1 left. While the R_{AA} continuously decreases with increasing $\langle N_{\text{part}} \rangle$ at RHIC ^{1, 2}, an enhancement is observed at LHC energy starting from $\langle N_{\text{part}} \rangle \approx 100$. This effect is due to the recombination of charm-anticharm pairs in the late stages of the QGP evolution close to the phase boundary, as predicted by different theoretical works several years ago ^{3, 4, 5, 6}. Recombination effects, which become stronger going to more central collisions and lower transverse momentum (p_T), are observed also for the $\psi(2S)$ ⁷. Another interesting effect predicted many years ago and considered as a decisive signature of the QGP formation ⁸ is the sequential suppression of higher-mass quarkonium states. This is confirmed by the R_{AA} of the $\psi(2S)$

measured by ALICE at forward rapidity ⁷⁾, which is found to be smaller compared to that of the J/ψ (Fig. 1 right). The p_T dependence of the R_{AA} is well reproduced by the TAMU transport model ⁹⁾.

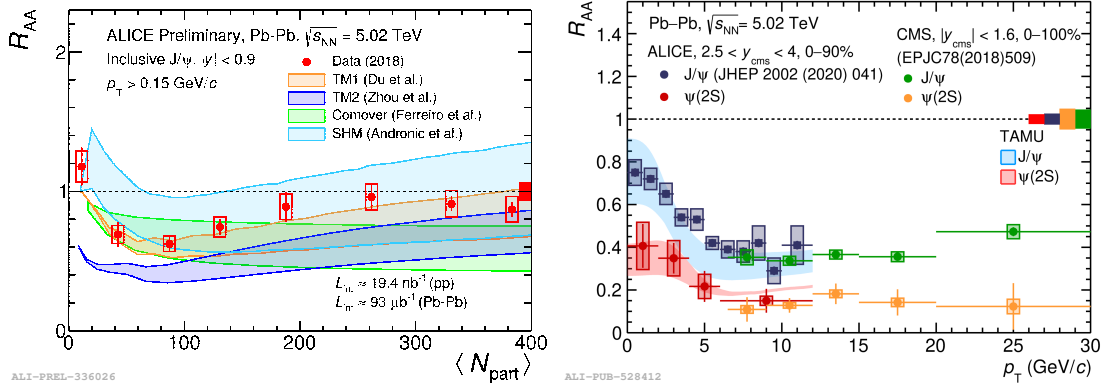


Figure 1: R_{AA} of inclusive J/ψ measured at mid-rapidity as a function of the average number of participant nucleons (left) and R_{AA} of both J/ψ and $\psi(2S)$ as a function of p_T (right).

2 Open Heavy Flavor

Open heavy-flavor hadrons are complementary probes to charmonia to study the in-medium energy loss of heavy quarks and characterize the QGP properties. Since the bottom quark is heavier than charm, it is expected to lose a lower fraction of its energy in collisions with other partons and by gluon radiation, due to the dead cone effect. This is confirmed by the measurement of the R_{AA} of prompt and non-prompt D^0 mesons in central Pb–Pb collisions at 5.02 TeV ¹⁰⁾, shown in Fig. 2 left. The ALICE measurement provides unprecedented access to the low p_T region, complementing existing results from ATLAS ¹¹⁾ and CMS ¹²⁾. The ratio of R_{AA} of non-prompt and prompt D^0 mesons, shown in Fig. 2 right, is sensitive to effects that are different for charm and bottom, such as shadowing, interaction with the medium, and mass-dependent radiative energy loss. Theoretical models that include both collisional and radiative energy loss describe the data within uncertainties. The R_{AA} and elliptic flow coefficient (v_2) of prompt D mesons are used by ALICE to constrain the spatial diffusion coefficients of charm ¹³⁾.

3 Jets

Jets are the result of the hadronization process of high-energy partons produced in the initial stages of the collision. Measurements of the jet suppression give information on how the initiating parton interacts with the produced medium. A hint for a higher suppression of inclusive jets as compared to jets containing a D^0 meson is observed from measurements of the charged-particle jets R_{AA} , shown in Fig. 3 left. This difference can be explained by the lower energy loss of heavy quarks inside the medium as compared to lighter quarks due to mass-dependent effects (dead cone). Medium-induced jet modifications are studied using the jet grooming technique, which allows one to find the first hard splitting inside the jet ¹⁴⁾. The jet cone in Pb–Pb collisions is found to be more collimated than in pp collisions, thus implying a suppression of wider jets due to interactions with the produced medium ¹⁴⁾. To further characterize the jet suppression phenomenon in heavy-ion collisions, the charged-jet R_{AA} is measured for different

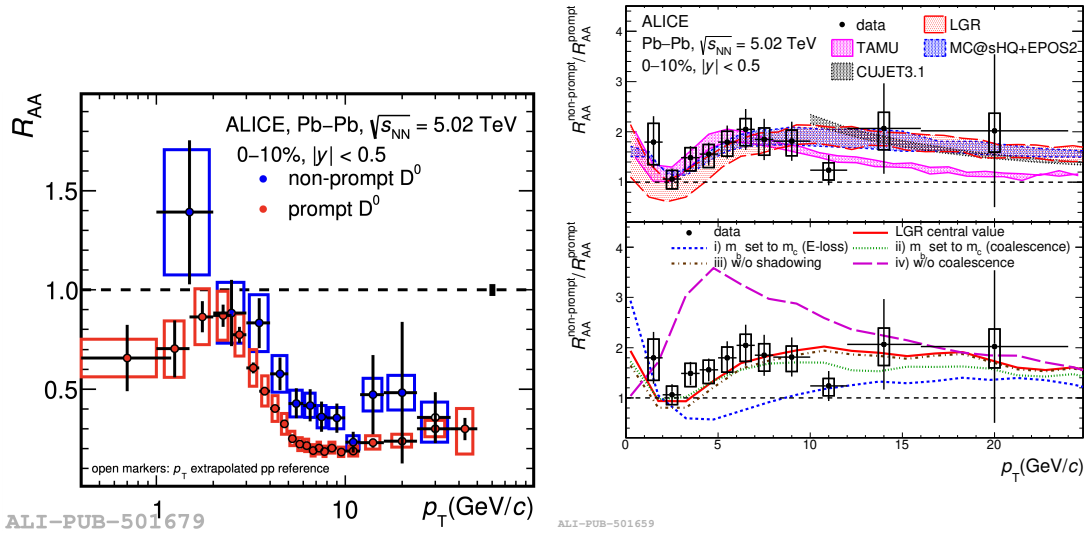


Figure 2: R_{AA} of prompt and non-prompt D^0 mesons in central Pb–Pb collisions at 5.02 TeV (left) and their ratio compared to theoretical models (right).

jet cone radii R . Wider jets are found to be more suppressed with respect to more collimated jets, as illustrated in Fig. 3 right.

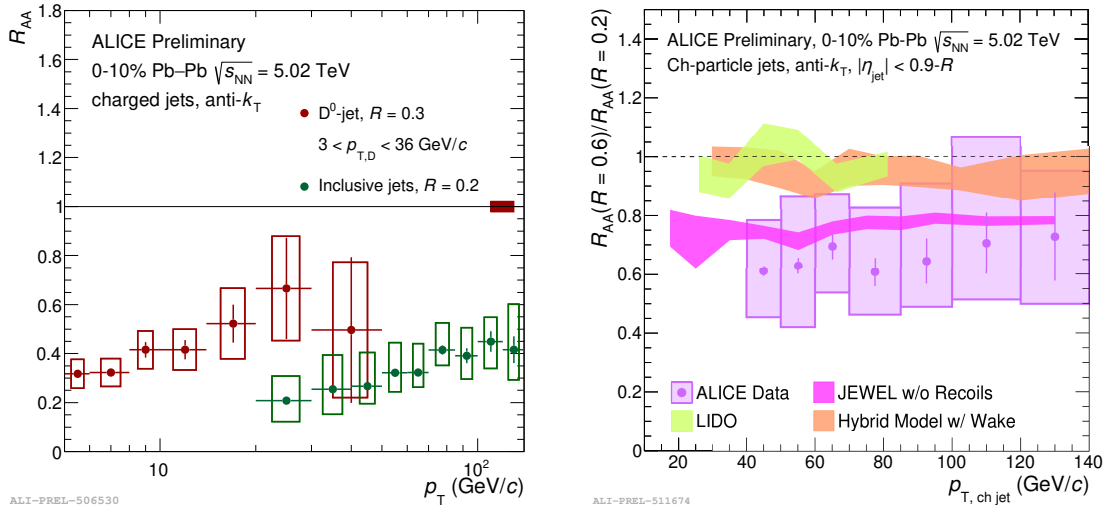


Figure 3: R_{AA} of inclusive and D^0 jets in Pb–Pb collisions at 5.02 TeV (left) and the ratio of charged-jet R_{AA} with different radii measured in Pb–Pb collisions (right).

4 Light Flavor

The bulk of particle production in heavy-ion collisions consists of light-flavor hadrons. Their yields are very well described by the statistical hadronization model (SHM) (15, 16, 17, 18), which assumes that particles are emitted by a source in local thermal and hadrochemical equilibrium with their abundances being fixed at chemical freeze-out, at a temperature of $T_{\text{chem}} = 156 \pm 4$ MeV. One of the parameters of this model is the baryochemical potential μ_B , which is a measure of the imbalance between matter and antimatter. This quantity is obtained with unprecedented precision by measuring antiparticle-to-particle ratios for different hadron species. A direct cancellation of correlated uncertainties between particles and antiparticles and an improved description of the hadronic interaction with the detector materials played a crucial role in the reached precision, which is almost one order of magnitude better than that obtained through the SHM fit, as shown in Fig. 4 left.

The properties of the hadron gas phase, produced after hadronization, can be studied by measuring the yields of short-lived resonances. Due to their short lifetimes, which are comparable to that of the hadron gas phase, resonance yields are affected by re-scattering effects of their decay daughters with other hadrons in the gas and also by re-generation effects, i.e. the back reaction to their decay. The ALICE Collaboration has measured the yield ratios of resonances with different lifetimes to those of the corresponding stable hadrons. Figure 4 right shows the $\Lambda(1520)/\Lambda$ measured as a function of multiplicity in different collision systems and center-of-mass energies. Although the $\Lambda(1520)$ has a longer lifetime than K^* , it shows a stronger suppression when going from peripheral to central Pb–Pb collisions than that of K^* (19). Obviously, the lifetime is not a good predictor for resonance suppression, which depends on the mean free path of the resonance in the hadron gas phase and on the (partial) chemical equilibrium with the system (20). The data challenge existing models which work for different resonances and fail for others.

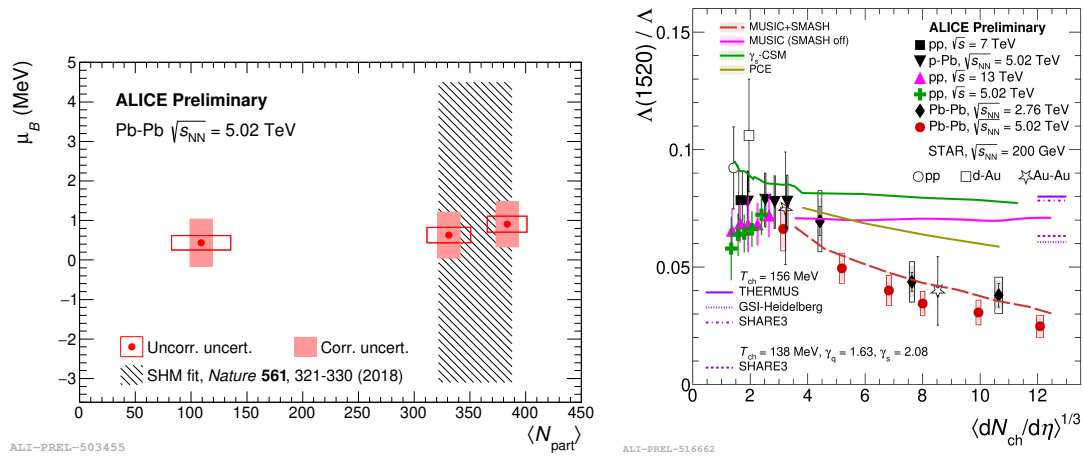


Figure 4: Baryochemical potential μ_B measured in Pb–Pb collisions at 5.02 TeV in comparison with the value obtained with the SHM fit (left) and $\Lambda(1520)/\Lambda$ as a function of multiplicity in different collision systems and center-of-mass energies (right).

5 Electromagnetic Probes

Direct photons and dileptons, i.e. lepton-antilepton pairs from virtual photons, are electromagnetic probes that are emitted continuously throughout the entire history of a heavy-ion collision. These particles interact with the medium only through the electroweak force, hence they carry undisturbed information on the production process. The low p_T region of the direct photon spectrum ($p_T \lesssim 3$ GeV/c) is sensitive to thermal radiation emitted by the QGP. The ratio R_γ between inclusive and decay photon spectra is measured in Pb–Pb collisions at 5.02 TeV as a function of p_T in different centrality intervals, as shown in Fig. 5 left. This ratio is close to unity at low p_T and rises to higher p_T , as expected by pQCD calculations that include prompt photon production from initial hard scattering²¹⁾. The sensitivity to thermal radiation is currently limited due to the large uncertainties of the measurement. Complementary information on direct photon production is obtained with dielectron (e^+e^-) measurements. The dielectron invariant-mass spectrum measured in Pb–Pb collisions at 5.02 TeV is shown in Fig. 5 right in comparison with the so-called “hadronic cocktail”, which is the sum of all contributions from hadron decays obtained from simulations. The data are consistent with theoretical model calculations that include thermal radiation from the QGP and contributions from in-medium ρ^0 decays, characterized by a broader spectral function. A detailed characterization of the ρ^0 spectral function and a precise measurement of the QGP temperature are expected in Run 3 thanks to the larger data sample that will be collected and the detector upgrade.

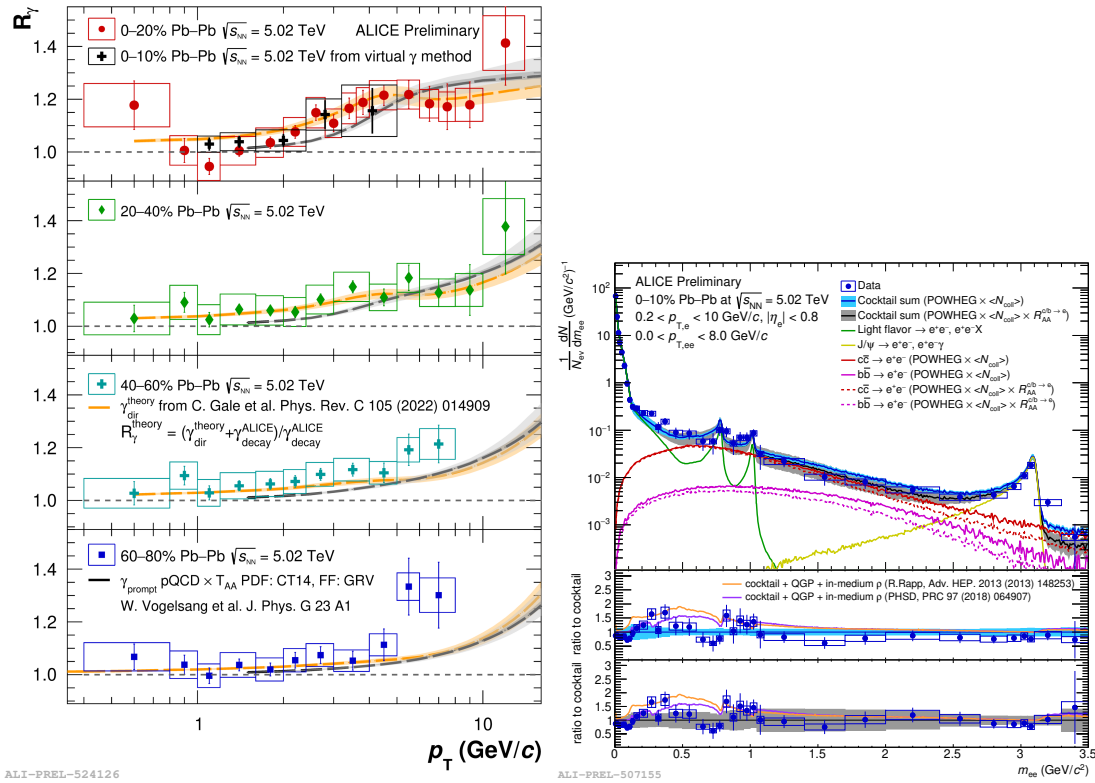


Figure 5: Ratio R_γ between inclusive and decay photon spectra measured in Pb–Pb collisions at 5.02 TeV as a function of p_T and dielectron invariant-mass spectrum (right) in comparison with theoretical model calculations.

6 Conclusions

Significant progress in the field of high-energy nuclear physics has been made by the ALICE Collaboration over the last few years. A detailed characterization of the QGP properties, spatial diffusion coefficients of heavy quarks in the QGP, as well as an in-depth understanding of a large variety of phenomena related to hadron production and hadronic interactions have been obtained. The study of rare events, improved precision of current measurements and more differential studies will be possible thanks to the detector upgrade and higher luminosity expected during Run 3.

References

1. L. Adamczyk *et al*, Phys. Lett. **B771**, 13-20 (2017).
2. J. Adam *et al*, Phys. Lett. **B797**, 134917 (2019).
3. B. Svetitsky, Phys. Rev. **D37**, 2484–2491 (1988).
4. P. Braun-Munzinger and J. Stachel, Phys. Lett. **B490**, 196–202 (2000).
5. R. L. Thews, M. Schroedter, and J. Rafelski, Phys. Rev. **C63**, 054905 (2001).
6. A. Andronic *et al*, Phys. Lett. **B797**, 134836 (2019).
7. ALICE Collaboration, arXiv:2210.08893v2 [nucl-ex] (2022).
8. S. Digal, P. Petreczky, and H. Satz, Phys. Rev. **D64**, 094015 (2001).
9. D. Xiaojian and R. Rapp, Nucl. Phys. **A943**, 147–158 (2015).
10. ALICE Collaboration, J. High Energ. Phys. **174** (2022).
11. ATLAS Collaboration, Eur. Phys. J. **C78**, 762 (2018).
12. CMS Collaboration, Eur. Phys. J. **C78**, 509 (2018).
13. ALICE Collaboration, JHEP **01**, 174 (2022).
14. ALICE Collaboration, Phys. Rev. Lett. **128**, 102001 (2022).
15. F. Becattini *et al*, Phys. Rev. **C90**, 054907 (2014).
16. V. Vovchenko and H. Stöcker, Phys. Rev. **C95**, 044904 (2017).
17. A. Andronic *et al*, Nature **561**, 321-330 (2018).
18. V. Vovchenko, B. Dönigus and H. Stöcker, Phys. Rev. **C100**, 054906 (2019).
19. ALICE Collaboration, Phys. Rev. **C91**, 024609 (2015).
20. A. Motornenko *et al*, Phys. Rev. **C102**, 024909 (2020).
21. C. Gale *et al*, Phys. Rev. **C105**, 014909 (2022).

COLOR SENSITIVE VARIABLES FOR $H \rightarrow b\bar{b}$ tagger

Giulia Manco

*Università degli studi di Pavia, Via Agostino Bassi***Abstract**

The Higgs decay in two b -quarks is very interesting and the most probable decay, but, due to the large QCD background, it is not straightforward to study. For this reason, the LHC community is investing in the direction of Xbb taggers ($X=Z$ boson or Higgs), which aims at finding an optimal Higgs-tagger using jet substructure information. Even if 10 years have passed from the discovery, the Higgs boson is still one of the most investigated particles at colliders and will be a warm topic also in the future. The Large Hadron Collider (LHC) produced around 8 million of Higgs boson and with the High Luminosity LHC (HL-LHC) the number will be improved by a factor 20, but will be not enough for having a complete knowledge of the boson. In the electroweak sector there are still several puzzling topics, i.e. the naturalness problem, the di-Higgs production, which need more sensitivity than available now: for them more powerful colliders are needed. Among the proposals, FCC-hh, the future hadron-hadron collider, scheduled for the second half of this century, would investigate the hadronic structure at center of mass energy of 100 TeV. In this document, color sensitive variables will be studied as Xbb tagger, exploiting the different color configuration of a colour-singlet and colour-octet. Observable performances are tested on the $VHbb$ channel in the boosted limit and their possible role in the future collider experiments is discussed.

1 Introduction

The Higgs boson was discovered in 2012 at LHC by the ATLAS and CMS Collaborations ¹⁾ ²⁾. Since then, the high energy physic community has been involved in the measurements of its proprieties. The Higgs boson gives the opportunity to test the Standard Model (SM) predictions and to discover new physics. In particular, the coupling of the Higgs particle is the only interaction that can test the difference between fermion generations.

At the Higgs boson mass of 125 GeV, the most probable decay is in two b quarks, with a branching ratio of

about 58%. The direct measurement of $b\bar{b}$ channel provides a test of the Yukawa coupling to a down-type quark and constrains the overall Higgs decay width. While this decay is the most frequent, it is a real experimental challenge to observe it. This is due to the overwhelming large QCD background that can mimic signal signature. The production mode usually analysed is the Higgs boson H in association with a vector boson V (W or Z), with the vector boson decaying leptonically and the Higgs boson decaying hadronically into a pair of b-quarks, which provides a clean experimental signature.

The hard b-quarks produced by the Higgs boson decay are usually detected as two separate b-jets. When the momentum of the jets is higher than their invariant mass, the regime is called *boosted*. In such situation, the two b-jets are close in angle and hence reconstructed as a single jet, also known as large radius jet.

In order to better discriminate the $H(b\bar{b})$ process over the production of the b-jets from a gluon collinear splitting $g(b\bar{b})$, many strategies have been developed. Several jet substructure techniques have been designed, which aim at improving discrimination performance by finding hard prongs inside the large radius jet. Specifically, the different radiation pattern of the signal and background can be exploited. In the signal case, the b-jets originate from a colour singlet and the radiation is more constrained inside the two b-quark system. In the background case, the radiation is more diffuse, due to the color connection with the initial state, as shown in Figure 1.

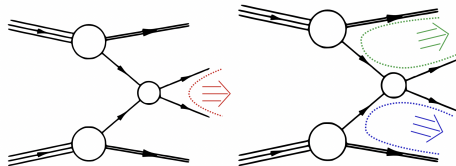


Figure 1: Possible color connections for signal on the left ($pp \rightarrow H \rightarrow b\bar{b}$) and for background on the right ($pp \rightarrow g \rightarrow b\bar{b}$) ⁵⁾.

Despite the excellent results obtained in the electroweak sector, there are still puzzling topics. LHC produced 8 million Higgs bosons so far, while HL-LHC will increase by a factor 20, with an estimated improving uncertainties of Higgs coupling by factor 5-10. By the way, the Higgs self-coupling and nature of electroweak symmetry break will remain unknown even after HL-LHC and FCC-ee. Higher energies are needed because many rare Higgs decay will be more probable. FCC-hh, future acellerator for hadron-hadron collisions, plans to reach center of mass energy of 100 TeV, almost 10 times compared to LHC. In Figure 2 the cross sections for the Higgs boson production in hadronic collisions are shown.

In this paper, observables sensitive to the different color configuration will be exploited, referring to this recent article ⁸⁾. The idea is build a tagger that can be applied for the decay products of a generic colour singlet X . In this regards, the Xbb tagger group in ATLAS aims at providing recommendations for the $H \rightarrow b\bar{b}$ tagging and tools for use within analysis. It is at intersection of jet substructure and b-tagging performance in boosted $H \rightarrow b\bar{b}$ topologies ⁹⁾. At the end some ideas for the application of the tagger in the future collider framework will be investigated.

2 Observables

A selection of high-level color sensitive variables are presented. They are introduced in the literature in the past few years. In particular ten variables are considered: jet pull variables ⁵⁾, t_{\parallel} , t_{\perp} , the pull

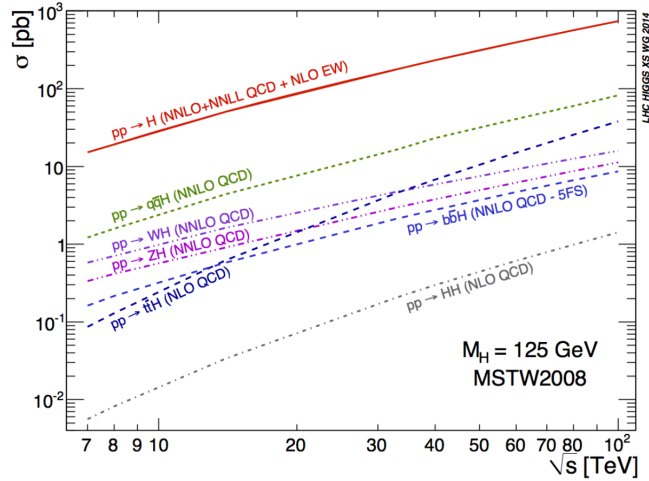


Figure 2: *Higgs production cross sections for hadron-hadron collisions* ⁶⁾.

Table 1: *Percentage of events which pass the analysis selections.*

	Truth	Reco
Signal	20%	17%
Background	1.6%	1.3%

angle θ_p ¹⁰⁾ for leading and subleading jets, jet colour ring \mathcal{O} ¹²⁾, D_2 ⁷⁾ and Lund jet plane ¹⁴⁾. They exploit the different color configurations in the b couple quarks decay, considering the direction of radiations emitted in the process.

3 Observable performances on $VHbb$ channel

3.1 Event simulation and selection

In order to test the observable discrimination performance, 300k events for $pp \rightarrow H(b\bar{b})Z(\nu_\ell\bar{\nu}_\ell)$ signal and 4M events for the $pp \rightarrow b\bar{b}\nu_\ell\bar{\nu}_\ell$ background processes are generated. Number of events are chosen in order to have 50k events for signal and background, according with efficiency after selection cuts, shown in Table 1. Hard events are generated with `MG5_aMC@NLO v2.8.3.2` ¹⁵⁾ in a boosted regime and parton-level events are then showered in `Pythia v8.305` ¹⁶⁾. Detector effects are considered with a fast detector simulation of `Delphes v3.5.0` ¹⁷⁾. From `Delphes` Monte Carlo truth is extracted, containing the particle-level information. The reference ⁸⁾ gives a complete description of analysis selections and simulation used here.

3.2 Discrimination performance

In Fig. 3 the normalised distributions for eight colour sensitive (CS) variables are shown, both for the signal and background, and at truth and reco level. Looking at the plots, the discrimination power of D_2 and \mathcal{O} can be appreciated and the detector effects, in particular on pull variables, can be observed.

In Fig. 2 the average Lund images for the signal and background process in the truth and reco case are

presented. From the plot, it is possible to appreciate the detector effect on image, which add in the reco case a radiation in the middle values of Δ and k_t .

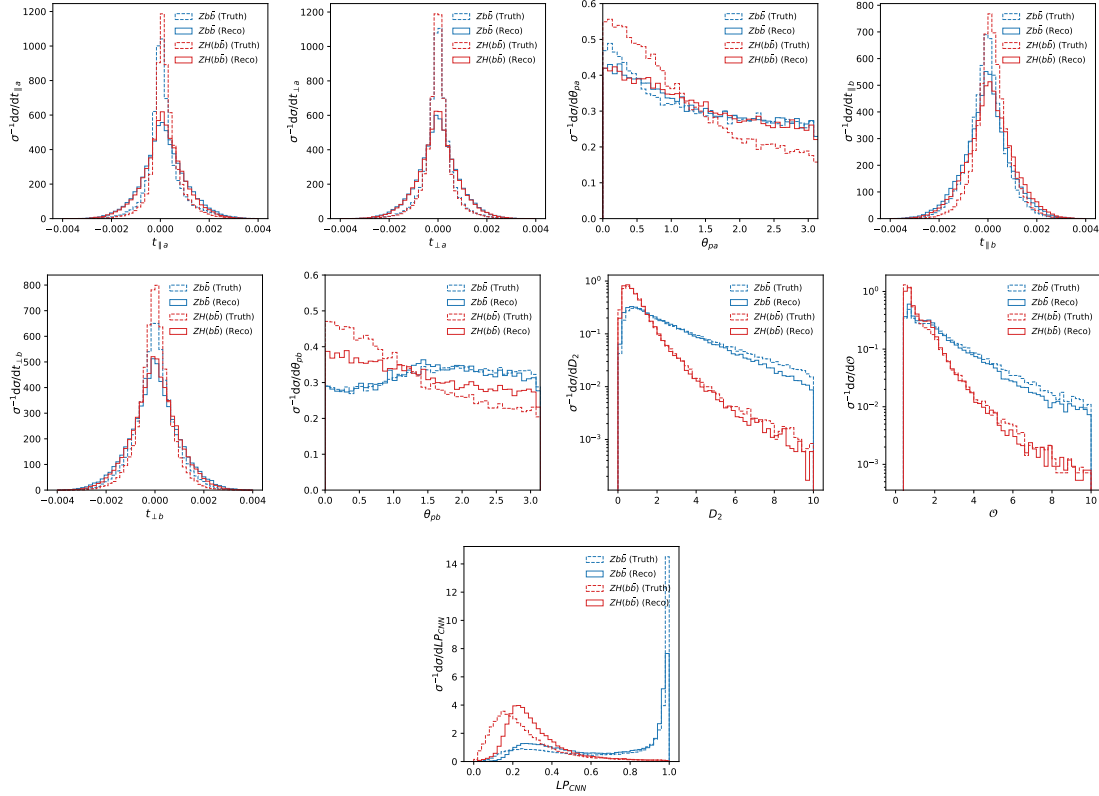


Figure 3: *Observables for signal and background, truth and reco cases, defined in Chapter 2 of 8).*

After having determined the distributions of the CS observables and the Lund jet images, these are used as inputs to ML algorithms in order to build combined classifiers. Specifically, a Boosted Decision Tree (BDT) is trained on the CS observables, whereas Lund images are classified using a Convolutional Neural Network (CNN). The output distribution of CNN Lund jet plane classifier is shown in Figure 3. More details about these methods and architectures are provided in 8).

Different combinations of variables are also considered in order to improve the total discrimination power. In this case the procedure is in two step, by using the CNN Lund jet plane classifier as an additional input to the BDT.

In Fig. 3, the receiver operating characteristic (ROC) curves for several combinations of observables are shown. It shows the background rejection ($1/\epsilon_b$) vs the signal efficiency (ϵ_s): higher is the curve, better is the discriminant power. Namely, are considered all the colour sensitive observables (CS) or just the D_2 and the colour ring (D_2 +CR), combined through a BDT; the CNN Lund jet plane classifier (LP_{CNN}); the combination of all the CS observables with the ($CS+LP_{CNN}$), by means of the two step procedure explained above. For each curve in Fig. 3, the value of the area under the ROC curve (AUC) is reported in Table 2.

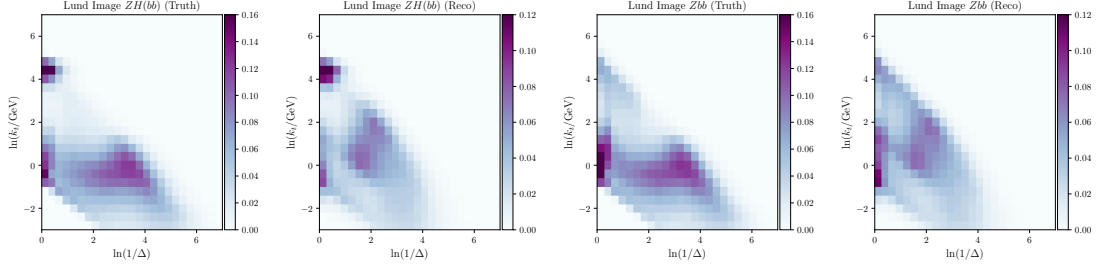


Figure 4: Averaged primary Lund jet plane images for $ZH(b\bar{b})$ and $Zb\bar{b}$ in the truth and reco case ⁸⁾.

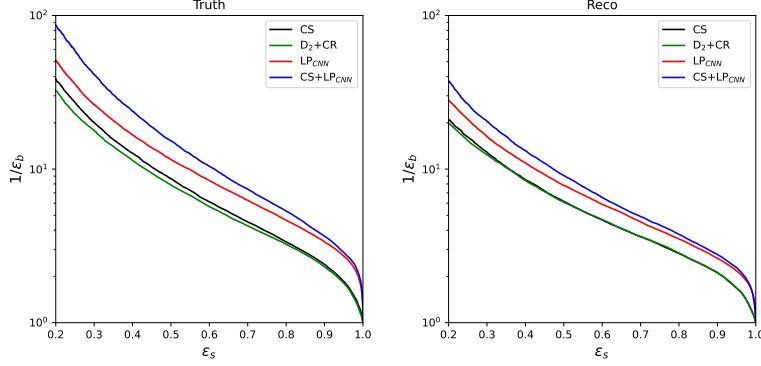


Figure 5: The ROC curves showing background rejection as a function of signal efficiency for the truth (left) and reco case (right) for CS variables, LP_{CNN} and the combined cases ⁸⁾.

3.3 Future perspectives

Xbb tagger techniques can be useful also in future collider analyses. Discrimination between a singlet and an octet of color can give its contribution in Higgs and Beyond Standard model (BSM) physics. Next colliders need to investigate electroweak sector, which is still puzzling: for example the Δm_H quantum correction of Higgs mass, naturalness problem ⁶⁾. Higgs self-coupling and nature of electroweak symmetry breaking will remain unknown even after HL-LHC and FCC-ee, which will provide only indirect results.

Di-Higgs production allows for investigations of the Standard Model λ parameters of the Higgs potential:

$$V(H) = \frac{1}{2}m_H^2 H^2 + \lambda_{3H\nu} H^3 + \frac{1}{4}\lambda_{4H} H^4 \quad (1)$$

As shown in Figure 6, FCC-hh will improve the sensitivity of k_3 (λ_3/λ_3^{SM}) from 50% of HL-LHC to 5% of FCC-hh. However, in the di-Higgs b couple channel the main source of background comes from the irreducible QCD production. The Xbb tagger can be useful in the di-Higgs production in bb channel, since can help to discriminate if they come from Higgs or QCD production.

Moving to BSM physics, the Xbb tagger can have an important role in the di-jet resonances in the final states. For example the tagger can help in case of Z'_B color singlet and G' color octet vector resonances identification respect QCD background or to discriminate to each other. In an extended $SU(3)_C$ color

Table 2: Area under the ROC curves for different combination of observables.

	Truth	Reco
CS observables	0.826	0.788
D_2+CR	0.817	0.787
LP_{CNN}	0.876	0.828
CS + LP_{CNN}	0.893	0.846

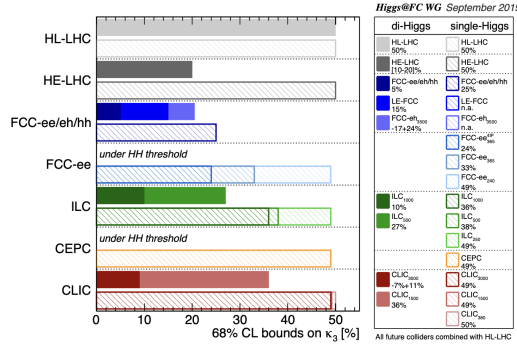


Figure 6: Sensitivity at 68% probability on the Higgs self-coupling parameter k_3 at the various future colliders ⁶⁾.

models G' arises as a heavy cousin of the SM gluon and couple universally to quarks with a coupling $g_s \tan \theta$, while Z'_B is predicted in models with gauged baryon number.

3.4 Results

As expected, the performances are worse in the reco case, due to detector resolution. However discrimination is still good for most combinations, close to 0.85 for CS + LP_{CNN} . It is evident that most of the discriminating power of CS is due to D_2+CR alone, both in AUC values and in distributions. It is clear that pull variables are not as powerful in discrimination as the other variables. Moving to the combination with the Lund jet plane, the Lund jet plane alone performs better than the whole set of CS observables. When LP_{CNN} is combined with CS observables, there is a noticeable improvement of the overall classification power, with a value of AUC equal to 0.893 in the truth case and 0.846 in the reco case.

4 Conclusions

In this paper, the problem of finding a Xbb tagger, namely to distinguish the b-jets originating from a colour singlet, as Higgs boson, from those originating from QCD background is investigated.

Colour sensitive observables present in literature are exploited in combination, in order to perform a powerful discriminator. These observables are tested on signal process $pp \rightarrow H(b\bar{b})Z(\nu_\ell\bar{\nu}_\ell)$, but the strategy can be valid in a more general context.

The discrimination performance is estimated using ML techniques, namely the BDT and CNN architectures. The BDT is trained with the colour sensitive variables, including the Lund jet plane CNN discriminator.

The results are encouraging, with a power in discrimination of 0.893 AUC for the combination of CS + LP_{CNN}.

In the end, this tagger, which is a combination of several theory-driven single-variable observables with a representation of radiation pattern within a jet, is not only effective in theory, but also shows promising prospects for application to future collider accelerators.

5 Acknowledgements

The author acknowledge the University of Pavia, in particular her supervisor Daniela Rebutzi, for the opportunity to attend the LFC22 workshop . We also thank the authors of the publication which inspired this paper ⁸⁾: Luca Cavallini, Andrea Coccaro, Charanjit Khosa, Simone Marzani, Fabrizio Parodi, Daniela Rebutzi, Alberto Rescia and Giovanni Stagnitto. In the end, the author acknowledges the LFC22 organisers for the opportunity to present this work.

References

1. ATLAS Collaboration, G.Aad et al., *Phys. Lett. B* **716** 1, 1-29 (2012).
2. CMS Collaboration, S.Chatrchyan et al., *Phys. Lett. B* **716** 30 1, 30-61 (2012).
3. ATLAS Collaboration, M. Aaboud et al., *Phys. Lett. B*, **786**, 59-86 (2018).
4. CMS Collaboration, Sirunyan, A. M. et al., *CMS-PAS-HIG-18-016*, (2018).
5. J. Gallicchio, M.D. Schwartz, *Phys. Rev. Lett* **105**, 022001 (2010).
6. Ellis, Richard Keith et al., *arXiv* (2019).
7. Larkoski, A.J., Salam, G.P. & Thaler, *J. High Energ. Phys.* **2013**, 108 (2013).
8. L. Cavallini, A. Coccaro, C.K. Khosa, G. Manco, S. Marzani, F. Parodi, D. Rebutzi, A. Rescia, G. Stagnitto, *Eur. Phys. J. C*, **82**, 493 (2022).
9. ATLAS Collaboration, *ATL-PHYS-PUB-2020-019*, (2020).
10. A.J.Larkoski, S. Marzani, C. Wu, *Phys. Rev. D* **99** 9, 091502 (2019).
11. Y.Bao and A.J. Larkoski, *JHEP* **12**, 035 (2019).
12. A.J. Larkoski, S. Marzani and C. Wu *SciPost Phys.* **9**, 026 (2020).
13. I. Moutl, L. Necib and J. Thaler, *JHEP* **12**, 153 (2016).
14. F.A. Dreyer, G.P. Salam and G. Soyez, *JHEP* **12**, 064 (2018).
15. J. Alwall, R. Frederix, S. Frixione, V. Hirschi, F. Maltoni, O. Mattelaer et al., *JHEP* **07**, 079 (2014).
16. T. Sjöstrand, S. Ask, J.R. Christiansen, R. Corke, N. Desai, P. Ilten et al., *Comput. Phys. Commun.* **191**, 159 (2015).
17. DELPHES 3 collaboration, *JHEP* **02**, 057 (2014).

INITIAL-STATE QED RADIATION AT NLL ACCURACY FOR FUTURE ELECTRON-POSITRON COLLIDERS

Giovanni Stagnitto

Physik-Institut, Universität Zürich, Winterthurerstrasse 190, CH-8057 Zürich, Switzerland

Abstract

We present state-of-the-art results for the QED Parton Distribution Functions (PDFs), which have been recently pushed up to next-to-leading logarithmic (NLL) accuracy. In particular, in this contribution, we will focus on a simple process as a toy model to explore the impact of NLL PDFs and the dependence on the renormalisation and factorisation scheme.

It is not unreasonable to assume that the future of high-energy physics will involve an e^+e^- collider. It is time for the theoretical community to start thinking about how to enlarge the legacy of LEP. The techniques and the calculations developed for LEP need to be revisited to keep up with the astonishing projected experimental error on measurements at future colliders. The relative error on several electroweak observables will reach 0.01% and possibly be even smaller.

The typical cross section relevant to e^+e^- collisions is in principle entirely computable as a perturbative series in the QED coupling constant α . However, calculations of processes in QED always feature large contributions stemming from photon collinear emissions in the initial state (initial state radiation, ISR). These contributions appear as logarithms to some power of some hard physical scale Q over the mass of the electron m_e , $L = \log^k(Q^2/m_e^2)$:

$$d\sigma_{e^+e^-} = \alpha^b \sum_{n=0}^{\infty} \alpha^n \left(c_0^{(n)} + c_1^{(n)} L + \dots + c_n^{(n)} L^n \right), \quad (1)$$

with b the power of α in the Born process. These logarithmic terms can be numerically large, preventing the perturbative series from being well behaved.

It is fortunate that such $\log^k(Q^2/m^2)$ terms are universal, hence they can be taken into account to all orders in α by a process-independent resummation procedure. With the *collinear factorisation* approach,

the physical cross section is written by means of a factorisation formula that recalls the standard QCD factorization formula at hadron colliders:

$$d\sigma_{e^+e^-} = \sum_{ij} \int dz_+ dz_- \Gamma_{i/e^+}(z_+, \mu^2, m_e^2) \Gamma_{j/e^-}(z_-, \mu^2, m_e^2) d\hat{\sigma}_{ij}(z_+, z_-, Q^2, \mu^2) + \mathcal{O}\left(\frac{m_e^2}{Q^2}\right). \quad (2)$$

Let us describe the various terms present in this equation: $d\sigma_{e^+e^-}$ is the *particle-level* cross section, computed with massive electrons; $d\hat{\sigma}_{ij}$ is a *parton-level* cross section, understood to be computed with massless electrons, which does not contain any logarithmic term, and is expected to be well-behaved order by order in perturbation theory; z_{\pm} are the longitudinal momentum fractions carried by the partons w.r.t. their mother particle; $\Gamma_{i/e^{\pm}}$ are the Parton Distribution Functions (PDFs) of the electron or the positron, a name that originates from the analogy of Eq. 2 with its QCD counterpart. PDFs are universal and resum to all order the collinear logarithms due ISR. Note that the nature of the parton entering the short-distance cross section can coincide with that of the incoming particle e.g. $(i, j) = (e^+, e^-)$, or it can differ e.g. $(i, j) = (\gamma, e^-), (e^-, e^-), \dots$. Moreover, as in QCD, a suitable factorisation scheme must be introduced (e.g. $\overline{\text{MS}}$) to regulate the zero-mass divergences in the parton-level cross section and a factorization scale μ^2 appears both in the $\Gamma_{i/e^{\pm}}$ and in $d\hat{\sigma}_{ij}$.

At variance with hadronic PDFs, QED PDFs are entirely calculable with perturbative techniques. In the following, we will mostly focus on the PDFs relevant to an incoming unpolarised electron particle, $\Gamma_{i/e^-} \equiv \Gamma_i$; the PDFs of an incoming positron are trivially related by charge conjugation. We will refer to Γ_{e^-} as electron PDF, and to Γ_{γ} as photon PDF. At the initial scale $\mu_0^2 \simeq m_e^2$, the leading order initial condition is a trivial $\Gamma_{e^-}(z, \mu_0^2) = \delta(1 - z)$. The PDF at the final scale μ^2 can be obtained by means of QED DGLAP evolution equations ^{1, 2, 3, 4}. At leading logarithmic (LL) accuracy i.e. the resummation of the dominant tower of $(\alpha L)^k$ terms, analytical expressions have been known for a long time ^{2, 3, 5, 6}:

$$\Gamma_{e^-}^{\text{LL}}(z, \mu^2) = \frac{\exp[(3/4 - \gamma_E)\eta]}{\Gamma(1 + \eta)} \eta (1 - z)^{-1 + \eta} - \frac{1}{2} \eta (1 + z) + \mathcal{O}(\alpha^2), \quad \eta = \frac{\alpha}{\pi} L. \quad (3)$$

Such LL analytical expressions are built out of an additive matching between a recursive solution up to some order in α , typically $\mathcal{O}(\alpha^3)$, and an all-order α solution valid in the region $z \rightarrow 1$. Note that with Q of the order of a few hundred GeV's one obtains $\eta \sim 0.05$. Therefore, because of the $(1 - z)^{-1 + \eta}$ factor, the PDF is very peaked towards $z = 1$, where it diverges with an integrable singularity. In general, such a peculiar structure of the PDFs requires a suitable re-parameterization of the phase-space ⁷) when numerically performing the convolution in Eq. 2.

In view of high-energy future colliders and the need for precise predictions, LL accuracy for QED PDFs is certainly insufficient. Moreover, theoretical systematics are not well defined in a LL-accurate picture. For instance, the value of α in Eq. 3 is entirely arbitrary at LL: whether α runs or not, or more generally in which renormalisation scheme α is defined, are questions that arise only at higher orders. To improve on the LL result, one can calculate individual higher powers of $\alpha^l L^k$ by means of fixed-order calculations (see e.g. ⁸) and references therein) or extend the resummed result to next-to-leading logarithmic (NLL) accuracy i.e. resumming also the tower of $\alpha(\alpha L)^k$ terms. We will focus on the latter.

In Ref. ⁹), the electron, positron, and photon PDFs of the unpolarised electron have been calculated at NLL accuracy in the $\overline{\text{MS}}$ factorisation and renormalisation scheme. The PDFs have been derived by solving the DGLAP equations both numerically and analytically, by using as initial conditions for the evolution the ones derived in Ref. ¹⁰). In Ref. ¹¹), these results have been improved in several directions: first, with a DGLAP evolution featuring multiple fermion families (leptons and quarks) in

a variable flavour number scheme i.e. by properly including the respective mass thresholds; second, by taking into account an alternative factorisation scheme, the Δ scheme ¹²⁾, where the NLO initial condition are maximally simplified; third, by considering two alternative renormalisation schemes, $\alpha(m_Z)$ and G_μ schemes (where α is fixed).

NLL PDFs ready for phenomenology can be obtained with the public code EMELA, available here:

<https://github.com/gstagnit/eMELA>

Such a code supersedes the one developed in Ref. ⁹⁾ (EPDF), that was limited to the evolution with a single lepton in the $\overline{\text{MS}}$ renormalisation and factorisation schemes. EMELA is a standalone code, and can be linked to any external program. Since a runtime evaluation of the numerical solution is likely too slow for phenomenological applications, the possibility is given to the user to output the PDFs as grids compliant with the LHAPDF ¹³⁾ format, that can be employed at a later stage. Moreover, regardless of whether the numerical solution is computed at runtime or read from the grids, EMELA always switches to the analytical solution for $z \rightarrow 1$. EMELA can also provide one with PDFs with beamstrahlung effects, according to the procedure presented in Ref. ⁷⁾.

In Ref. ¹¹⁾, EMELA has been linked to MADGRAPH5_AMC@NLO ^{14, 15)} in order to reach NLL accuracy for the PDFs and NLO accuracy (in the full electroweak theory) for the short-distance cross section, and obtain first NLL+NLO predictions for physical observables at lepton colliders. While MADGRAPH5_AMC@NLO is widely used in the context of LHC simulations, it can also be employed for lepton collisions. Indeed, many results for leptonic collisions were already provided in Ref. ¹⁴⁾, including NLO-QCD corrections but limited to the case of a strictly fixed centre-of-mass energy. The extension to the case with QED ISR and beamstrahlung has been documented in Ref. ⁷⁾, whereas Ref. ¹¹⁾ describes the inclusion of NLO EW corrections to the short distance cross section, allowing for the computation of NLL+NLO observables after linking to EMELA.

In order to investigate the effect of NLL PDFs, here we focus on a toy model process,

$$e^+e^- \rightarrow q\bar{q}(\gamma), \quad (4)$$

with a final state photon only present in the real-emission NLO contribution. In Eq. 4, q is a massless fermion of charge e_q , and in the corresponding short-distance cross sections we retain only the contributions proportional to e_q^2 (this limits the real and virtual radiation to the initial state, and thus the process is effectively equivalent to that for the production of a heavy neutral object of variable mass). Note that this is the process already used in Ref. ¹⁰⁾ for the determination of the initial conditions for the electron PDFs. The process under consideration is simple enough to be easy to calculate (indeed its simple analytical cross sections have been used as a cross-check of the corresponding automated computation carried out by MG5_AMC), but interesting enough to be able to draw some physical considerations.

We calculate the particle-level (parton-level) cross section as differential in τ ($\hat{\tau}$), defined as:

$$\tau = \frac{M_{q\bar{q}}^2}{s}, \quad \hat{\tau} = \frac{M_{q\bar{q}}^2}{\hat{s}} = \frac{\tau}{z_+z_-}, \quad (5)$$

with $M_{q\bar{q}}^2$ the invariant mass squared of the pair of final state quarks. Eq. 2 can be rewritten as

$$\frac{d\sigma}{d\tau} = \int_0^1 dz_+ dz_- d\hat{\tau} \Gamma_{e^-}(z_+, \mu_F^2) \Gamma_{e^-}(z_-, \mu_F^2) \frac{d\hat{\sigma}}{d\hat{\tau}}(\hat{\tau}, \mu_F^2) \delta(z_+z_- \hat{\tau} - \tau), \quad (6)$$

with the parton-level cross section given by the sum of the LO and the NLO contributions,

$$\frac{d\hat{\sigma}}{d\hat{\tau}} = \frac{d\hat{\sigma}^{[0]}}{d\hat{\tau}} + \frac{\alpha}{2\pi} \frac{d\hat{\sigma}^{[1]}}{d\hat{\tau}}. \quad (7)$$

The LO contribution is trivially given by

$$\frac{d\hat{\sigma}^{[0]}}{d\hat{\tau}} = B(\hat{s}) \delta(1 - \hat{\tau}), \quad B(\hat{s}) = \frac{4\pi\alpha^2}{3\hat{s}}. \quad (8)$$

In full generality, the NLO contribution is given by

$$\begin{aligned} \frac{d\hat{\sigma}^{[1]}}{d\hat{\tau}} = B(\hat{s}) \frac{1}{\hat{\tau}} & \left[2 \left(\frac{1 + \hat{\tau}^2}{(1 - \hat{\tau})_+} + \frac{3}{2} \delta(1 - \hat{\tau}) \right) \log \frac{\hat{s}}{\mu_F^2} - 2K_F(\hat{\tau}) + 2(2\pi)K_R\delta(1 - \hat{\tau}) \right. \\ & \left. + 4(1 + \hat{\tau}^2) \left(\frac{\log(1 - \hat{\tau})}{1 - \hat{\tau}} \right)_+ + \delta(1 - \hat{\tau}) \left(-\frac{92}{9} + \frac{2}{3}\pi^2 + \frac{4}{3} \log \frac{\hat{s}}{\mu_R^2} \right) \right]. \quad (9) \end{aligned}$$

The term proportional to K_F is related to the change of factorisation scheme, with the factor of 2 due to the fact that there are two incoming legs. In the $\overline{\text{MS}}$ factorisation scheme, $K_F^{\overline{\text{MS}}}(z) = 0$, whereas in the e.g. Δ scheme we have

$$K_F^{\Delta}(z) = \left[\frac{1 + z^2}{1 - z} (2 \log(1 - z) + 1) \right]_+. \quad (10)$$

The term proportional to K_R is related to the change of factorisation scheme, with the factor of 2 due to the power of α in Eq. 8. In the $\overline{\text{MS}}$ renormalisation scheme, $K_R^{\overline{\text{MS}}}(z) = 0$, whereas in the e.g. $\alpha(m_Z)$ scheme with a single active lepton, by neglecting the presence of thresholds and the W-boson contribution to the running of α , we have

$$K_R^{\alpha(m_Z)} = \frac{1}{3\pi} \log \frac{\mu_R^2}{m_Z^2} + \frac{5}{9\pi}. \quad (11)$$

More involved expressions in presence of multiple fermion families (leptons and quarks) by properly including the respective mass thresholds can be easily obtained with the results presented in Sec. 4 of Ref. 11).

In the following, we will focus on the cumulative cross section defined as

$$\sigma(\tau_{\min}) = \int d\sigma \Theta \left(\tau_{\min} \leq \frac{M_{q\bar{q}}^2}{s} \right) = \int_0^1 dz_+ dz_- \Gamma_{e^-}(z_+) \Gamma_{e^-}(z_-) \Theta \left(\frac{\tau_{\min}}{z_+ z_-} < 1 \right) \int_{\tau_{\min}/(z_+ z_-)}^1 d\hat{\tau} \frac{d\hat{\sigma}}{d\hat{\tau}}, \quad (12)$$

with the integral of parton-level NLO contribution given by

$$\begin{aligned} \frac{1}{B(\hat{s})} \int_c^1 d\hat{\tau} \frac{d\hat{\sigma}^{[1]}}{d\hat{\tau}} = & -\frac{56}{9} - 4c + \frac{4}{3} \log \frac{\hat{s}}{\mu_R^2} + (4\pi)K_R - 2 \int_c^1 d\hat{\tau} \frac{K_F(\hat{\tau})}{\hat{\tau}} \\ & - 4(1 - c) \log(1 - c) + 4 \log^2(1 - c) + 4\text{Li}_2(c) \\ & + \log \frac{\hat{s}}{\mu_F^2} (1 + 2c + 4 \log(1 - c) - 2 \log c). \quad (13) \end{aligned}$$

The integral of the K_F function in the Δ scheme reads

$$\int_c^1 d\hat{\tau} \frac{K_F^{\Delta}(\hat{\tau})}{\hat{\tau}} = 2\text{Li}_2(c) - c + 2 \log^2(1 - c) + 2c \log(1 - c) - \log(c) - \frac{\pi^2}{3} - 1. \quad (14)$$

We present numerical results for the the cumulative cross section Eq. 12 for the toy model process at $\sqrt{s} = \mu_R = \mu_F = 500$ GeV. Ratios of $\sigma(\tau_{\min})$ for different settings of the PDFs are shown in Fig. 1 and Fig. 2 as a function of τ_{\min} . We find qualitatively similar results in the range $\sqrt{s} \in [50, 500]$ GeV. The region close to $\tau_{\min} = 1$ has to be taken with a grain of salt because it features unresummed purely soft logs.

In Fig. 1 on the left, we show the dependence of the cumulative cross section on the adopted factorisation scheme. Such a dependence is of the order of 10^{-4} – 10^{-3} , to be considered as a systematic error associated to the calculation. Note that the NLL electron PDF largely differs ($\mathcal{O}(1)$) between the $\overline{\text{MS}}$ and the Δ scheme, with the NLL electron PDF in the Δ scheme closer to the LL value¹¹). Hence we can conclude that there are large cancellations between the PDFs and the short-distance cross section in the $\overline{\text{MS}}$ scheme, cancellations which are absent for the Δ scheme. Such beneficial cancellations in the Δ scheme are also evident in the cumulative short-distance cross section, Eq. 13: when inserting Eq. 14 into Eq. 13, we see that the $\log^2(1-c)$ term cancels entirely.

In Fig. 1 on the right, we show the dependence of the cumulative cross section on the adopted renormalisation scheme. By comparing with Fig. 1 on the left, we see that the renormalisation scheme dependence mostly leads to a normalisation effect, and it is significantly larger than the factorisation scheme one. The choice of the renormalisation scheme should be regarded as an informed choice rather than a systematic of the calculation.

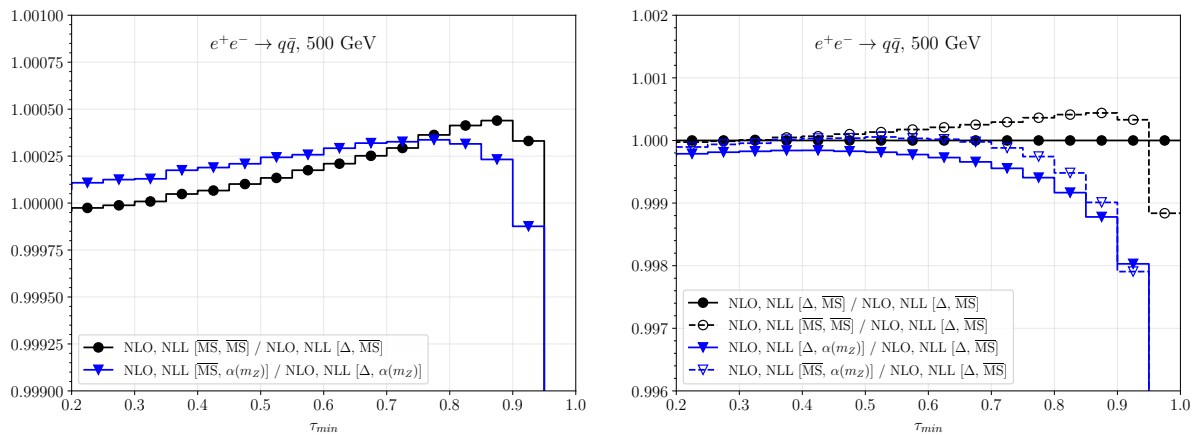


Figure 1: Dependence of the cumulative cross section Eq. 12 for the toy model process on factorisation and renormalisation schemes at $\sqrt{s} = \mu_R = \mu_F = 500$ GeV. Several choices of factorisation and renormalisation schemes for the PDFs are shown. The notation adopted in the legends of the plots is: {accuracy of short-distance cross section}, {accuracy of PDF} [{factorisation scheme}, {renormalisation scheme}]. The accuracy of the short-distance cross section is always NLO.

In Fig. 2, the impact of NLL vs. LL PDFs is shown for three different choices of renormalisation schemes. It is clear that the corrections due to next-to-leading logarithms follow a non-trivial pattern, impossible to account in some universal manner. Hence, NLL-accurate PDFs are phenomenologically important for precision studies.

Note that, despite its simplicity, the toy model process behaves similarly (w.r.t. ISR effects) to the other $2 \rightarrow 2$ processes considered in Ref. 11). We refer the interested reader to Refs. 10, 9, 7, 12, 11) for additional details about predictions at high-energy e^+e^- colliders within collinear factorisation and the usage of NLL PDFs. As a final remark, we would like to stress that moving towards NLL is important not only to improve on the accuracy of our predictions, but also needed for an assessment of sources of theoretical uncertainties.

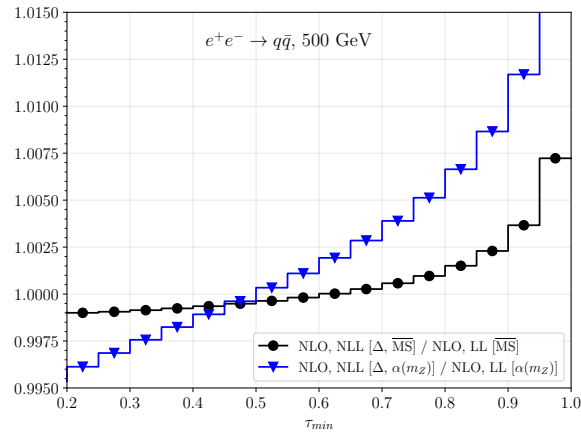


Figure 2: Impact of next-to-leading logarithmic terms in the PDFs. The notation adopted is as in Fig. 1.

1 Acknowledgements

The work presented in this contribution benefited from collaboration with V. Bertone, M. Cacciari, S. Frixione, M. Zaro and X. Zhao, to whom I am grateful. This work has received funding from the Swiss National Science Foundation (SNF) under contract 200020-204200.

References

1. G. Altarelli *et al*, *Nucl. Phys. B* **126** 298 (1977).
2. V.N. Gribov *et al*, *Sov. J. Nucl. Phys.* **15** 438 (1972).
3. L.N. Lipatov, *Yad. Fiz.* **20** 181 (1974).
4. Y.L. Dokshitzer, *Sov. Phys. JETP* **46** 641 (1977).
5. M. Skrzypek *et al*, *Z. Phys. C* **49** 577 (1991).
6. M. Cacciari *et al*, *Europhys. Lett.* **17** 123 (1992).
7. S. Frixione *et al*, 2108.10261.
8. J. Blümlein *et al*, *Mod. Phys. Lett. A* **37** 2230004 (2022) [2202.08476].
9. V. Bertone *et al*, *JHEP* **03** 135 (2020) [1911.12040].
10. S. Frixione, *JHEP* **11** 158 (2019) [1909.03886].
11. V. Bertone *et al*, *JHEP* **10** 089 (2022) [2207.03265].
12. S. Frixione, *JHEP* **07** 180 (2021) [2105.06688].
13. A. Buckley *et al*, *Eur. Phys. J. C* **75** 132 (2015) [1412.7420].
14. J. Alwall *et al*, *JHEP* **07** 079 (2014) [1405.0301].
15. R. Frederix *et al*, *JHEP* **07** 185 (2018) [1804.10017].

HIGH PRECISION QCD PHYSICS AT FCC-EE

Francesco Giuli [On behalf of the FCC collaboration]
*CERN – European Organization for Nuclear Research,
Espl. des Particules 1, 1211 Meyrin, Switzerland*

Abstract

The Future Circular Collider (FCC) is a post-LHC project aiming at direct and indirect searches for physics beyond the SM in a new 100 km tunnel at CERN. In addition, the FCC-ee offers unique possibilities for high-precision studies of the strong interaction in the clean environment provided by e^+e^- collisions, thanks to its broad span of center-of-mass energies ranging from the Z pole to the top-pair threshold, and its huge integrated luminosities yielding 10^{12} and 10^8 jets from Z and W^\pm bosons decays, respectively, as well as 10^5 pure gluon jets from Higgs boson decays. In this contribution, we will summarize studies on the impact the FCC-ee will have on our knowledge of the strong force including: (i) Quantum Chromodynamics (QCD) coupling extractions with per-mille uncertainties, (ii) parton radiation and parton-to-hadron fragmentation functions, (iii) jet properties (light-quark-gluon discrimination, e^+e^- event shapes and multijet rates, jet substructure, etc.), (iv) heavy-quark jets (dead cone effect, charm-bottom separation, gluon $\rightarrow c\bar{c}$, $b\bar{b}$ splitting, etc.); and (v) non-perturbative QCD phenomena (color reconnection, baryon and strangeness production, Bose-Einstein and Fermi-Dirac final-state correlations, etc.).

1 Introduction

A crucial aspect for many physics measurements is a precise understanding of QCD. An accurate determination of the strong coupling constant α_S is mandatory to improve the precision of the production cross sections and decays calculation. The computation of higher-order corrections up to next-to-next-to-next-to-leading order (N³LO) and next-to-next-to-leading logarithm (N²LL) is also central because it can increase the precision in observables predictivity. Another pivotal ingredient is a precise picture of jet substructure, parton showering, hadronization and colour reconnection, whose understanding benefits any hadronic final state.

The FCC- ee program ¹⁾, with its large integrated luminosities and clean environment, offers a rich QCD program. QCD studies with an unprecedented precision can be performed due to the large expected number of events at the FCC- ee of roughly $\sim 10^{11}$ Z at $\sqrt{s} = 91$ GeV, $\sim 10^7$ W^+W^- at $\sqrt{s} = 160$ GeV and $\sim 10^6$ ZH at $\sqrt{s} = 240$ GeV.

2 The strong coupling constant

The least precisely known of all interaction coupling constant is α_S , with an overall uncertainty at per-mille level, $\delta\alpha_S \sim 10^{-3}$. Currently, α_S is determined by comparing 7 experimental observables to perturbative QCD (pQCD) predictions, plus a global average at the Z pole scale. The relevant observable for e^+e^- collisions are e^+e^- jet shapes and hadronic τ leptons and W/Z bosons decays.

2.1 α_S from e^+e^- event shapes and jet rates

As already done at LEP ²⁾, the thrust (τ) and the C -parameter defined in Eq. 1 can be used to extract α_S :

$$\tau = 1 - T = 1 - \max_{\hat{n}} \frac{\sum |\vec{p}_i \cdot \hat{n}|}{\sum |\vec{p}_i|} \quad C = \frac{3 \sum_{i,j} |\vec{p}_i| |\vec{p}_j| \sin^2 \theta_{i,j}}{2 (\sum_i |\vec{p}_i|)^2}, \quad (1)$$

with $\theta_{i,j}$ the angle between particle i and j and $\vec{p}_{i,j}$ the momentum respectively. Other quantities which are sensitive to α_S are the n -jet rates, $R_n = \frac{\sigma_{n\text{-jet}}}{\sigma_{\text{tot}}}$, and therefore were used to extract the strong coupling constant. The comparison between the experimental measurements and N³LO+N²LL predictions yields $\alpha_S(m_Z) = 0.1171 \pm 0.0027$ ($\pm 2.6\%$).

At lower \sqrt{s} , the n -jet rates up to 7 jets could be studied ³⁾, while runs at higher \sqrt{s} could be used to study jet rates in regimes where the probability of hard gluon emission increases. Moreover, a better understanding of hadronization mechanism and improvements in logarithmic resummation to N³LL for jet rates would allow the extraction of α_S at $\delta\alpha_S/\alpha_S < 1\%$ at the FCC- ee .

2.2 α_S from hadronic τ decays

The very precise LEP and B-factories $e^+e^- \rightarrow \tau^+\tau^-$ data, together with higher-order pQCD corrections to the hadronic τ width, allow a remarkably accurate α_S extraction from hadronic τ decays. The quantity of interest is the ratio of the hadronic τ width and the electron τ width, defined as follows:

$$R_\tau = \frac{\Gamma(\tau^- \rightarrow \nu_\tau + \text{hadrons})}{\Gamma(\tau^- \rightarrow \nu_\tau e^- \bar{\nu}_e)} = S_{\text{EW}} N_C \left(1 + \sum_{n=1}^4 c_n \left(\frac{\alpha_S}{\pi} \right)^n + \mathcal{O}(\alpha_S^5) + \delta_{\text{np}} \right), \quad (2)$$

where S_{EW} represents the pure electroweak (EW) contribution to the ratio, N_C the number of colours, c_n the coefficients of the perturbative expansion, and δ_{np} power-suppressed non-perturbative (NP) corrections. Experimentally, this ratio has determined with a $\pm 0.23\%$ precision, and this leads to a determination of $\alpha_S(m_Z) = 0.1187 \pm 0.0018$ ($\pm 1.5\%$).

The dominant source of theoretical uncertainty in the extraction of α_S comes from the discrepancy between the Fixed Order Perturbation Theory (FOPT) and the Contour-Improved Perturbation Theory (CIPT), two different approaches for evaluating the perturbative expansion. Currently, this uncertainty is at the level of $\pm 1.5\%$. NP correction are also relevant in the determination of α_S from hadronic τ decays. These can be sizeable for $\mathcal{O}(\Lambda_{\text{QCD}}^2/m_\tau^2)$ and they can be controlled by new high-precision measurements of the hadronic τ spectral function.

Statistical uncertainty will be negligible at the FCC- ee , considering the $\sim 10^{11}$ τ produced at the Z -pole, and parametric and systematic uncertainties will dominate. To fully exploit this huge statistics,

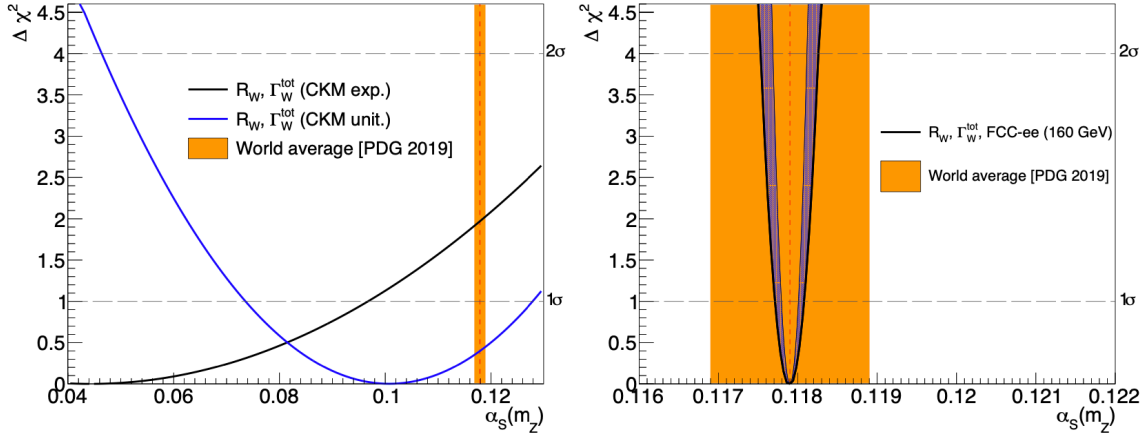


Figure 1: $\Delta\chi^2$ fit profiles of the $\alpha_S(m_Z)$ extracted from the combined N³LO analysis of the total W width (Γ_W^{tot}) and hadronic-to-leptonic W^\pm decay ratio (R_W), compared to the current $\alpha_S(m_Z)$ world average (vertical orange band). Left: Extraction with the present W^\pm data assuming (blue curve) or not (black curve) CKM unitarity. Right: Extraction expected at the FCC- ee , with the total (experimental, parametric, and theoretical in quadrature) uncertainties (outer parabola) and with the experimental uncertainties alone (inner parabola). These plots are taken from Ref. ⁴.

a reduction in the spread of theoretical determinations of R_τ is mandatory. This necessarily implies a better understanding of the discrepancies arising from the CIPT and FOPT comparison. Furthermore, a better determination of the spectral functions entering the R_τ calculation is compulsory, and this can be achieved exploiting new data coming from Belle II or the FCC- ee itself. In this way, the uncertainty on α_S can be reduced well below the current $\delta\alpha_S/\alpha_S \sim 1\%$ level.

2.3 α_S from hadronic W^\pm boson decays

Analogously to the case of the hadronic τ decays, the extraction of α_S from hadronic W^\pm boson decays can be performed considering the ratio of the hadronic width to the lepton width, as described in Eq. 3

$$R_W(Q) = \frac{\Gamma_W^{\text{had.}}(Q)}{\Gamma_W^{\text{lep.}}(Q)} = R_W^{\text{EW}} \left(1 + \sum_{i=1}^4 a_i(Q) \left(\frac{\alpha_S(Q)}{\pi} \right)^i + \mathcal{O}(\alpha_S^5) + \delta_{\text{mix}} + \delta_{\text{np}} \right) \quad (3)$$

with R_W^{EW} representing the pure EW contribution to the ratio, $a_i(Q)$ the coefficients of the perturbative expansion, δ_{mix} the mixed QCD+EW corrections, and δ_{np} the power-suppressed NP corrections. α_S is then extracted at N³LO from a simultaneous fit of 2 W boson pseudo-observables ⁴): R_W and Γ_W^{tot} . With the assumption of CKM unitarity, a value of $\alpha_S(m_Z) = 0.101 \pm 0.027$ is obtained (with negligible theoretical and parametric uncertainties), as depicted in Fig. 1 (left). The large uncertainty is mostly due to the poor experimental knowledge of R_W and Γ_W^{tot} , which have been measured in $e^+e^- \rightarrow W^+W^-$ LEP events. If CKM unitarity is not assumed, the resulting value of the strong coupling constant is basically unconstrained, as shown in Fig. 1 (left).

At the FCC- ee , the uncertainties on R_W and Γ_W^{tot} will be largely reduced, thanks to the high statistics at the WW threshold. With a factor of 10 reduction of the theoretical uncertainties due to missing $\alpha_S^5, \alpha^3, \alpha\alpha_S^2$ and $\alpha^2\alpha_S$ corrections, a final QCD coupling extraction of $\alpha_S(m_Z) = 0.11790 \pm 0.00023$ with 2 per-mille total error is possible, as illustrated in Fig. 1 (right).

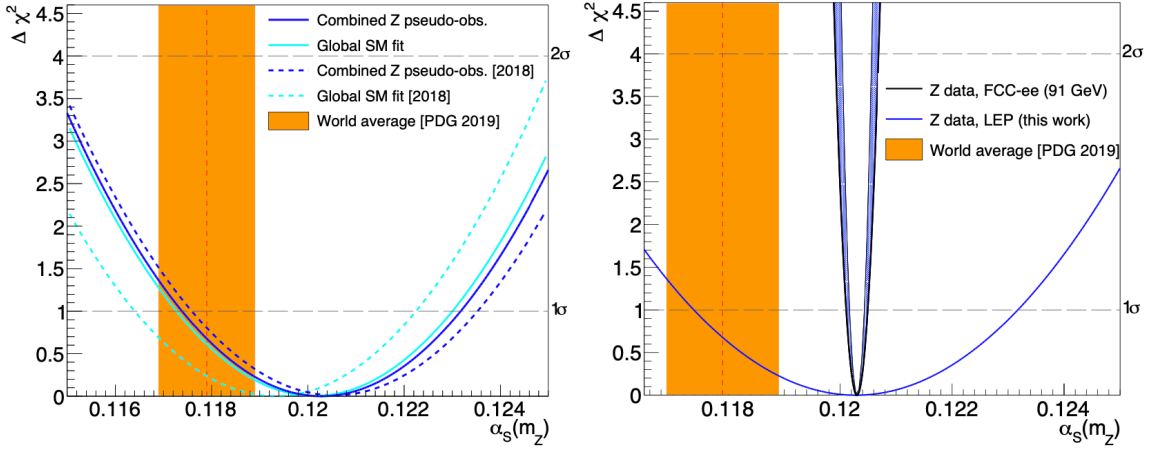


Figure 2: $\Delta\chi^2$ fit profiles of $\alpha_S(m_Z)$ extracted from the combined Z pseudo-observables analysis and/or the global SM fit compared to the current world average (orange band). Left: Current results (solid lines) compared to the previous 2018 fit (dashed lines). Right: Extraction expected at the FCC- ee - with central value (arbitrarily) set to $\alpha_S(m_Z) = 0.12030$ and total (experimental, parametric, and theoretical in quadrature) uncertainties (outer parabola) and experimental uncertainties alone (inner parabola) – compared to the present one from the combined Z data (blue line). These plots are taken from Ref. ⁴⁾.

2.4 α_S from hadronic Z boson decays

Following the same procedure described in Sec. 2.3, α_S can be extracted at N³LO from a simultaneous fit of 3 Z boson pseudo-observables ⁴⁾: R_Z , $\Gamma_Z^{\text{tot.}}$ and $\sigma_Z^{\text{had.}}$, yielding $\alpha_S = 0.1203 \pm 0.0029$ ($\pm 2.3\%$), as depicted in Fig. 2 (left).

Having 10^5 times more Z bosons than at LEP, together with an exquisite systematic and parametric precision would allow a remarkable improvement in the theoretical predictions of the Z boson pseudo-observables, and therefore a reduction in the strong coupling uncertainty by almost 2 orders of magnitude. This experimental precision has to be matched by a reduction in the theoretical uncertainties by almost a factor of 5 by computing missing α_S^5 , α^3 , $\alpha\alpha_S^2$ and $\alpha^2\alpha_S$ corrections. In this way, α_S can be extracted with a 2 per-mille accuracy, namely $\alpha_S(m_Z) = 0.11790 \pm 0.00023$, as reported in Fig. 2 (right).

3 Jet substructure

Jet substructure studies play a crucial role in improving our knowledge of parton shower (PS) and hadronization mechanism ^{5, 6, 7)}. In particular, jet angularities ⁸⁾, defined as $\lambda_\beta^\kappa = \sum_{i \in \text{jet}} z_i^\kappa \theta_i^\beta$ (with z_i and θ_i representing the energy fraction and angular distance to jet axis of constituent i), constitute an intriguing starting point. The parameters $\kappa \geq 0$ and $\beta \geq 0$ regulate the energy and angular weighting respectively. Multiplicity ($\kappa = 0$, $\beta = 0$), width ($\kappa = 1$, $\beta = 1$), mass ($\kappa = 1$, $\beta = 2$), p_T^D ($\kappa = 0$, $\beta = 2$) and Les Houches Angularity ($\kappa = 1$, $\beta = 0.5$) are the most common examples. Specifically, this last quantity offers an incredible opportunity to study different PS algorithms between generators.

The FCC- ee would be crucial in addressing such differences in PS and hadronization modelling. For example, the gluon radiation patterns could be studied exploiting the expected 10^6 $e^+e^- \rightarrow ZH(\rightarrow gg)$ events, together with the $e^+e^- \rightarrow Z \rightarrow b\bar{b}g$ events (assuming that b -jets are tagged with high efficiency). Therefore, these studies conducted at the FCC- ee would lead directly to improved MC tuning, together

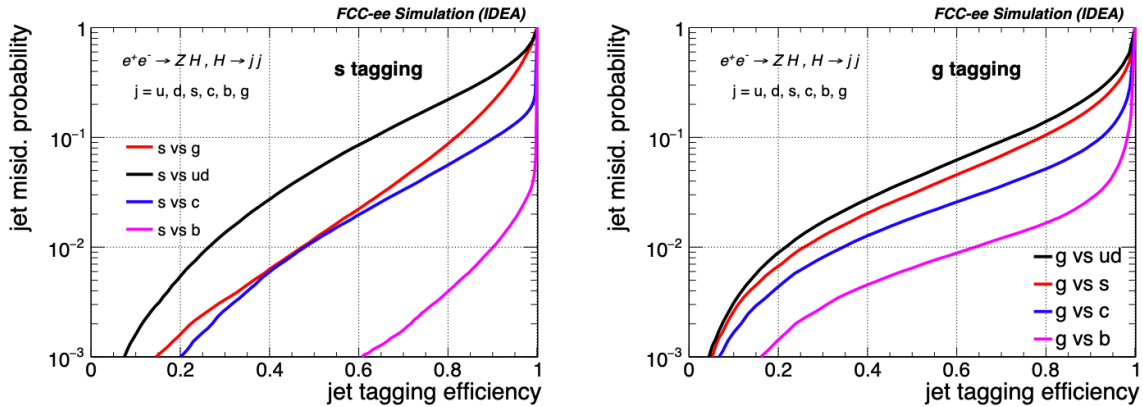


Figure 3: Evaluation of `ParticleNetIdea` performance in terms of a receiver operating characteristic (ROC) curve for the identification of different jet flavours i.e., s (left), and g (right). The different jet flavours considered background are indicated on the labels. The IDEA detector configuration is used. These plots are taken from Ref. ¹⁴⁾.

with a better understanding of NP QCD.

4 Quark-gluon tagging

One of the most exciting (but challenging) prospects in pp collisions is light-quark gluon discrimination. Being able to efficiently identify the flavour of the parton which initiates the jet is critical for the success of the physics program of future EW factories ⁹⁾. An accurate light quark-gluon discrimination would allow precise Beyond the Standard Model (BSM) searches for signals without leptons, b - or top-quarks, as well as would produce an enhancement of light quark-rich signals i.e. $t\bar{t}H$ or pure EW $W/Z +$ jets. Recently, a new generation of advanced machine learning based jet tagging algorithms has been developed ^{10, 11, 12, 13)}, bringing almost 2 orders of magnitude improvement in background rejection when comparing to the traditional approaches in Heavy Flavour and gluon tagging. In particular, within the context of the FCC-ee, the `ParticleNetIdea` ¹⁴⁾ has been developed, and Figure 3 shows its high performances in discriminating light quark jets from s -quark (left) and gluons (right).

5 Conclusion

To fully exploit present and future collider programs, a precise understanding of both perturbative and NP QCD is highly needed. At the FCC-ee, a plethora of unique QCD studies would be possible. Among them, the most relevant are the extraction of the strong coupling constant α_S from jet event shapes and hadronic $\tau/W^\pm/Z$ decays with a per mille level accuracy and jet substructure studies, which could greatly improve our current knowledge of parton shower and hadronization. Thanks to the large pure quark/gluon samples in the extremely clean environment of a lepton collider, precise quark-gluon discrimination studies would be carried out with a much better discriminating power than the one in $p\bar{p}/pp$ collisions. Finally, due to the large number of expected $e^+e^- \rightarrow W^+W^-$, the huge statistics ($\times 10^4$ LEP) could be exploited to measure the W boson mass, m_W , both (semi-)leptonically and hadronically to constrain colour reconnection at the 1% level or below.

References

1. FCC Collaboration, [arXiv:2203.08310 [physics.acc-ph]].
2. G. Dissertori *et al.*, JHEP **08** (2009), 036 doi:10.1088/1126-6708/2009/08/036 [arXiv:0906.3436 [hep-ph]].
3. D. d'Enterria *et al.*, [arXiv:1512.05194 [hep-ph]].
4. D. d'Enterria and V. Jacobsen, [arXiv:2005.04545 [hep-ph]].
5. D. Krohn *et al.*, JHEP **02** (2010), 084 doi:10.1007/JHEP02(2010)084 [arXiv:0912.1342 [hep-ph]].
6. S. D. Ellis *et al.*, Phys. Rev. D **80** (2009), 051501 doi:10.1103/PhysRevD.80.051501 [arXiv:0903.5081 [hep-ph]].
7. J. M. Butterworth *et al.*, Phys. Rev. Lett. **100** (2008), 242001 doi:10.1103/PhysRevLett.100.242001 [arXiv:0802.2470 [hep-ph]].
8. A. J. Larkoski *et al.*, JHEP **11** (2014), 129 doi:10.1007/JHEP11(2014)129 [arXiv:1408.3122 [hep-ph]].
9. P. Azzi *et al.*, Eur. Phys. J. Plus **137** (2022) no.1, 39 doi:10.1140/epjp/s13360-021-02223-z [arXiv:2107.05003 [hep-ex]].
10. ATLAS Collaboration, JINST **11** (2016) no.04, P04008 doi:10.1088/1748-0221/11/04/P04008 [arXiv:1512.01094 [hep-ex]].
11. CMS Collaboration, JINST **15** (2020) no.06, P06005 doi:10.1088/1748-0221/15/06/P06005 [arXiv:2004.08262 [hep-ex]].
12. ATLAS Collaboration, ATL-PHYS-PUB-2017-003.
13. E. Bols *et al.*, JINST **15** (2020) no.12, P12012 doi:10.1088/1748-0221/15/12/P12012 [arXiv:2008.10519 [hep-ex]].
14. F. Bedeschi *et al.*, Eur. Phys. J. C **82** (2022) no.7, 646 doi:10.1140/epjc/s10052-022-10609-1 [arXiv:2202.03285 [hep-ex]].

NON COMMUTATIVITY BETWEEN MASSLESS AND THRESHOLD LIMIT IN PROCESSES WITH HEAVY QUARKS

Andrea Ghira

Dipartimento di Fisica, Universit degli Studi di Genova and INFN, Via Dodecaneso 33, 16146, Italy

Abstract

Processes involving heavy quarks can be computed in perturbation theory in two different ways: we can adopt a scheme in which the mass of the quark is considered only as a regulator of the collinear divergences because of the fact that the hard scale of the process is far bigger or we can consider the quark as a massive particle. Each picture has its own advantages and drawbacks: we investigate the differences between the two approaches with particular attention to the threshold logarithmic structure. We examine the origin of this difference, focusing on different processes involving the Higgs boson. Finally we perform the soft logs resummation of the Higgs boson decay rate into a $b\bar{b}$ pair at NLL accuracy in the massive scheme.

1 Introduction

Quarks appear in the Quantum Chromo-Dynamics (QCD) lagrangian in different species, named flavours. From the point of view of strong interactions, different flavours are distinguished purely on the basis of the value of their masses. It is therefore natural to classify quark flavours according to their masses, compared to $\Lambda_{\text{QCD}} \simeq 300\text{MeV}$. The masses of up, down and strange quarks, relevant for ordinary matter, are much smaller than Λ_{QCD} , and can be taken to be zero for most applications in high-energy physics, on the other hand charm (c) and especially bottom (b) are heavy according to this definition. Heavy-flavour production cross-sections can be calculated in perturbative QCD because the mass of the b and c quarks sets the value of the coupling in the perturbative region and regulates collinear singularities. In order to compute processes involving heavy flavour two main approaches are employed. In the so-called *massive scheme*, the final-state heavy quarks are considered massive particles and we can compute order by order in perturbation theory the scattering amplitude. Within this approach the kinematics is treated correctly but calculations become cumbersome at higher and higher perturbative orders. Another drawback is that

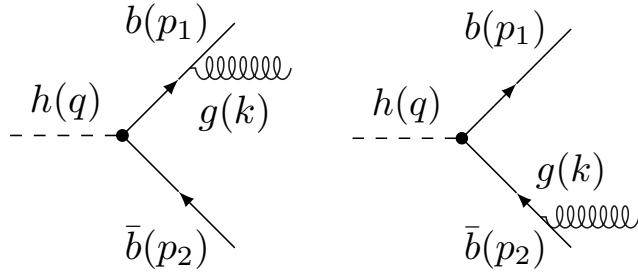


Figure 1: Real-emission contributions to the decay of the Higgs boson into a $b\bar{b}$ pair at $\mathcal{O}(\alpha_s)$.

large mass logarithms which arise due to the fact that the mass of the heavy quark is far smaller than hard scale of the process spoil the convergence of the perturbative series. Therefore another framework is employed which is the so called *massless scheme*. In the massless scheme, we treat the mass of the particle only as a regulator of the collinear divergences. Consequently we do not have control on the kinematics outside the collinear region, i.e. we consider only radiation emitted at small angle. This approach exploits the factorization theorem: the differential cross section can be written as a convolution product of a process dependent function times a fragmentation function, which is process independent and fulfills a first order linear equation that allows us to resum the mass logarithms (DGLAP). The initial condition of the DGLAP evolution equation is set at a scale $\mu_0^2 \simeq m_{c,b}^2 \gg \Lambda_{\text{QCD}}^2$ and therefore it is in the perturbative domain and it can be determined by matching the factorisation theorem with the massive scheme. It was determined to NLO in QCD for the b quark fragmentation function in ^{1, 2)} and to NNLO in ^{3, 4)}. The initial condition is affected by soft-collinear logarithms, that should be resummed to all-orders too ^{5, 6)}. The main problem we want to focus on is that the structure of threshold logarithms in the initial condition of the fragmentation function cannot be always recovered by the massless limit of a massive-framework calculation: this strongly depends both on the considered process and on the specific observable that is computed. We will show this particular behaviour using a simple process as an example which is the decay of a Higgs boson in a $b\bar{b}$ pair. Secondly, we want to derive a resummed expression of the differential decay rate at NLL accuracy that fully take into account the heavy quark mass and outline also in this case the non commutativity of the massless and threshold limit.

2 Interplay between threshold and massless limit in $H \rightarrow b\bar{b}$

In order to explain the aforementioned non commutativity of the limits we focus on the decay of the Higgs boson at NLO keeping the mass of the quarks:

$$h(q) \rightarrow b(p_1) + \bar{b}(p_2) + g(k) \quad p_1^2 = p_2^2 = m^2, \quad k^2 = 0. \quad (1)$$

We compute the differential decay rate $d\Gamma/dx$, where $x = (2p_1 \cdot q)/q^2$ is the energy of the quark in the CoM reference frame, and we are interested in the small mass limit necessary for the massless scheme ($m^2/|q^2| \equiv \xi \rightarrow 0$) and in the limit $x \rightarrow 1$. This limit can be achieved both when the gluon becomes soft or when it is emitted collinear respect to the emitting quark provided that the latter is massless. We are

interested in performing these limits in two different orders¹

$$\begin{aligned} \lim_{\xi \rightarrow 0} \lim_{x \rightarrow 1} \frac{1}{\Gamma_0} \frac{d\Gamma}{dx} &= -\frac{2\alpha_s C_F}{\pi} \left[\frac{1 + \log \xi}{1-x} + \mathcal{O}(\xi^0) + \mathcal{O}((1-x)^0) \right], \\ \lim_{x \rightarrow 1} \lim_{\xi \rightarrow 0} \frac{1}{\Gamma_0} \frac{d\Gamma}{dx} &= -\frac{\alpha_s C_F}{\pi} \left[\frac{\log \xi}{1-x} + \frac{\log(1-x)}{1-x} + \frac{7}{4} \frac{1}{1-x} + \mathcal{O}(\xi^0) + \mathcal{O}((1-x)^0) \right], \end{aligned} \quad (2)$$

where Γ_0 is the Born level decay rate:

$$\Gamma_0 = \frac{\sqrt{2q^2} G_F m^2 \beta^3 N_C}{8\pi}, \quad \beta = \sqrt{1-4\xi}, \quad (3)$$

with G_F is the Fermi constant. In order to analyze the logarithmic structure of the previous equation, we introduce the Mellin transformation:

$$\mathcal{M}\{f(x)\}(N) = \int_0^1 x^{N-1} f(x) dx \quad (4)$$

We notice that in the first case of equation (2) we have a mass logarithm multiplied by a soft one ($1/(1-x) \leftrightarrow \log N$ in Mellin space) whereas in the second one we have an additional term which corresponds to a $\log^2 N$ after the Mellin transformation. We note also that the overall coefficient is halved in the second limit, as if the $\log(1-x)$ contribution in the second line of (2) is playing the role of a mass logarithm. We would like to provide a physical interpretation to this fact: a measurement of x fixes the invariant mass $(p_2 + k)^2 = m_{g\bar{b}}^2$ thus screening one of the collinear (mass) logs and preventing the anti-quark propagator to go on-shell. In order to analyse the actual origin of the double logarithms, we have to look at the quark propagator: if we integrate it over the angle between the gluon and the quark in the $\vec{p}_2 + \vec{k} = 0$ frame we find

$$\int_{-1}^1 \frac{1}{1 - \beta_1 \cos \theta} d\cos \theta = \log \frac{x^2}{\xi(1-x)} + \mathcal{O}((1-x)^0), \quad \beta_1 = \frac{x\sqrt{1-4\xi/x^2}}{x-2\xi}, \quad (5)$$

where β_1 is the quark velocity in that reference frame. In this limit, collinear logarithms appear in two distinct ways: as explicit logarithm of the quark mass m or as logarithms of $1-x$. This consideration brings us to formulate a more general statement about the double threshold logs in processes with heavy quark. We expect this behaviour to arise if look at a differential distribution which is directly related to the virtuality of one of the propagators, here $m_{g\bar{b}}^2$. Let us consider the differential distribution in $\bar{x} = (p_1 + p_2)^2/q^2 \rightarrow 1$ as $k \rightarrow 0$. Performing an explicit calculation:

$$\lim_{\xi \rightarrow 0} \lim_{\bar{x} \rightarrow 1} \frac{1}{\Gamma_0} \frac{d\Gamma}{d\bar{x}} = \lim_{\bar{x} \rightarrow 1} \lim_{\xi \rightarrow 0} \frac{1}{\Gamma_0} \frac{d\Gamma}{d\bar{x}} = -\frac{2\alpha_s C_F}{\pi} \frac{1 + \log \xi}{1-\bar{x}} + \mathcal{O}(\xi^0) + \mathcal{O}((1-x)^0), \quad (6)$$

In this case we have only a single logarithmic enhancement and the two limits commute.

2.1 Higgs Production and Higgs DIS

We test our statement by studying other processes related by crossing symmetry to the Higgs boson decay, i.e Higgs boson production and Higgs DIS. In the Higgs production $b(p_1) + \bar{b}(p_2) \rightarrow h(q) + g(k)$,

¹It is worth to mention that if the massless limit is taken first, $x \rightarrow 1$ corresponds the soft-collinear limit, otherwise only to the soft one.

we are differential in $\tau = (p_1 + p_2)^2/q^2$, which is not related to the virtuality of the propagators. In this case we find that the limits commute, as expected:

$$\lim_{\tau \rightarrow 1} \lim_{\xi \rightarrow 0} \frac{1}{\sigma_0} \frac{d\sigma}{d\tau} = \lim_{\xi \rightarrow 0} \lim_{\tau \rightarrow 1} \frac{1}{\sigma_0} \frac{d\sigma}{d\tau} = -\frac{2\alpha_s C_F}{\pi} \frac{1 + \log \xi}{1 - \tau} + \mathcal{O}(\xi^0) + \mathcal{O}((1 - \tau)^0), \quad (7)$$

$$\sigma_0 = \frac{\sqrt{2}G_F m^2 \beta \pi N_C}{18s}.$$

Finally we study the differential distribution $\frac{d\sigma}{dx_B}$ with $x_B = \frac{-q^2}{2p_1 \cdot q}$ for the real emission corrections to the process $b(p_1) + h(q) \rightarrow b(p_2) + g(k)$. Due to the fact that x_B is related to the virtuality of one of the propagator we expect that the limit do not commute. Indeed we find:

$$\lim_{x_B \rightarrow 1} \lim_{\xi \rightarrow 0} \frac{1}{\bar{\sigma}_0} \frac{d\sigma}{dx_B} = -\frac{\alpha_s C_F}{\pi} \left[\frac{\log \xi}{1 - x_B} + \frac{\log(1 - x_B)}{1 - x_B} + \frac{7}{4} \frac{1}{1 - x_B} + \mathcal{O}(\xi^0) + \mathcal{O}((1 - x_B)^0) \right], \quad (8)$$

$$\lim_{\xi \rightarrow 0} \lim_{x_B \rightarrow 1} \frac{1}{\bar{\sigma}_0} \frac{d\sigma}{dx_B} = -\frac{2\alpha_s C_F}{\pi} \frac{1 + \log \xi}{1 - x_B} + \mathcal{O}(\xi^0) + \mathcal{O}((1 - x_B)^0),$$

$$\bar{\sigma}_0 = \frac{\pi \sqrt{2} G_F m^2 N_C \eta}{-3q^2}, \quad \eta = \sqrt{1 + 4\xi}.$$

3 Soft Resummation in the Massive Scheme

In this section we want to give an explicit expression for the all-order soft resummation of the Higgs decay rate in a $b\bar{b}$ pair at NLL accuracy in the massive scheme. Since we look at the differential distribution over x , we are in class of process with the so called single-particle inclusive kinematics (see ⁷⁾). The main result of ⁷⁾ is that the resummed expression can be factorized as a product of a soft function times a hard function times a jet function for every masses particle n the final state. In our case the resummation formula simplifies considerably there are not massless particles. The resummed result of ⁷⁾ at NLL, adapted to the process we are considering, reads²

$$\tilde{\Gamma}(N, \xi) = \left(1 + \frac{\alpha_s}{\pi} C^{(1)}(\xi) + \mathcal{O}(\alpha_s^2) \right) e^{-2 \int_{1/\bar{N}}^1 \frac{dz}{z} \left[\frac{\alpha_s(z^2 q^2)}{\pi} \gamma_{\text{soft}}^{(0)}(\beta) + \left(\frac{\alpha_s(z^2 q^2)}{\pi} \right)^2 \gamma_{\text{soft}}^{(1)}(\beta) + \mathcal{O}(\alpha_s^3) \right]}$$

$$+ \mathcal{O}\left(\frac{1}{\bar{N}}\right), \quad (9)$$

with $\bar{N} = N e^{\gamma_E}$ and γ_{soft} the massive soft anomalous dimension. To this logarithmic accuracy we need the two loops expression of the running coupling, the coefficients $\gamma_{\text{soft}}^{(0)}$, $\gamma_{\text{soft}}^{(1)}$ and $C^{(1)}$. The first order soft anomalous dimension can be obtained from the calculation of one gluon emission in the eikonal limit:

$$\gamma_{\text{soft}}^{(0)}(\beta) = C_F \left[\frac{1 + \beta^2}{2\beta} \log\left(\frac{1 + \beta}{1 - \beta}\right) - 1 \right], \quad (10)$$

²We are not so sure about the argument of the running coupling, since in ⁷⁾ $\alpha_s(z^2 q^2)$ is used, on the other hand it seems that in ⁸⁾ $\alpha_s(z^2 m^2)$ is used.

while the second order was presented in 8)³:

$$\begin{aligned}
\gamma_{\text{soft}}^{(1)} = & \left\{ \frac{K}{2} + \frac{C_A}{2} \left[-\frac{1}{3} \log^2 \frac{1-\beta}{1+\beta} + \log \frac{1-\beta}{1+\beta} - \zeta_2 \right] \right. \\
& + \frac{(1+\beta^2)}{4\beta} C_A \left[\text{Li}_2 \left(\frac{(1-\beta)^2}{(1+\beta)^2} \right) + \frac{1}{3} \log^2 \frac{1-\beta}{1+\beta} + \zeta_2 \right] \left. \right\} \gamma_{\text{soft}}^{(0)}(\beta) \\
& + C_F C_A \left\{ \frac{1}{2} + \frac{1}{2} \log \frac{1-\beta}{1+\beta} + \frac{1}{3} \log^2 \frac{1-\beta}{1+\beta} - \frac{(1+\beta^2)^2}{8\beta^2} \left[-\text{Li}_3 \left(\frac{(1-\beta)^2}{(1+\beta)^2} \right) + \zeta_3 \right] \right. \\
& \left. - \frac{(1+\beta^2)}{2\beta} \left[\log \frac{1-\beta}{1+\beta} \log \frac{(1+\beta)^2}{4\beta} - \frac{1}{6} \log^2 \frac{1-\beta}{1+\beta} - \text{Li}_2 \left(\frac{(1-\beta)^2}{(1+\beta)^2} \right) \right] \right\}, \tag{11}
\end{aligned}$$

with $K = C_A \left(\frac{67}{18} - \zeta_2 \right) - \frac{5n_f}{9}$. The coefficient $C^{(1)}$ is instead process-dependent, as it receives contributions from both the end-point of the real emission and from the virtual corrections (computed in the on-shell scheme). Writing the real emission differential decay rate as:

$$\frac{d\Gamma^{(R)}}{dx} = \frac{\alpha_s C_F}{\pi} \Gamma_0^{(d)} \frac{f_\varepsilon \left(x, \xi, \frac{q^2}{\mu^2} \right)}{(1-x)^{1+2\varepsilon}}, \quad \Gamma_0^{(d)} = \Gamma_0 \frac{\pi^{\frac{5-d}{2}}}{2^{d-3} \Gamma \left(\frac{d-1}{2} \right)} \left(\frac{4\mu^2}{q^2 \beta^2} \right)^{\frac{4-d}{2}}, \tag{12}$$

the coefficient $C^{(1)}$ can be determined using the fact that virtual corrections are proportional to $\delta(1-x)$ and the identity between distributions:

$$\begin{aligned}
\frac{f_\varepsilon \left(x, \xi, \frac{q^2}{\mu^2} \right)}{(1-x)^{1+2\varepsilon}} = & \delta(1-x) \left[-\frac{f_0(1, \xi)}{2\varepsilon} + f_0(1, \xi) \log(1-2\sqrt{\xi}) - \frac{1}{2} \frac{d}{d\varepsilon} f_\varepsilon \left(1, \xi, \frac{q^2}{\mu^2} \right) \Big|_{\varepsilon=0} \right] \\
& + \frac{f_0(x, \xi)}{(1-x)_+} + \mathcal{O}(\varepsilon). \tag{13}
\end{aligned}$$

Summing up virtual and real contributions we obtain:

$$\begin{aligned}
C^{(1)}(\xi) = & \frac{C_F}{2} \left\{ -2 \frac{\gamma_{\text{soft}}^{(0)}(\beta)}{C_F} \left[-2 \log \left(1 - \sqrt{1-\beta^2} \right) + \log \frac{m^2}{q^2} + \log \left(\frac{1-\beta^2}{4} \right) + 1 \right] - 2 \right. \\
& + 2L(\beta) \left(\frac{1-\beta^2}{\beta} \right) + \frac{1+\beta^2}{\beta} \left[\frac{1}{2} L(\beta) \log \left(\frac{1-\beta^2}{4} \right) + 2L(\beta)(1-\log \beta) + 2\text{Li}_2 \left(\frac{1-\beta}{1+\beta} \right) \right. \\
& \left. \left. + L(\beta)^2 + L(\beta) \log \frac{1-\beta}{2} + \frac{2}{3} \pi^2 - \frac{1}{2} \left(\text{Li}_2 \left(\frac{4\beta}{(1+\beta)^2} \right) - \text{Li}_2 \left(\frac{-4\beta}{(1-\beta)^2} \right) \right) \right] \right\}, \tag{14}
\end{aligned}$$

with $L(\beta) = \log \left(\frac{1+\beta}{1-\beta} \right)$. We note that the non commutativity of the soft and massless limits has consequences for the resummed expression in the massive scheme: In the small ξ limit we find:

$$\alpha_s C^{(1)}(\xi) = \alpha_s C_F \left(\frac{1}{2} \log^2 \xi + \log \xi + \mathcal{O}(\xi^0) \right).$$

We have a double log of the mass in disagreement with DGLAP evolution equation. The problem is that equation (13) does not hold if we perform the massless limit because in this limit $f_0(1, \xi)$ is not defined. In a certain way we can say that double mass logarithms in the soft limit of the massive calculation

³It is worth to mention that there is a mismatch in the literature between 8) and 9)

and double threshold logarithms of the massless scheme are connected. A well defined expression in the massless limit can be obtained rewriting the differential decay rate as:

$$\frac{1}{\Gamma_0} \frac{d\Gamma}{dx} = \delta(1-x) + \frac{\alpha_s}{\pi} \left[C_F \left(\frac{f_0(x, \xi)}{1-x} \right)_+ + A(\xi) \delta(1-x) \right], \quad (15)$$

The delta coefficient has an expected behaviour for $\xi \rightarrow 0$

$$A(\xi) = C_F \frac{3}{2} \log \xi + \mathcal{O}(\xi^0). \quad (16)$$

4 Conclusions

We have considered observables with different kinematics in processes involving heavy quarks, and in all processes we have computed NLO corrections taking into account the mass dependence of the square amplitude. We have underlined that soft and massless do not always commute, in particular in the massless limit the structure of the distributions can radically change because of the presence of double logs of N . We have traced back the origin of this particular behaviour to the interplay between the observable we are computing and the fermionic propagators in the scattering amplitudes. Finally, we have focused on the massive scheme resummation of the process $H \rightarrow b\bar{b}$ in the soft limit (in this case $x \rightarrow 1$ is only the soft limit because we have taken into account all the mass dependence) and we have found that within this approach double logarithms of the mass may appear, and the origin of this surprising behaviour can be lead back again to the non commutativity between the large N and small mass limit.

An interesting phenomenological study, in the context of heavy-quark calculations, would be combine the massive scheme with the massless one where also soft-collinear logarithms are resummed. The merging of the two becomes far from trivial because of the lack of commutativity of the limits. One would like to design an all-order matching scheme that takes into account both the different logarithmic behaviour that arises in the two cases.

5 Acknowledgements

We thank Simone Marzani and Giovanni Ridolfi for the aid in the drafting of this proceeding, which is entirely based on ¹⁰).

References

1. B. Mele and P. Nason, Nucl. Phys. B **361** (1991), 626-644 [erratum: Nucl. Phys. B **921** (2017), 841-842] doi:10.1016/0550-3213(91)90597-Q
2. B. Mele and P. Nason, Phys. Lett. B **245** (1990), 635-639 doi:10.1016/0370-2693(90)90704-A
3. K. Melnikov and A. Mitov, Phys. Rev. D **70** (2004), 034027 doi:10.1103/PhysRevD.70.034027 [arXiv:hep-ph/0404143 [hep-ph]].
4. A. Mitov, Phys. Rev. D **71** (2005), 054021 doi:10.1103/PhysRevD.71.054021 [arXiv:hep-ph/0410205 [hep-ph]].
5. M. Cacciari and S. Catani, Nucl. Phys. B **617** (2001), 253-290 doi:10.1016/S0550-3213(01)00469-2 [arXiv:hep-ph/0107138 [hep-ph]].

6. F. Maltoni, G. Ridolfi, M. Ubiali and M. Zaro, JHEP **10** (2022), 027 doi:10.1007/JHEP10(2022)027 [arXiv:2207.10038 [hep-ph]].
7. E. Laenen, G. Oderda and G. F. Sterman, Phys. Lett. B **438** (1998), 173-183 doi:10.1016/S0370-2693(98)00960-5 [arXiv:hep-ph/9806467 [hep-ph]].
8. N. Kidonakis, Phys. Rev. Lett. **102** (2009), 232003 doi:10.1103/PhysRevLett.102.232003 [arXiv:0903.2561 [hep-ph]].
9. A. von Manteuffel, R. M. Schabinger and H. X. Zhu, Phys. Rev. D **92** (2015) no.4, 045034 doi:10.1103/PhysRevD.92.045034 [arXiv:1408.5134 [hep-ph]].
10. D. Gaggero, A. Ghira, S. Marzani and G. Ridolfi, JHEP **09** (2022), 058 doi:10.1007/JHEP09(2022)058 [arXiv:2207.13567 [hep-ph]].

WEIGHING THE TOP WITH ENERGY CORRELATORS

Massimiliano Procura

University of Vienna, Faculty of Physics, Boltzmannngasse 5, A-1090 Vienna, Austria

Jack Holguin

CPHT, CNRS, Ecole polytechnique, IP Paris, F-91128 Palaiseau, France

Ian Moult

Department of Physics, Yale University, New Haven, CT 06511

Aditya Pathak

University of Manchester, School of Physics and Astronomy, Manchester, M13 9PL, United Kingdom

Abstract

Final states in collider experiments are characterized by correlation functions, $\langle \mathcal{E}(\vec{n}_1) \cdots \mathcal{E}(\vec{n}_k) \rangle$, of the energy flow operator $\mathcal{E}(\vec{n}_i)$. We show that the top quark imprints itself as a peak in the three-point correlator at an angle $\zeta \sim m_t^2/p_T^2$, with m_t the top quark mass and p_T its transverse momentum, thereby providing access to one of the most important parameters of the Standard Model in one of the simplest field theoretical observables. Our analysis represents the first step towards a novel precision top mass determination that is, for the first time, highly insensitive to soft physics and underlying event contamination whilst remaining directly calculable from the Standard Model Lagrangian.

1 Introduction

The top quark mass plays a central role both in determining the structure of the electroweak vacuum and in the consistency of precision Standard Model fits. A field theoretic definition of m_t , and its relation to experimental measurements, though, is notoriously subtle ^{1, 2}). At future e^+e^- colliders, high precision m_t measurements from the threshold lineshape will be possible. At present, the remarkably small quoted uncertainties on m_t from direct extractions at the LHC have been argued to be potentially affected by an additional $\mathcal{O}(1 \text{ GeV})$ contribution stemming from the theoretical interpretation of the measured “Monte Carlo (MC) top mass parameter” (for quantitative estimates, see e.g. refs. ^{4, 5, 6}). It is thus crucial and timely to explore kinematic top-mass sensitive observables at the LHC where a direct comparison of experimental data with accurate first principles theory predictions can be carried out.

Significant progress has been made in this regard from multiple directions. A unique feature of the LHC is that large numbers of top quarks are produced with enough boosts to decay into single collimated jets on which jet shapes can be measured. Using Soft Collinear Effective Theory and boosted

Heavy Quark Effective Theory, factorization theorems have been derived for event shapes measured on boosted top quarks, enabling these observables to be expressed in terms of m_t in a field theoretically well-defined mass scheme. In this framework, a paradigmatic example is given by the groomed jet mass. While jet grooming significantly improves the robustness of the observable on which it is applied, the complicated residual non-perturbative corrections³⁾ continue to be a limiting factor in achieving a precision competitive with direct measurements. This motivates the exploration of further m_t -sensitive observables that do not rely on jet grooming.

In recent years, intriguing progress has been made within a program aiming to rethink⁷⁾ jet substructure in terms of correlation functions, $\langle \mathcal{E}(\vec{n}_1) \cdots \mathcal{E}(\vec{n}_k) \rangle$, of the energy flow $\mathcal{E}(\vec{n})$ in a direction \vec{n} ^{8, 9, 10)}, motivated also by the original work in QCD¹¹⁾. These correlators have a number of unique and remarkable properties. Most importantly for phenomenological applications, correlators are mostly insensitive to soft radiation without the application of grooming. Additionally they can also be computed on tracks^{7, 12)}, using the formalism of track functions¹³⁾, allowing for higher angular resolution and pile-up suppression. However, so far these applications have been restricted to massless quark or gluon jets.

In¹⁴⁾ we have presented the first steps towards a new precision m_t measurement based on the simple idea of exploiting the mass dependence of the characteristic opening *angle* of the decay products of the boosted top, $\zeta \sim m_t^2/p_T^2$. The motivation for rephrasing the question in this manner is twofold. First, this angle can be accessed via low-point correlators, which are field theoretically drastically more simple than a groomed substructure observable sensitive to ζ . Second, while the jet mass is sensitive to soft contamination and UE, the angle ζ is not, since it is primarily determined by the hard dynamics of the top decay. In the following, we will illustrate a numerical proof-of-principles analysis showing that the three-point correlator in the vicinity of $\zeta \sim m_t^2/p_T^2$ provides a simple, but highly sensitive probe of m_t , free of the typical challenges of jet-shape based approaches. Our goal is to provide the motivation to perform future precision analyses and to find solutions to outstanding theoretical problems concerning low-point correlators relevant to the top mass determination and novel jet substructure studies.

2 The Three-Point Energy Correlator

There has recently been significant progress in understanding the perturbative structure of correlation functions of energy flow operators. This includes the landmark analytical calculation of the two-point correlator at next-to-leading order (NLO) in QCD¹⁵⁾ as well as the first calculation of a three-point correlator¹⁶⁾ at LO. The idea of using the three-point correlator to study the top quark is a natural one, and was considered early on in the jet substructure literature¹⁷⁾. However, recent theoretical progress enables us now to make concrete steps towards a comprehensive program of using energy correlators as a precision tool for Standard Model measurements^{7, 18)}.

The three-point correlator (EEEC) with generic energy weights is defined as

$$G^{(n)}(\zeta_{12}, \zeta_{23}, \zeta_{31}) = \int d\sigma \widehat{\mathcal{M}}^{(n)}(\zeta_{12}, \zeta_{23}, \zeta_{31}), \quad (1)$$

with the measurement operator given by

$$\widehat{\mathcal{M}}^{(n)}(\zeta_{12}, \zeta_{23}, \zeta_{31}) = \sum_{i,j,k} \frac{E_i^n E_j^n E_k^n}{Q^{3n}} \delta(\zeta_{12} - \hat{\zeta}_{ij}) \delta(\zeta_{23} - \hat{\zeta}_{ik}) \delta(\zeta_{31} - \hat{\zeta}_{jk}). \quad (2)$$

Here $\hat{\zeta}_{ij} = (1 - \cos(\theta_{ij}))/2$, with θ_{ij} the angle between particles i and j , the sum runs over all triplets

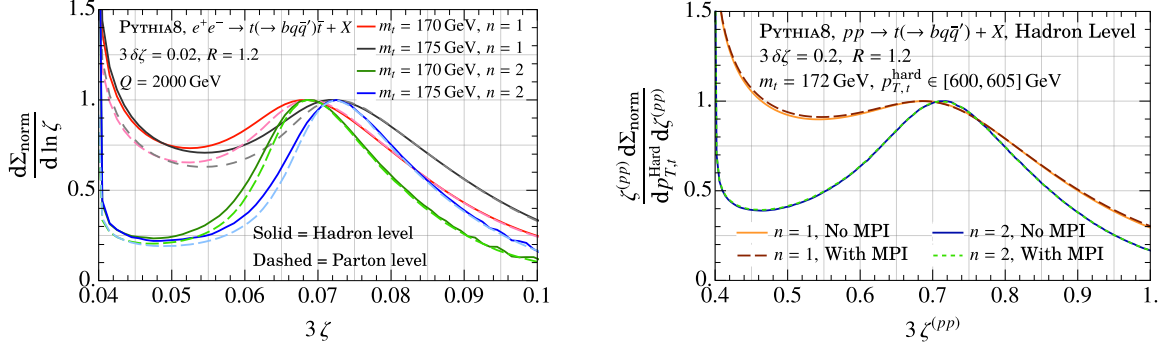


Figure 1: Weighted cross sections from three-point energy correlators using PYTHIA8. *Left panel:* The $n = 1, 2$ three-point correlators on boosted tops in e^+e^- annihilations showing a clear peak at $\zeta \sim 3m_t^2/Q^2$. All curves are normalized to peak height. *Right panel:* The $n = 1, 2$ three-point correlators on decaying top quarks with a fixed hard p_T in proton-proton collisions, with and without MPI. Here a clear peak can be seen at $\zeta \approx 3m_t^2/p_{T,t}^2$.

of particles in the jet, and Q denotes the hard scale in the measurement. It is worth stressing that the EEEC is not an event-by-event observable, but rather is defined as an ensemble average.

We are interested in the limit $\zeta_{12}, \zeta_{23}, \zeta_{31} \ll 1$, such that all directions of energy flow lie within a single jet. In the case of a conformal field theory (or massless QCD up to the running coupling), the small-angle limit of the EEEC simplifies due to the rescaling symmetry along the light-like direction defining the jet. In our case, m_t explicitly breaks this rescaling symmetry and appears as a characteristic scale imprinted in the three-point correlator. While the top quark has a three-body decay at leading order, higher-order corrections give rise to additional radiation, which is primarily collinear to the decay products leading to a growth in the distribution at angles $\hat{\zeta}_{ij} \ll m_t^2/p_T^2$. To extract m_t , we therefore focus on the correlator in a specific energy flow configuration sensitive to the hard decay kinematics. In ¹⁴⁾ the simplest configuration is studied, that of an equilateral triangle $\hat{\zeta}_{ij} = \zeta$ allowing for a small asymmetry ($\delta\zeta$). Thus the key object of our analysis is the n th energy weighted cross section

$$\frac{d\Sigma(\delta\zeta)}{dQd\zeta} = \int d\zeta_{12}d\zeta_{23}d\zeta_{31} \int d\sigma \widehat{\mathcal{M}}_{\Delta}^{(n)}(\zeta_{12}, \zeta_{23}, \zeta_{31}, \zeta, \delta\zeta), \quad (3)$$

where the measurement operator $\widehat{\mathcal{M}}_{\Delta}^{(n)}$ is

$$\widehat{\mathcal{M}}_{\Delta}^{(n)}(\zeta_{12}, \zeta_{23}, \zeta_{31}, \zeta, \delta\zeta) = \widehat{\mathcal{M}}^{(n)}(\zeta_{12}, \zeta_{23}, \zeta_{31}) \delta(3\zeta - \zeta_{12} - \zeta_{23} - \zeta_{31}) \prod_{l,m,n \in \{1,2,3\}} \Theta(\delta\zeta - |\zeta_{lm} - \zeta_{mn}|). \quad (4)$$

For $\delta\zeta \ll \zeta$,

$$\frac{d\Sigma}{d\zeta} \approx 4(\delta\zeta)^2 G^{(n)}(\zeta, \zeta, \zeta; m_t), \quad (5)$$

where we have made the dependence on m_t explicit. Three-body kinematics implies that the distribution is peaked at $\zeta_{\text{peak}} \approx 3m_t^2/Q^2$, exhibiting quadratic sensitivity to m_t . At the LHC the peak is resilient to collinear radiation since $\ln \zeta_{\text{peak}} < 1/\alpha_s$, making its properties computable in fixed-order perturbation theory at the hard scale. In the region $\zeta < 2\delta\zeta$ the hard three-body kinematics is no longer identified, leading to a bulge in the distribution, as shown in the *Supplemental Material* in ref. ¹⁴⁾.

3 Mass Sensitivity in e^+e^-

To illustrate the mass sensitivity of our observable, we begin with the simplest case of e^+e^- collisions. We simulate the $e^+e^- \rightarrow t + X$ process at a center of mass energy of $Q = 2000$ GeV using the PYTHIA8 parton shower and reconstruct anti- k_T jets with $R = 1.2$. Although jet clustering is not required in e^+e^- , this analysis strategy is chosen to achieve maximal similarity with the case of hadron colliders.

In the left panel of Fig. 1 we show the distribution of the three-point correlator in the peak region, both with and without the effects of hadronization. Agreement of the peak position with the leading-order expectation is found, showing that the observed behavior is dictated by the hard decay of the top. In Fig. 1, linear ($n = 1$) and quadratic ($n = 2$) energy weightings are used, see Eq. (2). The latter is not collinear safe, but the collinear IR-divergences can be absorbed into moments of the fragmentation functions or track functions.

Crucially, non-perturbative effects in energy correlators are governed by an additive underlying power law^[19, 9], which over the width of the peak has a minimal effect on the normalized distribution. This is confirmed by the small differences in peak position between parton and hadron level distributions in Fig. 1. Taking $m_t = 170, 172$ GeV with $n = 2$ as representative distributions, we find that the shift due to hadronization corresponds to a $\Delta m_t^{\text{Had.}} \sim 250$ MeV shift in m_t . This is in contrast with the groomed jet mass case where hadronization causes peak shifts equivalent to $\Delta m_t^{\text{Had.}} \sim 1$ GeV^[20].

4 Hadron Colliders

We now extend our discussion to the more challenging case of proton-proton collisions. This study illustrates the difference between energy correlators and standard jet shape observables, and also emphasizes the irreducible difficulties of jet substructure at hadron colliders.

At variance with the case of e^+e^- annihilations, the hadronic final states in proton-proton collisions on which the energy correlators are computed are necessarily defined through a measurement, e.g. by selecting anti- k_T jets with a specific $p_{T,\text{jet}}$. Due to the insensitivity of the energy correlators to soft radiation, it is in fact the non-perturbative effects on the jet p_T selection that are the only source of complications in a hadron collider environment^[14]. This represents a significant advantage of our approach, since it shifts the standard problem of characterizing non-perturbative corrections to infrared jet shape observables, to characterizing non-perturbative effects on a *hard* scale. This enables us to propose a methodology for the precise extraction of m_t in hadron collisions by independently measuring the universal non-perturbative effects on the $p_{T,\text{jet}}$ spectrum. We now illustrate the key features of this approach.

The three-point correlator in hadron collisions is defined as

$$\widehat{\mathcal{M}}_{(pp)}^{(n)}(\zeta_{12}, \zeta_{23}, \zeta_{31}) = \sum_{i,j,k \in \text{jet}} \frac{(p_{T,i})^n (p_{T,j})^n (p_{T,k})^n}{(p_{T,\text{jet}})^{3n}} \delta\left(\zeta_{12} - \hat{\zeta}_{ij}^{(pp)}\right) \delta\left(\zeta_{23} - \hat{\zeta}_{ik}^{(pp)}\right) \delta\left(\zeta_{31} - \hat{\zeta}_{jk}^{(pp)}\right), \quad (6)$$

where $\hat{\zeta}_{ij}^{(pp)} = \Delta R_{ij}^2 = \sqrt{\Delta\eta_{ij}^2 + \Delta\phi_{ij}^2}$, with η, ϕ the standard rapidity, azimuth coordinates.

The peak of the EEEC distribution is determined by the hard kinematics and is found at $\zeta_{\text{peak}}^{(pp)} \approx 3m_t^2/p_{T,t}^2$, where $p_{T,t}$ is the hard top p_T , *not* $p_{T,\text{jet}}$.

To clearly illustrate the distinction between the infrared measurement of the EEEC and the hard measurement of the $p_{T,\text{jet}}$ spectrum, we present a two-step analysis using data generated in PYTHIA8^[14]. First, we generated hard top quark states with definite momentum (like in e^+e^-), but in the more complicated LHC environment including the underlying event (UE). This is shown in the right panel of

Fig. 1, where we see a clear peak that is *completely* independent of the presence of MPI (the PYTHIA8 model for UE), which illustrates that the correlators themselves, on a perfectly characterized top quark state, are insensitive to soft radiation *without* grooming.

In ref. ¹⁴⁾ a proof-of-principles analysis was performed to illustrate that a characterization of non-perturbative corrections to the $p_{T,\text{jet}}$ spectrum allows us to extract m_t , with small uncertainties from non-perturbative physics. To extract a value of m_t , we write the peak position as

$$\zeta_{\text{peak}}^{(pp)} = \frac{3F_{\text{pert}}(m_t, p_{T,\text{jet}}, \alpha_s, R)}{(p_{T,\text{jet}} + \Delta_{\text{NP}}(R) + \Delta_{\text{MPI}}(R))^2}, \quad (7)$$

where F_{pert} incorporates the effects of perturbative radiation. At leading order, $F_{\text{pert}} = m_t^2$. Corrections from hadronization and MPI are encoded through the shifts $\Delta_{\text{NP}}(R)$ and $\Delta_{\text{MPI}}(R)$. Crucially, in the factorization limit that we consider, these are not a property of the EEEC observable, but can instead be extracted directly from the non-perturbative corrections to the jet p_T spectrum ²¹⁾. This is a unique feature of our approach.

The next step would be to calculate F_{pert} at NLO in perturbative QCD within a well-defined short-distance top mass scheme (such as the MSR ²²⁾) and use the result to extract m_t according to the procedure described below. However, since the computation of F_{pert} has not been performed yet, in order to illustrate the feasibility of our approach, we have used PYTHIA8 (including hadronization and MPI) to extract $\zeta_{\text{peak}}^{(pp)}$ as a function of $p_{T,\text{jet}}$, over an energy range within the expected reach of the high luminosity LHC. As a proxy for the perturbative calculation, we used parton-level simulations to extract F_{pert} . To the accuracy we are working, F_{pert} is independent of the jet p_T , and can just be viewed as an effective top mass $\sqrt{F_{\text{pert}}(m_t)}$. We also extract $\Delta_{\text{NP}}(R) + \Delta_{\text{MPI}}(R)$ independently from the $p_{T,\text{jet}}$ spectrum.

Using Eq. (7) we fit $\zeta_{\text{peak}}^{(pp)}$ as a function of $p_{T,\text{jet}}$ for an effective value of $F_{\text{pert}}(m_t)$. With a perfect characterization of the non-perturbative corrections to the EEEC observable, the value of $F_{\text{pert}}(m_t)$ extracted when hadronization and MPI are included should exactly match its extraction at parton level. This would lead to complete control over m_t . In Table 1 we show the extracted value of $F_{\text{pert}}(m_t)$ from our parton level fit, and from our hadron+MPI level fit for two values of the PYTHIA8 m_t . The errors quoted are the statistical errors on the parton shower analysis. The Hadron+MPI fit is quoted with two errors: the first originates from the statistical error on the EEEC measurement, the second stems from the statistical error on the determination of $\Delta_{\text{NP}}(R) + \Delta_{\text{MPI}}(R)$ from the $p_{T,\text{jet}}$ spectrum. A more detailed discussion of this procedure can be found in the *Supplemental Material* in ¹⁴⁾. Thus we find promising evidence that theoretical control of m_t , with conservative errors $\lesssim 1\text{GeV}$, is possible with an EEEC-based measurement. We stress that systematically improvable calculations of $F_{\text{pert}}(m_t)$ within our approach are made feasible by a factorization formula for the weighted cross section discussed in ref. ¹⁴⁾. Theory errors are contingent upon currently unavailable NLO computations, see the discussion in ¹⁴⁾. However, we expect observable-dependent NLO theory errors on m_t to be better than those in other inclusive measurements wherein in the dominant theory errors are from PDFs+ α_s ^{23, 24)} and which mostly affect the normalization of the observable. By contrast the EEEC is also inclusive but the extracted m_t is only sensitive to the observable's shape.

Our promising results motivate developing a deeper theoretical understanding of the three-point correlator of boosted tops in the hadron collider environment. Nevertheless, there remain many areas in which our methodology could be improved to achieve greater statistical power and bring it closer to experimental reality. These include the optimization of $\delta\zeta$, the binning of $p_{T,\text{jet}}$ and $\zeta^{(pp)}$, and including other shapes on the EEEC correlator. Regardless, our analysis does demonstrate the observable's potential for

PYTHIA8 m_t	Parton $\sqrt{F_{\text{pert}}}$	Hadron + MPI $\sqrt{F_{\text{pert}}}$
172 GeV	172.6 ± 0.3 GeV	$172.3 \pm 0.2 \pm 0.4$ GeV
173 GeV	173.5 ± 0.3 GeV	$173.6 \pm 0.2 \pm 0.4$ GeV
175 GeV	175.5 ± 0.4 GeV	$175.1 \pm 0.3 \pm 0.4$ GeV
173 – 172	0.9 ± 0.4 GeV	1.3 ± 0.6 GeV
175 – 172	2.9 ± 0.5 GeV	2.8 ± 0.6 GeV

Table 1: The effective parameter $F_{\text{pert}}(m_t)$ extracted at parton level, and hadron+MPI level. The consistency of the two simulations provides a measure of our uncertainty due to uncontrolled non-perturbative corrections. Statistical errors are shown.

a precision m_t extraction when measured on a sufficiently large sample of boosted tops. We are optimistic that such a sample will be accessible at the HL-LHC where it is forecast that $\sim 10^7$ boosted top events with $p_T > 500$ GeV will be measured²⁵). Our results support the possibility of achieving complete theoretical control over an observable with top mass sensitivity competitive with direct measurements whilst avoiding the ambiguities associated with the usage of MC event generators.

References

1. G. Corcella, *Front. in Phys.* **7**, 54 (2019).
2. A.H. Hoang, *Ann. Rev. Nucl. Part. Sci.* **70**, 225 (2020).
3. A.H. Hoang, S. Mantry, A. Pathak and I.W. Stewart, *JHEP* **12**, 002 (2019).
4. J. Kieseler, K. Lipka and S.-O. Moch, *Phys. Rev. Lett.* **116**, 162001 (2016).
5. M. Butenschoen, B. Denhadi, A.H. Hoang, V. Mateu, M. Preisser and I.W. Stewart, *Phys. Rev. Lett.* **117**, 232001 (2016).
6. A.H. Hoang, S. Plätzer and D. Samitz, *JHEP* **10**, 200 (2018).
7. H. Chen, I. Moulton, X.Y. Zhang and H.X. Zhu, *Phys. Rev. D* **5**, 054012 (2020).
8. N.A. Sveshnikov and F.V. Tkachov, *Phys. Lett. B* **382**, 403 (1996).
9. G.P. Korchemsky and G.F. Sterman, *Nucl. Phys. B* **555**, 335 (1999).
10. D. Hofman and J. Maldacena, *JHEP* **05**, 012 (2008).
11. C.L. Basham, L.S. Brown, S.D. Ellis and S.T. Love, *Phys. Rev. Lett.* **41**, 1585 (1978).
12. Y. Li, I. Moulton, S. Schrijnder van Velzen, W.J. Waalewijn and H.X. Zhu, *Phys. Rev. Lett.* **18**, 182001 (2022).
13. H.-M. Chang, M. Procura, J. Thaler and W.J. Waalewijn, *Phys. Rev. Lett.* **111**, 102002 (2013).
14. J. Holguin, I. Moulton, A. Pathak and M. Procura, arXiv:2201.08393 [hep-ph].
15. L.J. Dixon, M.-X. Luo, V. Shtabovenko, T.-Z. Yang and H.X. Zhu, *Phys. Rev. Lett.* **120**, 102001 (2018).
16. H. Chen, M.-X. Luo, I. Moulton, T.-Z. Yang, X. Zhang and H.X. Zhu, *JHEP* **08**, 028 (2020).

17. M. Jankowiak and A.J. Larkoski, JHEP **06**, 057 (2011).
18. P.T. Komiske, I. Moulton, J. Thaler and H.X. Zhu, arXiv:2201.07800 [hep-ph].
19. G.P. Korchemsky and G.F. Sterman, Nucl. Phys. B **437**, 415 (1995).
20. A.H. Hoang, S. Mantry, A. Pathak and I.W. Stewart, Phys. Rev. D **100**, 074021 (2019).
21. M. Dasgupta, L. Magnea and G.P. Salam, JHEP **02**, 055 (2008).
22. A.H. Hoang, A. Jain, I. Scimemi and I.W. Stewart, Phys. Rev. Lett **101**, 151602 (2008).
23. S. Chatrchyan et al., Phys. Lett. B **728**, 496 (2014).
24. A.M. Sirunyan et al., JHEP **09**, 051 (2017).
25. P. Azzi et al., CERN Yellow Rep. Monogr. **7**, 1 (2019).

NON-FACTORISABLE CORRECTIONS TO t -CHANNEL SINGLE-TOP PRODUCTION: COMPARING RESULTS FOR THE LHC AND FCC

Christian Brønnum-Hansen

*Institute for Theoretical Particle Physics, Karlsruhe Institute of Technology (KIT),
Wolfgang-Gaede-Strae 1, 76131 Karlsruhe, Germany*

J eremie Quarroz

*Institute for Theoretical Particle Physics, Karlsruhe Institute of Technology (KIT),
Wolfgang-Gaede-Strae 1, 76131 Karlsruhe, Germany*

Chiara Signorile-Signorile

*Institute for Theoretical Particle Physics, Karlsruhe Institute of Technology (KIT),
Wolfgang-Gaede-Strae 1, 76131 Karlsruhe, Germany,*

*Institute for Astroparticle Physics, Karlsruhe Institute of Technology (KIT),
Hermann-von-Helmholtz-Platz 1, 76344 Eggenstein-Leopoldshafen, Germany*

Chen-Yu Wang

*Institute for Theoretical Particle Physics, Karlsruhe Institute of Technology (KIT),
Wolfgang-Gaede-Strae 1, 76131 Karlsruhe, Germany*

Max-Planck-Institut fr Physik, Fhringer Ring 6, 80805 Mnchen, Germany

Abstract

In this contribution we report on the recent calculation of QCD non-factorisable corrections to t -channel single-top production and stress the importance of these corrections in the light of increasing the accuracy of theoretical predictions for this process. We present results for the total cross section and for selected observables relevant for proton-proton collisions at the LHC and the FCC.

TTP23-006, P3H-23-011

1 Introduction

The large mass and the strong coupling with the Higgs boson makes the top quark a favorite candidate to improve our understanding of the Standard Model, and possibly reveal heavy new physics. A large fraction of the top quarks produced at the LHC emerges from electroweak interactions, via the so-called t -channel single-top production. Predictions for this process can be used, for instance, to constrain the CKM matrix element V_{bt} , and probe possible anomalous couplings in the tWb vertex. QCD corrections to t -channel single-top production are known up to next-to-next-to-leading order (NNLO) in the factorisable approximation ^{1, 2, 3, 4}, namely neglecting the crosstalk between different quark lines (see the left panel of Fig.1 for an example of a Feynman diagram contributing to the factorisable corrections). Factorisable corrections are found to be considerably small and only impact the cross section at $\mathcal{O}(1\%)$. Given the current level of the theory precision, it is useful to go beyond this approximation, and compute the non-factorisable corrections (see the right panel of Fig.1 for an example of Feynman diagram). This contribution vanishes at NLO, due to colour conservation, and it is colour suppressed at NNLO by a factor $N_c^2 - 1 = 8$ with respect to the factorisable corrections. However, it has been recently argued

Table 1: Comparison of the poles of the two-loop amplitude with the ones predicted using Catani’s operator for $s \sim 104.337 \text{ GeV}^2$ and $t \sim -5179.68 \text{ GeV}^2$.

	ϵ^{-2}	ϵ^{-1}
$\langle \mathcal{A}^{(0)} \mathcal{A}_{\text{nf}}^{(2)} \rangle$	$-229.0940408654660 - 8.978163333241640i$	$-301.1802988944764 - 264.1773596529505i$
Catani	$-229.0940408654665 - 8.978163333241973i$	$-301.1802988944791 - 264.1773596529535i$

that an enhancement factor π^2 , due to the Glauber phase, may enhance non-factorisable corrections and compensate for the colour suppression. This effect was explicitly proven to occur in the calculation of non-factorisable corrections to the vector boson fusion in the eikonal approximation ⁵⁾.

In this document we summarise the results obtained for the non-factorisable corrections to t -channel single-top production ^{6, 7, 8)} and discuss their relevance for 13 TeV and 100 TeV proton-proton collisions.

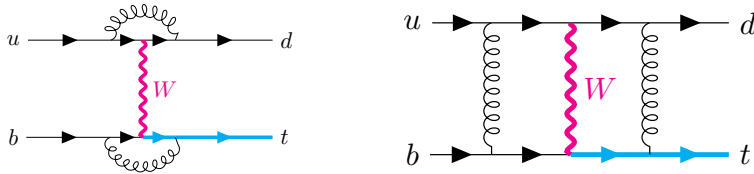


Figure 1: Left panel: example of Feynman diagram contributing to factorisable corrections. Right panel: example of diagram contributing to non-factorisable corrections. Massless quarks are indicated with thin black line, while the massive top-quark is depicted with a blue solid line.

2 Ingredients of the calculation

One crucial ingredient for the calculation is the double-virtual correction. In this regard, the most challenging part is the evaluation of the two-loop amplitude associated to non-factorisable diagrams as in the right panel of Fig. 1. The double-virtual amplitude is obtained numerically through the auxiliary mass flow method ^{10, 11)}. We refer the reader to Ref. ⁶⁾ for further details. Here we emphasise that the reduction of the amplitude is done analytically, retaining the full dependence on the kinematic scales s , t , m_W and m_t . The evaluation of the master integrals can be performed to any desired accuracy within a modest computing time (for a typical phase space point, 20 digits accuracy can be reached in about 30 minutes on a single core). In Tab. 2, we present the poles obtained for the two-loop amplitude compared to those predicted by Catani’s operator ⁹⁾. The match between the two values degrades by only one digit per ϵ -order, starting with an agreement of 15 digits at ϵ^{-2} . We then expect a 13 digits accuracy for the finite part. To evaluate the cross section, we prepare a grid optimised for the Born cross section. We extract 10 independent sets of 10^4 points from this grid and evaluate the amplitude for each of these points. The resulting accuracy can be estimated to be $\mathcal{O}(2\%)$.

A further non-trivial element of the calculation is the evaluation of real-virtual amplitudes, and of the corresponding cross-section level contribution. The challenge is related to the presence of numerous mass scales and to the necessity of having stable results also in kinematic regions where the extra radiation becomes unresolved. We note that working with anticommuting γ_5 in d dimensions, we can calculate

form factors treating the weak current as a pure vector current, while fixing the external massless quarks to be left-handed. To treat the form factors we manage to express the real-virtual amplitude in terms of scalar box, triangle and bubble integrals. To improve the numerical stability of the amplitude, we switch to a basis of finite box integrals, restricting the divergent part to triangle integrals only, whose coefficients either become independent of the dimensional regulator ϵ or simply vanish.

The last contribution is the tree-level, double-real correction, which involves the emission of two, potentially unresolved, gluons that connect the massive and the massless quark lines. Real emission contributions are known to develop soft and collinear (IR) singularities and therefore cannot be evaluated directly (see for instance Ref. ¹²⁾ for a recent review on the topic). In our analysis we exploit the nested soft-collinear subtraction scheme ¹³⁾ to handle this issue and obtain fully differential results. For the process at hand, only soft singularities can affect real-radiation amplitudes, and they are only related to independent emissions, namely to Abelian-like interactions. This observation simplifies remarkably the subtraction procedure, which indeed requires a limited number of counterterms. When integrating over the energies and emission angles of unresolved partons, the IR singularities encoded in the counterterms turn into poles in ϵ , which cancel against those stemming from virtual and real-virtual corrections. A small complication arises from having massive emitters. However, phase space integration can be performed analytically and returns compact results.

3 Phenomenology at the LHC and at the FCC

We consider proton-proton collisions at 13 TeV and at 100 TeV. We use the CT14 set for parton distribution functions (PDF) and the strong coupling constant. We match the perturbative order of the cross section to that of the PDF set, and use the following input parameters: $v = 246.2$ GeV, $m_W = 80.379$ GeV, and $m_t = 173.0$ GeV.

We first present the integrated cross section at a fixed factorisation scale $\mu_F = m_t$ at 13 TeV

$$\frac{\sigma_{pp \rightarrow X+t}}{1 \text{ pb}} = 117.96 + 0.26 \left(\frac{\alpha_s(\mu_R)}{0.108} \right)^2. \quad (1)$$

We stress that non-factorisable corrections arise for the first time at NNLO, and therefore there is not a clear indication of an optimal choice of renormalisation scale. From Eq.1, it is clear that changing the value of μ_R can substantially modify the impact of these corrections. For instance, considering the renormalisation scale $\mu_R = m_t$, the non-factorisable corrections amount to about 0.2% of the LO cross section. If instead we set μ_R to the typical transverse momentum of the top quark, $\mu_R = 40$ GeV, non-factorisable corrections reach 0.35% of the LO cross section. Although tiny, non-factorisable corrections are quite comparable to the NNLO factorisable corrections to the NLO cross section. The latter were computed to be about -0.7% for similar choices of scales and parton distribution functions (see Table 7 in Ref. ⁴⁾).¹ To further analyse the effects of different scale choices, in Tab. 3 we report the LO cross section and the corresponding non-factorisable corrections for different values of the minimal top-quark transverse momentum ($p_{\perp}^{t,cut}$). We fixed $\mu_F = m_t$ and vary the renormalisation scale. For $\mu_R = m_t$ we also include scale variations corresponding to $\mu_R/2$ and $2\mu_R$. We notice that, while the LO cross section decreases by $\mathcal{O}(11\%)$ if the p_{\perp}^t cut increases from 0 to 60 GeV, the non-factorisable contribution to the cross section increases by $\mathcal{O}(8\%)$, both for $\mu_R = m_t$ and $\mu_R = 40$ GeV.

¹Computations in Ref. ⁴⁾ were performed for proton-proton collisions at 14 TeV.

Table 2: *Dependence of the LO cross section and the non-factorisable corrections on the transverse momentum of the top quark for different values of the renormalisation scale, at $\mu_F = m_t$. For each scale choice, we report the relative impact, δ_{NNLO} , of the non-factorisable contributions with respect to the LO cross section. See Ref. ⁷⁾ and the text for further details.*

$p_{\perp}^{t,cut}$	σ_{LO} (pb)	$\mu_R = m_t$		$\mu_R = 40 \text{ GeV}$	
		$\sigma_{\text{NNLO}}^{\text{nf}}$ (pb)	δ_{NNLO} [%]	$\sigma_{\text{NNLO}}^{\text{nf}}$ (pb)	δ_{NNLO} [%]
0 GeV	118.01	$0.26_{+0.06}^{-0.04}$	$0.22_{+0.05}^{-0.04}$	0.40	0.34
20 GeV	115.09	$0.26_{+0.06}^{-0.04}$	$0.23_{+0.05}^{-0.04}$	0.41	0.36
40 GeV	109.56	$0.27_{+0.06}^{-0.05}$	$0.25_{+0.06}^{-0.04}$	0.43	0.39
60 GeV	104.63	$0.28_{+0.06}^{-0.05}$	$0.26_{+0.06}^{-0.04}$	0.43	0.41

Table 3: *Dependence of the LO cross section and the non-factorisable corrections on the transverse momentum of the top quark for different values of the renormalisation scale, at $\mu_F = m_t$ and $\sqrt{S} = 100 \text{ TeV}$. Similarly to Tab. 3, for each scale choice we report the relative impact, δ_{NNLO} , of the non-factorisable contributions with respect to the LO cross section. See Ref. ⁸⁾ and the text for further details.*

$p_{\perp}^{t,cut}$	σ_{LO} (pb)	$\mu_R = m_t$		$\mu_R = 40 \text{ GeV}$	
		$\sigma_{\text{NNLO}}^{\text{nf}}$ (pb)	δ_{NNLO} [%]	$\sigma_{\text{NNLO}}^{\text{nf}}$ (pb)	δ_{NNLO} [%]
0 GeV	2367.02	$3.79_{+0.84}^{-0.63}$	$0.16_{+0.04}^{-0.03}$	5.95	0.25
20 GeV	2317.03	$3.89_{+0.86}^{-0.64}$	$0.17_{+0.04}^{-0.03}$	6.11	0.26
40 GeV	2216.61	$4.14_{+0.92}^{-0.69}$	$0.19_{+0.04}^{-0.03}$	6.50	0.29
60 GeV	2121.88	$4.28_{+0.95}^{-0.71}$	$0.20_{+0.04}^{-0.03}$	6.71	0.32

We now present the results for the integrated cross-section at 100 TeV

$$\frac{\sigma_{pp \rightarrow X+t}}{1 \text{ pb}} = 2367.0 + 3.8 \left(\frac{\alpha_s(\mu_R)}{0.108} \right)^2. \quad (2)$$

For a renormalisation scale $\mu_R = m_t$, the NNLO corrections amount to 0.16%, and increase to 0.25% for $\mu_R = 40 \text{ GeV}$. In order to compare the two energy regimes, 13 and 100 TeV, we repeat the analysis presented in the previous paragraph and report in Tab. 3 the impact of imposing different cuts on the top-quark transverse momentum and varying the renormalisation scale. We notice that, for a center-of-mass energy of 100 TeV, the LO cross-section manifests a relative decrease of $\mathcal{O}(10\%)$ when setting $p_{\perp}^{t,cut} = 60 \text{ GeV}$. This behaviour is comparable with the one observed at 13 TeV. On the other hand, non-factorisable corrections increase by a slightly larger amount with respect to the 13 TeV result: $\mathcal{O}(13\%)$ for both $\mu_R = m_t$ and $\mu_R = 40 \text{ GeV}$.

We then consider differential distributions, and study the the impact of the non-factorisable corrections on the top-quark transverse momentum. In Fig. 2 we plot with a blue solid line the LO contribution, with a red dashed line the non-factorisable corrections at $\mu \equiv \mu_F = \mu_R = m_t$ (the corresponding scale variation is denoted by the striped region), and with a green dashed line the non-factorisable corrections at $\mu = 40 \text{ GeV}$. We notice from Fig. 2 that for both $\sqrt{S} = 13 \text{ TeV}$ and $\sqrt{S} = 100 \text{ TeV}$, the non-factorisable corrections are p_{\perp}^t -dependent and manifest a similar shape. For instance, they are relatively small and negative at low values of the transverse momentum. This behaviour is compatible with the one of the

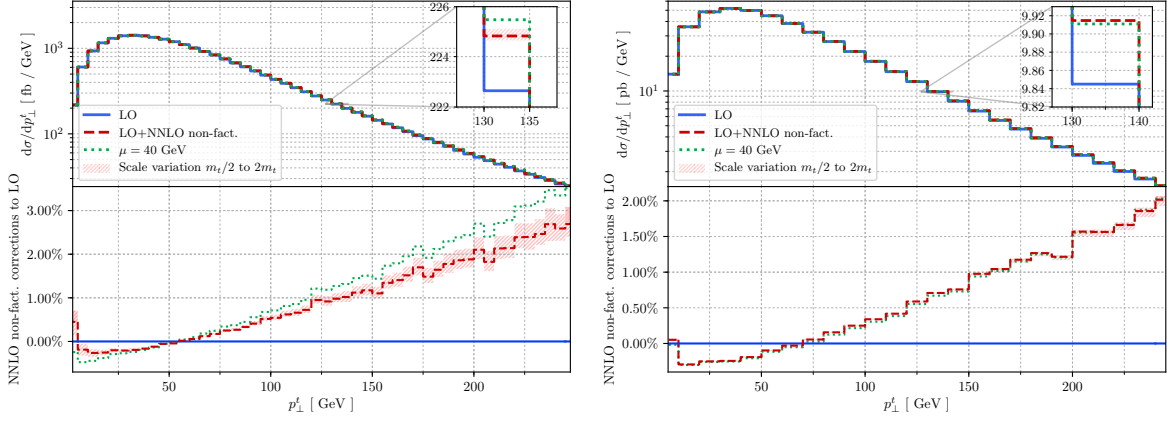


Figure 2: *Top quark transverse momentum distribution for $\sqrt{S} = 13$ TeV (left panel) and $\sqrt{S} = 100$ TeV (right panel). The blue solid line represents the Born cross section. The red dashed line corresponds to the non-factorisable corrections at $\mu \equiv \mu_F = \mu_R = m_t$. The striped region denotes the scale variation band. We also present with a green dotted line the p_{\perp}^t distribution at $\mu = 40$ GeV.*

double-virtual correction, presented in Ref. 6), which we expect to be kinematically favoured at low p_{\perp}^t . In contrast, we observe that the sign of the corrections changes at different values of p_{\perp}^t depending on \sqrt{S} : around 70 GeV for $\sqrt{S} = 100$ TeV and around 50 GeV for $\sqrt{S} = 13$ TeV.

We turn to the analysis of jet observables and focus on the transverse momentum distribution of the leading jet. To define jets we use the k_{\perp} -algorithm 14) and require them to have transverse momenta larger than 30 GeV and a radius of $R = 0.4$. From Fig. 3 we observe that the corrections to the leading-jet

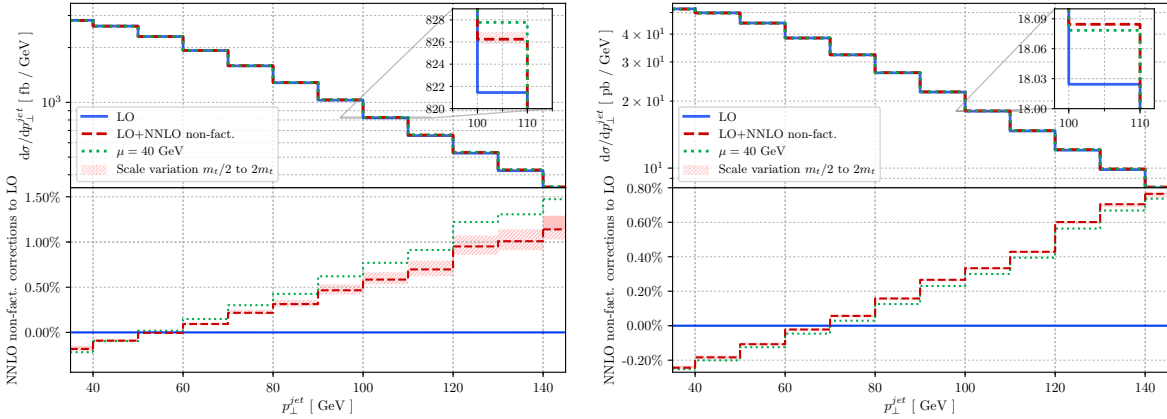


Figure 3: *Leading jet transverse momentum distribution for $\sqrt{S} = 13$ TeV (left panel) and $\sqrt{S} = 100$ TeV (right panel). See the caption of Fig. 2 for details about the colors code.*

transverse momentum are negative for p_{\perp}^{jet} smaller than ~ 50 GeV and reach about 1% at $p_{\perp}^{jet} \sim 140$ GeV for $\sqrt{S} = 13$ TeV. In contrast, at $\sqrt{S} = 100$ TeV the corrections change sign around 70 GeV and reach 0.7% at $p_{\perp}^{jet} \sim 140$ GeV.

4 Conclusions

In this manuscript, we have reported on the recent calculation of *non-factorisable* corrections to the t -channel single-top production. This contribution was previously neglected by invoking its color suppression with respect to factorisable corrections, known since many years. The present calculation completes the estimate of NNLO corrections to the t -channel single-top production, and proves that the methods used to overcome the technical challenges are sufficiently robust to produce phenomenologically relevant results. We have investigated the impact of non-factorisable corrections on the inclusive cross section and on a number of kinematic distributions, for proton-proton collisions at 13 and 100 TeV. For collisions at 13 TeV, we have shown that non-factorisable contributions can become quite comparable to the factorisable ones in selected regions of the phase space. At 100 TeV, a direct comparison is not yet available due to the lack of results for the factorisable component. Such comparison would be beneficial for a deeper understanding of the relative importance of the two classes of corrections, encouraging similar analysis for different processes.

5 Acknowledgements

The authors thank Prof. Kirill Melnikov for contributing to the results quoted in this report. This research is partially supported by the Deutsche Forschungsgemeinschaft (DFG, German Research Foundation) under grant 396021762 - TTR 257. CBH acknowledges support from the Carlsberg Foundation.

References

1. M. Brucherseifer *et al*, Phys. Lett. B **736**, 58 (2014).
2. E. L. Berger *et al*, Phys. Rev. D **94**, 7 (2016).
3. E. L. Berger *et al*, JHEP **11**, 158 (2017).
4. J. Campbell *et al*, JHEP **02**, 040 (2021).
5. T. Liu *et al*, Phys. Rev. Lett. **123**, 12 (2019).
6. C. Brønnum-Hansen *et al*, JHEP **11**, 130 (2021).
7. C. Brønnum-Hansen *et al*, JHEP **06**, 061 (2022).
8. C. Brønnum-Hansen *et al*, PoS LL2022, 035 (2022).
9. S. Catani, Phys. Lett. B **427**, 161 (1998).
10. X. Liu *et al*, Phys. Lett. B **779**, 353 (2018).
11. X. Liu *et al*, Chin. Phys. C **45**, 1 (2021)
12. N. Agarwal *et al*, Phys. Rept. **994**, 1 (2023).
13. F. Caola *et al*, Eur. Phys. J. C **77**, 248 (2017)
14. S. D. Ellis *et al*, Phys. Rev. D **48**, 3160 (1993)

Top pair entanglement in the SMEFT

Rafael Aoude

*Centre for Cosmology, Particle Physics and Phenomenology (CP3),
Université Catholique de Louvain, 1348 Louvain-la-Neuve, Belgium*

Abstract

Entanglement is a very powerful tool to explore properties of quantum states and their evolution. In this work, the spin entanglement in top pair production is explored within the framework of the Standard Model Effective Field Theory (SMEFT). In particular, we explore two regions of the phase space where the Standard Model produces maximally entangled states: the high-energy limit and at production threshold. We study the pattern in the $q\bar{q}$, gg and the pp initiated channels. In general, we have observed that higher-dimensional operators lower the entanglement produced purely by the Standard Model.

1 Introduction

In a recent work ¹⁾, the authors have explored the spin-entanglement of a top pair produced by Standard Model (SM) interactions at the Large Hadron Collider (LHC). Top quarks have two main advantages compared to other particles: they decay faster than their hadronization scale and therefore their spin information is directly transmitted to the decay products and they can be characterized by a simple bipartite qubit system. Since this work, many other studies have appear on top spin-entanglement ^{10, 11, 12, 13)} but also on other SM process such as photon pairs, $\tau\tau$, and diboson ^{12, 14, 15, 16, 17, 18)}

The authors also proposed an experimental strategy to detect entanglement based on measuring the differential cross-section with respect to the decay products' angle, in particular the angular separation of the charged leptons of each top. Furthermore, they have shown that there are two regions in the phase-space of *maximal entanglement*: for very high-energies $\hat{s} \rightarrow \infty$ and $\theta = \pi/2$ and at threshold $\hat{s} = 2m_t$. In these regions, the quantum state of the top pair is a triplet and singlet, respectively.

In this study ²⁾, with the final goal of studying the underlying theory of the SM, we use the SMEFT framework to explore two main questions:

- Are the Standard Model maximally-entangled regions affected by the SMEFT?
- Can the SMEFT induce new different maximally-entangled regions in the phase-space?

2 Top pair spin correlations

The study of the entanglement in spin-space is given in terms of the spin correlation matrix, also called the R -matrix

$$R_{\eta_1\eta_2,\zeta_1\zeta_2}^I = \frac{1}{N_a N_b} \sum_{\substack{\text{colors} \\ \text{spins}}} \mathcal{M}_{\eta_2\zeta_2}^* \mathcal{M}_{\eta_1\zeta_1} \quad \text{with} \quad \mathcal{M}_{\eta\zeta} \equiv \langle t(k_1, \eta) \bar{t}(k_2, \zeta) | \mathcal{T} | a(p_1) b(p_2) \rangle \quad (1)$$

where \mathcal{T} is the transition matrix and $I = ab$ denotes the possible initial state, i.e $I = q\bar{q}, gg$ at leading-order and $N_{a,b}$ represents the number of degrees of freedom in the initial states a and b . This matrix can be rewritten using the Fano decomposition³⁾

$$R = \tilde{A} \mathbb{1}_2 \otimes \mathbb{1}_2 + \tilde{B}_i^+ \sigma^i \otimes \mathbb{1}_2 + \tilde{B}_i^- \mathbb{1}_2 \otimes \sigma^i + \tilde{C}_{ij} \sigma^i \otimes \sigma^j, \quad (2)$$

where the summations over repeated indices are implicit and the first coefficient \tilde{A} is related to the cross-section. This matrix has to be properly normalized by taking $\rho = R/\text{tr}(R)$, which can be decomposed using the same Fano decomposition, in terms of Pauli matrices. The normalized coefficients are given by $B_i^\pm = \tilde{B}_i^\pm/\tilde{A}$ and $C_{ij} = \tilde{C}_{ij}/\tilde{A}$.

The R^I matrix for a given state is not representative of the initial state at the LHC in proton-proton collisions, where at leading-order, the gg - and $q\bar{q}$ -initiated channels contribute non-interfering. Hence, the initial quantum state is mixed and it is given by the weighted sum of both channels: $R(\hat{s}, \mathbf{k}) = \sum_I L^I(\hat{s}) R^I(\hat{s}, \mathbf{k})$, where $L^I(\hat{s})$ are the luminosity functions for each channel given in⁴⁾.

Once each matrix is obtained, we further calculate these coefficients in the so-called *helicity basis*, which consists of a centre-of-mass orthonormal frame:

$$\{\mathbf{k}, \mathbf{n}, \mathbf{r}\} : \quad \mathbf{r} = \frac{\mathbf{p} - z\mathbf{k}}{\sqrt{1 - z^2}}, \quad \mathbf{n} = \mathbf{k} \times \mathbf{r} \quad (3)$$

where \mathbf{p} and \mathbf{k} are unit vectors along the beam axis and the top direction with $z \equiv \mathbf{k} \cdot \mathbf{p}$. In this basis, the entanglement measure becomes very simple, as we are going to see in the following. But before, note that the spin density matrix, at LO in QCD, simplifies due to: invariance under CP, which implies symmetric C_{ij} and $B_i^+ = B_i^-$; non-zero C_{kn}, C_{rn} and B_n^\pm are only non-vanishing at one-loop; and, finally, $B_k^\pm = B_r^\pm = 0$, since interactions are P-even. For SMEFT, the two first statements still holds since we focus on CP even operators.

3 Entanglement in the SM(EFT)

For the most general bipartite quantum state acting on the Hilbert space $\mathcal{H}_{ab} = \mathcal{H}_a \otimes \mathcal{H}_b$, if the state can be written as a convex combination of product states $p_{ab} = \sum_k p_k \rho_a^k \otimes \rho_b^k$, the state is separable. If the state cannot be taken to this form, we say the state is entangled. However, it is more practical to use entanglement measures to quantify it. We have used the concurrence⁵⁾ and the Peres-Horodecki Criterion (PHC)^{6, 7)}. For the LO-QCD density matrix in the helicity basis, the PHC implies

$$\Delta[\rho] \equiv -C_{nn} + |C_{kk} + C_{rr}| - 1 > 0 \quad (4)$$

as a sufficient condition for entanglement. For the SM, at LO-QCD, the condition $\Delta > 0$ is a necessary condition and the concurrence can be written in a simple form as $C[\rho] = \max(\Delta/2, 0)$. For higher orders in SMEFT, the explicit analytical results can be found in App. C of²⁾.

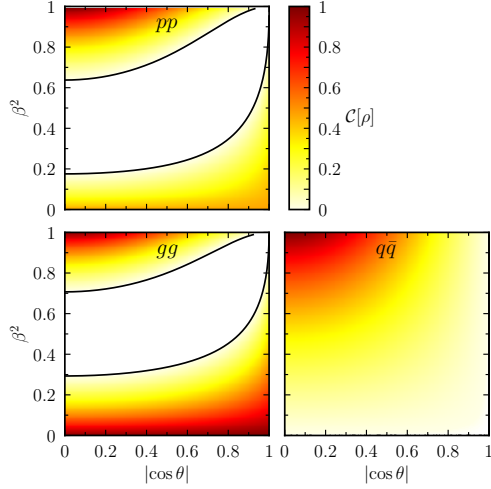


Figure 1: SM contribution for the concurrence in the $q\bar{q}$ - (bottom right) and gg -initiated (bottom left) channels, as well as in the full pp collision (top).

raised in the introduction for Fig. 1 and the maximally entangled quantum states. The SMEFT Lagrangian is formulated as

$$\mathcal{L}_{\text{SMEFT}} = \mathcal{L}_{\text{SM}} + \frac{1}{\Lambda^2} \sum_i c_i \mathcal{O}_i + \dots \quad (7)$$

where we work only with CP -even operators at dimension six. The relevant operators for our analysis are ⁸⁾

$$\mathcal{O}_G = g_s f^{ABC} G_\nu^{A,\mu} G_\rho^{B,\nu} G_\mu^{C,\rho}, \quad \mathcal{O}_{\varphi G} = \left(\varphi^\dagger \varphi - \frac{v^2}{2} \right) G_A^{\mu\nu} G_{\mu\nu}^A, \quad \mathcal{O}_{tG} = g_s (\bar{Q} \sigma^{\mu\nu} T^A t) \tilde{\varphi} G_{\mu\nu}^A + \text{h.c.}, \quad (8)$$

where φ is the Higgs doublet, as well as the color-octet and -singlet four-fermion operators

$$\mathcal{O}_{Qq}^{(8,1)} = (\bar{Q}_L \gamma_\mu T^a Q_L) (\bar{q}_L \gamma^\mu T^a q_L), \quad \mathcal{O}_{Qq}^{(8,3)} = (\bar{Q}_L \gamma_\mu T^a \sigma^A Q_L) (\bar{q}_L \gamma^\mu T^a \sigma^A q_L), \quad (9)$$

$$\mathcal{O}_{tu}^{(8)} = (\bar{t}_R \gamma_\mu T^a t_R) (\bar{u}_R \gamma^\mu T^a u_R), \quad \mathcal{O}_{td}^{(8)} = (\bar{t}_R \gamma_\mu T^a t_R) (\bar{d}_R \gamma^\mu T^a d_R), \quad (10)$$

$$\mathcal{O}_{Qu}^{(8)} = (\bar{Q}_L \gamma_\mu T^a Q_L) (\bar{u}_R \gamma^\mu T^a u_R), \quad \mathcal{O}_{Qd}^{(8)} = (\bar{Q}_L \gamma_\mu T^a Q_L) (\bar{d}_R \gamma^\mu T^a d_R), \quad (11)$$

$$\mathcal{O}_{tq}^{(8)} = (\bar{t}_R \gamma_\mu T^a t_R) (\bar{q}_L \gamma^\mu T^a q_L), \quad (12)$$

with the corresponding singlet operators given by the same expressions but without the $SU(3)$ generators T^a . Here, Q_L and q_L denote heavy and light left-handed quark doublets, respectively, and u_R and d_R are the right-handed light quarks.

To understand its effect, we come back to the R -matrix, expanding the SM and the EFT part and normalizing it as

$$\rho = \frac{R^{\text{SM}} + R^{\text{EFT}}}{\text{tr}(R^{\text{SM}}) + \text{tr}(R^{\text{EFT}})} \quad (13)$$

As stated before, the new density matrix can be written in terms of the Fano decomposition and all the explicit SMEFT contribution to these terms can be found in the Appendix A of the original paper ²⁾.

We first start with the SM, in particular the LO-QCD. For this case, we have reproduced the results from ¹⁾, which gives the plots in Fig. 1. For the gg -channel, we have two regions of maximal entanglement, at threshold $\beta = 0$, regardless of $z = \cos \theta$, and at high-energy ($\beta = 1$) and $\cos \theta = 0$. These produced quantum states are Bell states, where the former is given by a singlet and the latter by a triplet:

$$\rho_{gg}^{\text{SM}}(0, z) = |\Psi^-\rangle_{\mathbf{n}} \langle \Psi^-|_{\mathbf{n}}, \quad \rho_{gg}^{\text{SM}}(1, 0) = |\Psi^+\rangle_{\mathbf{n}} \langle \Psi^+|_{\mathbf{n}}, \quad (5)$$

while for the $q\bar{q}$ -channel we only have one maximally entangled state at high energies

$$\rho_{q\bar{q}}^{\text{SM}}(1, 0) = |\Psi^+\rangle_{\mathbf{n}} \langle \Psi^+|_{\mathbf{n}}, \quad (6)$$

and it is entangled across all the phase-space expected at threshold, which is separable. Given these conclusions for the SM, we would like to answer the questions

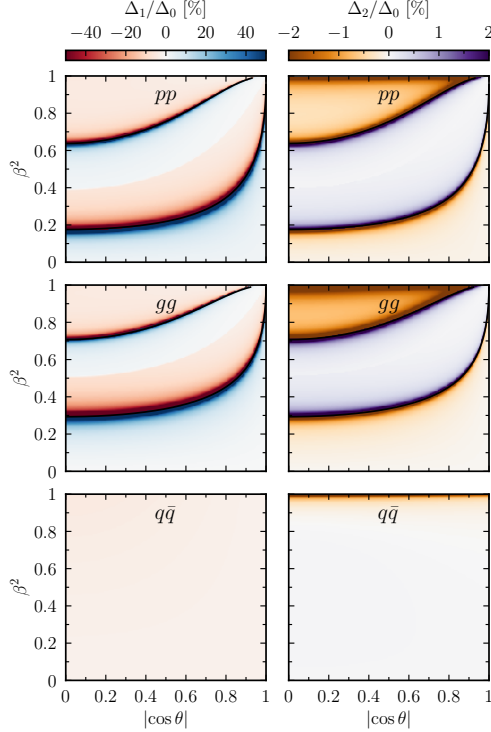


Figure 2: Relative contributions of the linear (left) and quadratic (right) effects of the chromomagnetic operator for $c_{tG}/\Lambda^2 = 0.1 \text{ TeV}^{-2}$ to the PHC entanglement marker Δ .

(both linear and quadratic) whereas at high energies, both effects may modify the level of entanglement around the SM point of maximal entanglement. In this region, the quadratic contribution of the latter always decreases the concurrence at high p_T and the linear one depends on the sign of the respective Wilson coefficient. The threshold quantum states are then modified to

$$\rho_{gg}^{\text{EFT}}(0, z) = p_{gg} |\Psi^+\rangle_{\mathbf{p}} \langle \Psi^+|_{\mathbf{p}} + (1 - p_{gg}) |\Psi^-\rangle_{\mathbf{p}} \langle \Psi^-|_{\mathbf{p}}, \quad (14)$$

$$\rho_{q\bar{q}}^{\text{EFT}}(0, z) = p_{q\bar{q}} |\uparrow\uparrow\rangle_{\mathbf{p}} \langle \uparrow\uparrow|_{\mathbf{p}} + (1 - p_{q\bar{q}}) |\downarrow\downarrow\rangle_{\mathbf{p}} \langle \downarrow\downarrow|_{\mathbf{p}} \quad (15)$$

where $p_{gg} = 72m_t^2(3\sqrt{2}m_t c_G + v c_{tG})^2 / 7\Lambda^4$ and $p_{q\bar{q}} = \frac{1}{2} - 4c_{VA}^{(8),u} / \Lambda^2 + \mathcal{O}(1/\Lambda^4)$. For the gg -initiated, SMEFT induces a triple state at quadratic order while for $q\bar{q}$ the eigenvalues of the matrix are affected. For the high- p_T region, the analysis is more subtle since we cannot reach $\beta \rightarrow 1$, where the EFT validity breaks down. However, for high enough energies and below the cut-off scale, the quadratic contribution again decreases the entanglement while the linear one depends on the Wilson coefficient sign.

4 Conclusion

In this work, we have explored the possibility of quantum observables, such as entanglement, to assess the impact of new physics effects in high-energy interactions. Two main entanglement measures were used, PHC and concurrence, to explore how the linear and quadratic SMEFT effects change the SM maximal entanglement. Overall, we have observed that linear higher-dimensional effects tend to vanish

Since the R -matrix includes a product of two scattering amplitudes expanded in Λ^{-2} , we will consider two types of terms: linear $\mathcal{O}(\Lambda^{-2})$ and quadratic $\mathcal{O}(\Lambda^{-4})$. To examine these contributions, we will consider the entanglement marker Δ at the desired order compared to the SM marker Δ_0 . Hence, for the linear order we define $\Delta_1 \equiv \Delta - \Delta_0$ where Δ is calculated with the ρ up to linear order. Similarly, we define $\Delta_2 \equiv \Delta - (\Delta_0 + \Delta_1)$ where ρ now also includes the squared contributions.

In Figure 2, we show an example plot for these markers. In particular, we show Δ_1/Δ_0 and Δ_2/Δ_0 for the operator \mathcal{O}_{tG} with the value of the Wilson coefficient given by $c_{tG} = 0.1 \text{ TeV}^{-2}$. In general, for the gg -channel, three operators contribute \mathcal{O}_{tG} , \mathcal{O}_G and $\mathcal{O}_{\varphi G}$. At threshold, all the linear interference effects vanish and the SMEFT does not affect the maximally entangled points induced by the SM, which is not generally true across the phase-space. At quadratic order, the story is different and although the operator $\mathcal{O}_{\varphi G}$ has a vanishing contribution, \mathcal{O}_G and \mathcal{O}_{tG} induce an entanglement decrease across the phase space and especially at the SM maximal points. For the latter, this can be seen in Figure 2 by the orange regions. In the $q\bar{q}$ initiated channel we have a similar pattern in the sense that there are no contributions to the marker Δ at threshold

in the threshold maximal entanglement point whereas quadratic terms lower the entanglement predicted in the Standard Model across the phase space.

Our study opens a number of questions worth being investigated such as higher-order in the EFT and loop expansion as well as other decay channels. The top pair production in SMEFT next-to-leading order in QCD accuracy was explored in ⁹⁾, where the inclusion of higher-orders do not dramatically change the LO results but give notable numerical differences.

5 Acknowledgements

The author thanks the organizers of the "LFC22: Strong Interaction from QCD to new dynamics at LHC and Future Colliders" for the great workshop in Trento. RA's research was funded by the F.R.S-FNRS project no. 40005600.

References

1. Y. Afik and J. R. M. de Nova, Eur. Phys. J. Plus **136** (2021) no.9, 907 doi:10.1140/epjp/s13360-021-01902-1 [arXiv:2003.02280 [quant-ph]].
2. R. Aoude, E. Madge, F. Maltoni and L. Mantani, Phys. Rev. D **106** (2022) no.5, 055007 doi:10.1103/PhysRevD.106.055007 [arXiv:2203.05619 [hep-ph]].
3. U. Fano, Rev. Mod. Phys. **55** (1983), 855-874 doi:10.1103/RevModPhys.55.855
4. W. Bernreuther, M. Flesch and P. Haberl, Phys. Rev. D **58** (1998), 114031 doi:10.1103/PhysRevD.58.114031 [arXiv:hep-ph/9709284 [hep-ph]].
5. W. K. Wootters, Phys. Rev. Lett. **80** (1998), 2245-2248 doi:10.1103/PhysRevLett.80.2245 [arXiv:quant-ph/9709029 [quant-ph]].
6. A. Peres, Phys. Rev. Lett. **77** (1996), 1413-1415 doi:10.1103/PhysRevLett.77.1413 [arXiv:quant-ph/9604005 [quant-ph]].
7. P. Horodecki, Phys. Lett. A **232** (1997), 333 doi:10.1016/S0375-9601(97)00416-7 [arXiv:quant-ph/9703004 [quant-ph]].
8. C. Degrande, G. Durieux, F. Maltoni, K. Mimasu, E. Vryonidou and C. Zhang, Phys. Rev. D **103** (2021) no.9, 096024 doi:10.1103/PhysRevD.103.096024 [arXiv:2008.11743 [hep-ph]].
9. C. Severi and E. Vryonidou, JHEP **01** (2023), 148 doi:10.1007/JHEP01(2023)148 [arXiv:2210.09330 [hep-ph]].
10. Y. Afik and J. R. M. de Nova, Quantum **6** (2022), 820 doi:10.22331/q-2022-09-29-820 [arXiv:2203.05582 [quant-ph]].
11. J. A. Aguilar-Saavedra and J. A. Casas, Eur. Phys. J. C **82** (2022) no.8, 666 doi:10.1140/epjc/s10052-022-10630-4 [arXiv:2205.00542 [hep-ph]].
12. M. Fabbrichesi, R. Floreanini and E. Gabrielli, [arXiv:2208.11723 [hep-ph]].
13. Y. Afik and J. R. M. de Nova, [arXiv:2209.03969 [quant-ph]].

14. J. A. Aguilar-Saavedra, A. Bernal, J. A. Casas and J. M. Moreno, Phys. Rev. D **107** (2023) no.1, 016012 doi:10.1103/PhysRevD.107.016012 [arXiv:2209.13441 [hep-ph]].
15. R. Ashby-Pickering, A. J. Barr and A. Wierchucka, [arXiv:2209.13990 [quant-ph]].
16. J. A. Aguilar-Saavedra, [arXiv:2209.14033 [hep-ph]].
17. M. M. Altakach, P. Lamba, F. Maltoni, K. Mawatari and K. Sakurai, [arXiv:2211.10513 [hep-ph]].
18. M. Fabbrichesi, R. Floreanini, E. Gabrielli and L. Marzola, [arXiv:2302.00683 [hep-ph]].

RESUMMATION OF LARGE ELECTROWEAK TERMS FOR INDIRECT DARK MATTER DETECTION

Martin Vollmann

Institut für Theoretische Physik, Eberhard Karls Universität Tübingen

Abstract

This paper reports on theoretical advances relevant for the indirect detection of TeV-scale Weakly Interacting Massive Particles (WIMPs) as dark matter. Our focus is on the resummation of large electroweak corrections in the endpoint spectrum of gamma rays from WIMP annihilations in the Milky Way, using non-relativistic soft collinear effective field theories. Our results are evaluated in the context of the “wino” and “higgsino” models, achieving next-to-leading-prime accuracy. We also introduce `DM γ Spec`, a tool that generates theoretical indirect detection templates for these models, making them readily available for use in gamma-ray telescope analyses.

1 Introduction

Our Universe consists mostly of dark matter - five times more than baryonic matter (stars, etc.)¹). Despite its abundance, the true nature of dark matter remains unknown. Uncovering its identity is thus a priority area of research in theoretical physics.

The WIMP scenario is an attractive framework that links, rather naturally, the dark matter (DM) problem to the need to extend the Standard Model (SM) of particle physics. WIMPs, which stands for weakly interacting massive particles, decoupled from the primordial plasma at a certain time after being in thermal equilibrium with it. In this hypothesis the observed amount of DM in the Universe depends on the rate of annihilation of these particles, which typically have the same strength as the electroweak interactions. For recent reviews refer to e. g. ^{2, 3}).

The theory space for these wimps is admitley very large, but some predictive scenarios exist. For example, if the DM field is part of an electroweak (EW) multiplet that is electrically neutral after the EW symmetry is broken, large masses of $\mathcal{O}(\text{TeV})$ are predicted in this setup^{4, 5}). In particular, the

minimal supersymmetric standard model (MSSM) contains fermionic (spin-1/2) EW multiplets that can mix, resulting in the Lightest Supersymmetric (Neutralino) particle (LSP) being a good WIMP DM candidate ⁶). Generic neutralinos consist of one Majorana EW triplet (wino), one Dirac doublet (higgsino), and one Majorana singlet (bino). We examine here cases where the mixing is suppressed and the neutralino is mostly wino or higgsino. This is the standard situation in (mini-)split supersymmetric scenarios, e. g. ^{7, 8}).

Detecting heavy DM particles directly or through collider experiments is challenging. However, it may be possible to detect indirect signals, like those from cosmic gamma-ray observations, in the near future ⁹). Large quantum effects resulting from the big hierarchies between the DM mass and the masses of the EW gauge bosons and the non-relativistic speeds of DM particles in nearby galaxies, could significantly enhance the DM-induced signals sought by indirect-detection experiments ^{10, 11}).

In this work, we focus on how the aforementioned quantum effects can be accounted for in a systematic way using a suitable effective field theory (EFT). Our focus is on the endpoint of the gamma-ray spectrum, characterized by a prominent line-like bump detectable with current and next-generation telescopes. In particular, we account for the effect of the otherwise negligible emissions of collinear and soft gauge bosons at the endpoint, which in this case play a very important role. Lastly, we introduce `DMγSpec`, a python library to calculate resummed gamma-ray annihilation cross sections for wino/higgsino.

This review is organized as follows: Section 2 covers the basic aspects of the computation of gamma-ray fluxes; Section 3 outlines the EFTs pertinent to this work (NREFT and SCET); Section 4 presents the numerical results; after which we summarize our findings in the conclusions.

2 Phenomenology

Very high energy (VHE) gamma rays from nearby sources, e. g. satellite dwarf galaxies or the Miky-Way halo, can pass through the interstellar medium unimpeded. Therefore, the differential flux (number of photons of energy between E and $E + dE$ per unit time and area) in a small cone centered in the \hat{n} direction, with a solid angle $d\Omega_{\hat{n}}$ is given by

$$d\Phi_{\gamma}(E) = dE d\Omega_{\hat{n}} \int_{\text{l.o.s.}} ds q(\hat{n}s) , \quad (1)$$

where $q(\hat{n}s)$ is the source function and is given by

$$q(\hat{n}s) = \frac{1}{8\pi m_{\chi}^2} \rho_{\text{DM}}^2(r(s\hat{n})) \frac{d\langle\sigma v\rangle}{dE} . \quad (2)$$

In this formula, m_{χ} is the mass of the DM particle, $\rho_{\text{DM}}(r)$ its density, $\langle\sigma v\rangle$ its velocity-averaged $\chi\chi \rightarrow \gamma + X$ annihilation cross section and X is any combination of particles associated with the annihilation process. For a review see e. g. ¹²). Assuming a velocity distribution of $\sim \delta^{(3)}(\mathbf{v})$, the differential flux can be expressed as the product of an astrophysical “ J ” factor and the differential annihilation cross-section, with $\langle\sigma v\rangle \simeq \lim_{v \rightarrow 0} \sigma v$. For a given observed angular region $\Delta\Omega$, this J -factor is defined as

$$J_{\hat{n}}(\Delta\Omega) = \int_{\Delta\Omega} d\Omega_{\hat{n}} \int_{\text{l.o.s.}} ds \rho_{\text{DM}}^2(r(s\hat{n})) , \quad (3)$$

Regarding the annihilation process, energy-momentum conservation dictates that the gamma-ray spectrum has a sharp cutpff at¹ $E = m_{\chi}$. In the idealized case, with e.g. infinite energy-resolution

¹We use natural units.

detectors, this would appear as a $\gamma\gamma$ line with no width. However, the finite energy resolution of the instrument will cause smearing of this signal. To properly address this, we must consider the more generic annihilation process $\chi\chi \rightarrow \gamma + X$, where X denotes all possible unobserved particles with an invariant mass $m_X = 2m_\chi\sqrt{1 - E/m_\chi} \equiv 2m_\chi\sqrt{1 - x}$ constrained by the instrument's energy resolution.

3 Non-relativistic and soft collinear effective field theories for DM

In order to gain insight into the complexity of the computation of gamma-ray spectra from TeV-scale DM, consider the fixed-order $\chi\chi \rightarrow \gamma\gamma$ amplitude

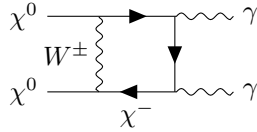


Figure 1: Illustrative Feynman diagram occurring in the $\chi\chi \rightarrow \gamma\gamma$ amplitude computation

The Feynman diagram shown above (Fig. 1) has several features that merit special attention. First, due to the fact that the DM is non-relativistic², the W -boson t -channel exchange depicted in the figure yields a very large $\sim \alpha_2^2 m_\chi/m_W$ contribution that invalidates the perturbative expansion. The leading order computation is thus insufficient and the effects of an infinite number of Feynman diagrams has to be included. We thus employ EFT methods to identify and resum large terms that would otherwise invalidate the perturbative expansion. More concretely, in the context of non-relativistic EFTs (NREFT) large terms of $\mathcal{O}(\alpha_2^n m_\chi^n/m_W^n)$ that occur in certain n -loop diagrams ($n = 1, 2, \dots$) can be resummed by solving a Schrödinger equation with static Yukawa potentials^{10, 11, 13}, e. g. $V(r) \sim \alpha_{\text{EW}} \frac{e^{-m_W r}}{r}$. Depending on the theory parameters (e. g. DM particle mass), the resummation yields phenomenologically interesting resonant effects (see Fig. 2).

Secondly, the $\chi\chi \rightarrow \gamma\gamma$ process is also affected by large Sudakov-like double logarithmic terms $\sim \alpha_2^2 \log^2(2m_\chi/m_W)$. The origin of these terms (and their higher-order counterparts) is also well understood and can be resummed using renormalization-group (RG) running in the context of a soft-collinear EFT (SCET)^{14, 15, 16, 17}.

Note that although the previous discussion was mostly concerned with the $\chi\chi \rightarrow \gamma\gamma$ process, this approach is applicable in the full $\chi\chi \rightarrow \gamma + X$ process near the endpoint. More concretely, the NR/SCET EFT for the $\chi\chi \rightarrow \gamma + X$ process features the following non-local operators¹⁷

$$\mathcal{L}_{\text{int}} \supset \frac{1}{2m_\chi} \int ds dt \hat{C}_i(s, t) \xi^{c\dagger} T_i^{VW} \xi \mathcal{A}_{+, \mu}^V(sn_+) \varepsilon_{\perp}^{\mu\nu} A_{-, \nu}^W(tn_-), \quad (4)$$

where n_+ and n_- are the four vectors that describe the collinear and anticollinear directions of the process and $\mathcal{A}_{\pm, \mu}^V$ are the associated (anti)collinear SCET building-block fields³. The remaining ξ fields are the non-relativistic (here fermionic) two-component spinor DM fields; the T_i^{VW} tensors are constructed in

²We adopt the stronger assumption that $v \ll \alpha_{\text{EW}}$, where α_{EW} refers to either the α_1 or α_2 couplings in the SM.

³The definition of these in terms of light-like Wilson lines is rather involved. We refer to e. g. ¹⁸) for a review.

such a way that electroweak symmetries are respected; and $\hat{C}_i(s, t)$ are the Wilson “coefficients” as functions of the t and s parameters that one introduces in the definition of the building-block (anti)collinear vector fields.

The resummation of the Sudakov double logs is completed once renormalization-group equations are solved for the several pieces of the annihilation-process’ *factorization formula*. The results depend on the assumptions made about the typical scale of the invariant mass of X . In this work we consider the following two validity regimes. Namely,

- ‘nrw’: $m_X \sim m_W$ or, equivalently $1 - x \sim m_W^2/(2m_\chi)^2$
- ‘int’: $m_X \sim \sqrt{2m_\chi m_W}$ or, equivalently $1 - x \sim m_W/(2m_\chi)$

The case in which m_X is treated as an independent parameter satisfying $2m_\chi \gg m_X \gg \sqrt{2m_\chi m_W}$ or $1 - x \gg m_W/(2m_\chi)$ (‘wide’) has been treated in Refs. 16, 19).

4 Resummed pure wino/higgsino spectra

In this section, we explain how to calculate endpoint gamma-ray spectra in pure wino and higgsino models. For the full MSSM, see the recent paper 20). Details about these models and associated experimental constraints can be found in e. g. 4, 21, 22, 23, 24). The key features of these are the following:

Wino: a massive fermionic *triplet* is added to the Standard Model (SM). After Electroweak Symmetry Breaking (EWSB), this produces one neutral Majorana particle (χ^0) and one electrically χ^\pm charged Dirac particle, with a mass splitting of ~ 165 MeV. This is a highly predictive theory, with only one free parameter: the DM mass. Assuming thermal freeze-out, this yields $m_\chi^{\text{wino}} \simeq 3$ TeV.

Higgsino: a spin-1/2 EW *doublet* is added to the SM, giving two neutral Majorana particles (χ_1^0, χ_2^0) and a charged Dirac particle (χ^\pm) after EWSB. Like in the wino model, a small mass splitting of ~ 355 MeV between the charged and the neutral particles is induced by EWSB. A dimension-5 operator $(1/\Lambda)\mathcal{O}_H^{\text{dim}5}$, where $\Lambda \gg m_\chi$, is required in order to introduce a mass splitting between the two neutral particles. The theory is, thus, characterized by two free parameters: m_χ and Λ (or $\delta m_\chi^{\text{hino}}$). In the wimp (thermal freeze-out) hypothesis, $m_\chi^{\text{hino}} \simeq 1$ TeV.

Exploring our resummed spectra further, we stress the obvious fact that χ in $\chi\chi \rightarrow \gamma + X$ refers to the LSP (e. g. χ_0^1 in the higgsino model). However, non-relativistic effects may cause the pair of DM particles to virtually transition into, say, a $\chi^+\chi^-$ state. These transitions will play an important role in our factorization formula. We thus introduce the following notation: all electrically neutral combinations of wino/higgsino field pairs will be denoted with the “collective” indices I or $J = (11), (+-), \dots$. This enables us to express our factorization formula as follows

$$\frac{d\langle\sigma v\rangle}{dx} = 2m_\chi \sum_{I,J} S_{IJ}\Gamma_{IJ}(x) . \quad (5)$$

The Sommerfeld factors, S_{IJ} , are independent of x , and account for the resummation of those $\mathcal{O}(\alpha_2^n m_\chi^n/m_W^n)$ terms that are associated to the non-relativistic initial-state kinematics. The associated non-relativistic potentials are known at next-to-leading order 25, 26). $\Gamma_{IJ}(x)$, however, depends on x

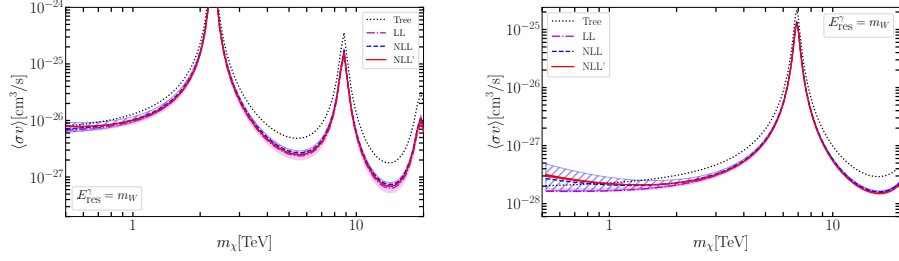


Figure 2: Cumulative $\chi\chi \rightarrow \gamma+X$ annihilation cross sections times relative speeds for pure wino (left) and higgsino (right) DM as a function of their particle’s mass. Our featured calculation at next-to-leading-log prime accuracy is shown as a solid (red) line. We include, for comparison, the NLL (dashed blue) and LL (dot-dashed magenta) computations with their associated theory-uncertainty bands. For concreteness, $E_\gamma^{\text{res}} = m_W$ is assumed (see text for the definitions). Figures taken from [17, 28]

and the factorization regime (i.e. ‘nrw’, ‘int’). In the higgsino model and ‘int’ regime, for instance, this reads [17]

$$\Gamma_{IJ}(x) = \frac{1}{(\sqrt{2})^{n_{id}}} \frac{1}{4} \frac{2}{\pi m_\chi} \sum_{i,j} C_i(\mu) C_j^*(\mu) \times Z_\gamma^{WY}(\mu, \nu) \times \int d\omega \left(J^{\text{SU}(2)}(4m_\chi(m_\chi - E_\gamma - \omega/2), \mu) \times W_{IJ,WY}^{\text{SU}(2),ij}(\omega, \mu, \nu) + J^{\text{U}(1)}(4m_\chi(m_\chi - E_\gamma - \omega/2), \mu) \times W_{IJ,WY}^{\text{U}(1),ij}(\omega, \mu, \nu) \right). \quad (6)$$

As evident in (6), the factorization formula is a product of several pieces. Namely, C_i : Wilson coefficients in momentum space of the SCET; Z_γ and $J^\mathcal{G}(m_X^2)$: photon and recoiling jet functions; and $W_{IJ,WY}^{\mathcal{G},ij}$: the soft function (tensor), where $\mathcal{G} = \text{U}(1)$ or $\text{SU}(2)$. Detailed expressions and proper definitions are given in Refs. [17, 27, 28].

Fig. 2 shows how uncertainties are gradually reduced as we increase the accuracy of our calculations and for large DM masses. In particular, our *next-to-leading logarithmic prime* (NLL’) computations are accurate to within a few percent. In this figure, we consider the cumulative cross-section as a function of the variable E_γ^{res} which is defined as

$$\langle\sigma v\rangle(E_\gamma^{\text{res}}) = \int_{1-E_\gamma^{\text{res}}/m_\chi}^1 dx' \frac{d\langle\sigma v\rangle}{dx'}. \quad (7)$$

These figures can also be obtained using a python library `DMySpec` [29] which, among other features, enables the user to numerically evaluate eqs. (5), (6) in the ‘int’ and ‘nrw’ validity regimes. `DMySpec` is also useful for plotting the *complete annihilation spectrum* for generic wino/higgsino DM. This is achieved by matching our results (5), (6) with gamma-ray spectra from parton showers initiated by all possible Born-level 2-2 annihilation processes. The former hold for small values of $1-x$, whereas the latter are valid as long as the collinear approximation is applicable and is given by (5) but instead of using (6) for Γ_{IJ} we use

$$\Gamma_{IJ}^{\text{MC}}(x) = \sum_{a,b} (\sigma v)_{(IJ)ab}^{(0)} \frac{1}{m_\chi} \frac{dN_{ab \rightarrow \gamma+X}^{\text{MC}}}{dx}, \quad (8)$$

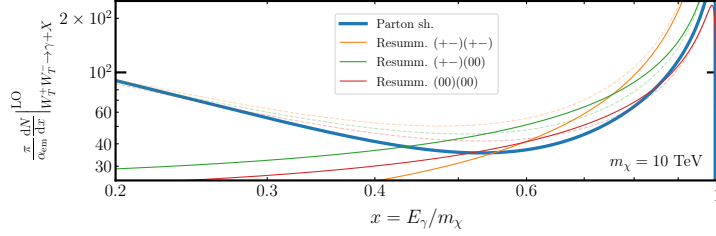


Figure 3: Fixed-order expanded $m_\chi \Gamma_{IJ}/(\sigma)_{IJ}^{(0)}$ using eq. (6) for the three possible combinations of I and J in the wino model ($m_\chi = 10$ TeV) considered here: in red $I = J = (00)$, etc. Dashed lines are obtained from full Born-level calculations. The (thick) blue line is the result of eq. (9). We use $s_W^2 = 0.222$.

where $a, b = W_T^\pm, Z_T$ or γ . The subscript T means *transverse* here and the upperscript (0) refers to the fact that the cross-section matrices are computed at tree level. For example, in the pure wino case:

$$\begin{aligned}
 (\sigma)_{IJ\gamma\gamma}^{\text{wino}(0)} &= \frac{s_W^2}{2c_W^2} (\sigma)_{IJ\gamma Z_T}^{\text{wino}(0)} = \frac{s_W^4}{c_W^4} (\sigma)_{IJ Z_T Z_T}^{\text{wino}(0)} = \frac{\pi \alpha_{\text{em}}^2}{m_\chi^2} \delta_{I,(+-)} \delta_{J,(+-)} \\
 (\sigma)_{(00)(00)W_T W_T}^{\text{wino}(0)} &= \sqrt{2} (\sigma)_{(00)(+-)W_T W_T}^{\text{wino}(0)} = 2 (\sigma)_{(+-)(+-)W_T W_T}^{\text{wino}(0)} = \frac{\pi \alpha_2^2}{m_\chi^2},
 \end{aligned}$$

where δ_{IJ} is the Kronecker delta, α_{em} is the fine-structure constant, and s_W and c_W are respectively the sine and cosines of the Weinberg angle in the SM. The splitting functions $dN_{X \rightarrow \gamma}^{\text{MC}}/dx$ are obtained from parton showers available in specialized software codes [30, 32, 31, 33].

The matching of these computations is remarkable. In order to understand why this happens, it is useful to compare the (unresummed) $\mathcal{O}(\alpha_{\text{EW}})$ terms associated to each calculation. Specifically, for the parton-shower approach, $dN_{a,b \rightarrow \gamma}^{(0)}/dx$ vanishes for $(a, b) = (Z_T, Z_T)$, (γZ_T) and $\gamma\gamma$ but is non-zero for $(a, b) = W_T^+ W_T^-$ and is given by [34]

$$\frac{dN_{W_T^+ W_T^- \rightarrow \gamma + X}^{(0)}}{dx} = \frac{2\alpha_{\text{em}}}{\pi} \left[\frac{x}{1-x} \log \frac{4m_\chi^2(1-x)^2}{m_W^2} + \left(\frac{1-x}{x} - x(1-x) \right) \log \frac{4m_\chi^2}{m_W^2} \right]. \quad (9)$$

Fig. 3 shows this for $m_\chi = 10$ TeV. The other curves shown there are obtained by performing fixed-order expansions in α_{EW} of (6). For $x \lesssim 0.5$, exact one-loop computations match the thick blue line, as expected. At the opposite end of the spectrum ($1-x \lesssim m_W/m_\chi \sim 0.01$ for $m_\chi = 10$ TeV), these computations are instead matched by our fixed-order expanded factorization formulas.

5 Conclusions

Indirect detection experiments will probe previously-unexplored regions of WIMP parameter-space in the near future. Radiative electroweak effects are an essential ingredient in the description of indirect-detection signals from TeV-scale dark matter. In particular, a proper treatment of Sudakov-log resummation and Sommerfeld enhancements is crucial in order to reliably assess these heavy WIMP scenarios.

To this end, we devised an EFT (NR/SCET) prescription to obtain fully resummed gamma-ray spectra from generic heavy DM with non-trivial EW multiplicities. In the pure wino and higgsino models we completed this at the NLL' accuracy of $\mathcal{O}(1\%)$. Furthermore, we developed DM γ Spec, a tool that makes it easy for Cherenkov telescope experiments to implement our wino/higgsino spectra. Our results show excellent agreement and consistency between its various pieces.

References

1. N. Aghanim *et al.* [Planck], *Astron. Astrophys.* **641** (2020), A6 [erratum: *Astron. Astrophys.* **652** (2021), C4] doi:10.1051/0004-6361/201833910 [arXiv:1807.06209 [astro-ph.CO]].
2. G. Arcadi, M. Dutra, P. Ghosh, M. Lindner, Y. Mambrini, M. Pierre, S. Profumo and F. S. Queiroz, *Eur. Phys. J. C* **78** (2018) no.3, 203 doi:10.1140/epjc/s10052-018-5662-y [arXiv:1703.07364 [hep-ph]].
3. L. Roszkowski, E. M. Sessolo and S. Trojanowski, *Rept. Prog. Phys.* **81** (2018) no.6, 066201 doi:10.1088/1361-6633/aab913 [arXiv:1707.06277 [hep-ph]].
4. M. Cirelli, N. Fornengo and A. Strumia, *Nucl. Phys. B* **753** (2006), 178-194 doi:10.1016/j.nuclphysb.2006.07.012 [arXiv:hep-ph/0512090 [hep-ph]].
5. N. Arkani-Hamed, A. Delgado and G. F. Giudice, *Nucl. Phys. B* **741** (2006), 108-130 doi:10.1016/j.nuclphysb.2006.02.010 [arXiv:hep-ph/0601041 [hep-ph]].
6. G. Jungman, M. Kamionkowski and K. Griest, *Phys. Rept.* **267** (1996), 195-373 doi:10.1016/0370-1573(95)00058-5 [arXiv:hep-ph/9506380 [hep-ph]].
7. N. Arkani-Hamed, S. Dimopoulos, G. F. Giudice and A. Romanino, *Nucl. Phys. B* **709** (2005), 3-46 doi:10.1016/j.nuclphysb.2004.12.026 [arXiv:hep-ph/0409232 [hep-ph]].
8. A. Arvanitaki, N. Craig, S. Dimopoulos and G. Villadoro, *JHEP* **02** (2013), 126 doi:10.1007/JHEP02(2013)126 [arXiv:1210.0555 [hep-ph]].
9. A. Acharyya *et al.* [CTA], *JCAP* **01** (2021), 057 doi:10.1088/1475-7516/2021/01/057 [arXiv:2007.16129 [astro-ph.HE]].
10. J. Hisano, S. Matsumoto and M. M. Nojiri, *Phys. Rev. Lett.* **92** (2004), 031303 doi:10.1103/PhysRevLett.92.031303 [arXiv:hep-ph/0307216 [hep-ph]].
11. J. Hisano, S. Matsumoto, M. M. Nojiri and O. Saito, *Phys. Rev. D* **71** (2005), 063528 doi:10.1103/PhysRevD.71.063528 [arXiv:hep-ph/0412403 [hep-ph]].
12. M. Lisanti, doi:10.1142/9789813149441_0007 [arXiv:1603.03797 [hep-ph]].
13. M. Beneke, C. Hellmann and P. Ruiz-Femenia, *JHEP* **05** (2015), 115 doi:10.1007/JHEP05(2015)115 [arXiv:1411.6924 [hep-ph]].
14. M. Baumgart, I. Z. Rothstein and V. Vaidya, *Phys. Rev. Lett.* **114** (2015), 211301 doi:10.1103/PhysRevLett.114.211301 [arXiv:1409.4415 [hep-ph]].
15. M. Bauer, T. Cohen, R. J. Hill and M. P. Solon, *JHEP* **01** (2015), 099 doi:10.1007/JHEP01(2015)099 [arXiv:1409.7392 [hep-ph]].
16. M. Baumgart, T. Cohen, I. Moulton, N. L. Rodd, T. R. Slatyer, M. P. Solon, I. W. Stewart and V. Vaidya, *JHEP* **03** (2018), 117 doi:10.1007/JHEP03(2018)117 [arXiv:1712.07656 [hep-ph]].
17. M. Beneke, A. Broggio, C. Hasner, K. Urban and M. Vollmann, *JHEP* **08** (2019), 103 [erratum: *JHEP* **07** (2020), 145] doi:10.1007/JHEP08(2019)103 [arXiv:1903.08702 [hep-ph]].

18. T. Becher, A. Broggio and A. Ferroglia, *Lect. Notes Phys.* **896** (2015), pp.1-206 Springer, 2015, doi:10.1007/978-3-319-14848-9 [arXiv:1410.1892 [hep-ph]].
19. M. Baumgart, T. Cohen, E. Moulin, I. Moul, L. Rinchiuso, N. L. Rodd, T. R. Slatyer, I. W. Stewart and V. Vaidya, *JHEP* **01** (2019), 036 doi:10.1007/JHEP01(2019)036 [arXiv:1808.08956 [hep-ph]].
20. M. Beneke, S. Lederer and C. Peset, *JHEP* **01** (2023), 171 doi:10.1007/JHEP01(2023)171 [arXiv:2211.14341 [hep-ph]].
21. J. Fan and M. Reece, *JHEP* **10** (2013), 124 doi:10.1007/JHEP10(2013)124 [arXiv:1307.4400 [hep-ph]].
22. T. Cohen, M. Lisanti, A. Pierce and T. R. Slatyer, *JCAP* **10** (2013), 061 doi:10.1088/1475-7516/2013/10/061 [arXiv:1307.4082 [hep-ph]].
23. K. Kowalska and E. M. Sessolo, *Adv. High Energy Phys.* **2018** (2018), 6828560 doi:10.1155/2018/6828560 [arXiv:1802.04097 [hep-ph]].
24. R. T. Co, B. Sheff and J. D. Wells, *Phys. Rev. D* **105** (2022) no.3, 035012 doi:10.1103/PhysRevD.105.035012 [arXiv:2105.12142 [hep-ph]].
25. M. Beneke, R. Szafron and K. Urban, *JHEP* **02** (2021), 020 doi:10.1007/JHEP02(2021)020 [arXiv:2009.00640 [hep-ph]].
26. K. Urban, *JHEP* **10** (2021), 136 doi:10.1007/JHEP10(2021)136 [arXiv:2108.07285 [hep-ph]].
27. M. Beneke, A. Broggio, C. Hasner and M. Vollmann, *Phys. Lett. B* **786** (2018), 347-354 [erratum: *Phys. Lett. B* **810** (2020), 135831] doi:10.1016/j.physletb.2018.10.008 [arXiv:1805.07367 [hep-ph]].
28. M. Beneke, C. Hasner, K. Urban and M. Vollmann, *JHEP* **03** (2020), 030 doi:10.1007/JHEP03(2020)030 [arXiv:1912.02034 [hep-ph]].
29. M. Beneke, K. Urban and M. Vollmann, *Phys. Lett. B* **834** (2022), 137248 doi:10.1016/j.physletb.2022.137248 [arXiv:2203.01692 [hep-ph]].
30. M. Cirelli, G. Corcella, A. Hektor, G. Hutsi, M. Kadastik, P. Panci, M. Raidal, F. Sala and A. Strumia, *JCAP* **03** (2011), 051 [erratum: *JCAP* **10** (2012), E01] doi:10.1088/1475-7516/2012/10/E01 [arXiv:1012.4515 [hep-ph]].
31. T. Bringmann and J. Edsjö, *PoS CompTools2021* (2022), 038 doi:10.22323/1.409.0038 [arXiv:2203.07439 [hep-ph]].
32. G. Belanger, F. Boudjema, A. Pukhov and A. Semenov, *Comput. Phys. Commun.* **185** (2014), 960-985 doi:10.1016/j.cpc.2013.10.016 [arXiv:1305.0237 [hep-ph]].
33. T. Bringmann *et al.* [GAMBIT Dark Matter Workgroup], *Eur. Phys. J. C* **77** (2017) no.12, 831 doi:10.1140/epjc/s10052-017-5155-4 [arXiv:1705.07920 [hep-ph]].
34. P. Ciafaloni, D. Comelli, A. Riotto, F. Sala, A. Strumia and A. Urbano, *JCAP* **03** (2011), 019 doi:10.1088/1475-7516/2011/03/019 [arXiv:1009.0224 [hep-ph]].

QCD-like strongly interacting dark matter at colliders

Suchita Kulkarni

Institute of Physics, NAWI Graz, University of Graz, Universitätsplatz 5, A-8010 Graz, Austria

Abstract

Understanding the laws governing the dark matter dynamics in the Universe is undoubtedly one of the pressing questions in astro-particle physics. While elementary particles as potential dark matter candidates have been at the heart of investigations, an equally interesting possibility arises if dark matter is a composite particle. We take an overview of dark matter theories arising from extensions of Standard Model with new non-Abelian sectors. Analysis of such dark sector dynamics benefits from connections to lattice calculations. We sketch the avenues of progress and highlight some of the open questions in this direction. We also take a few example realisations of such strongly interacting dark matter theories and exemplify associated phenomenology.

1 Introduction

New extensions of the Standard Model (SM) containing confining non-Abelian gauge groups which contain a stable composite particle to be associated with dark matter (DM) are dubbed strongly interacting dark matter scenarios. In such extensions in the ultraviolet (UV) regime, the non-Abelian gauge groups contain some matter fields, here taken as dark quarks in fundamental representation of the gauge group, and corresponding massless gauge bosons. At low energies, after confinement, the quarks combine to form a spectrum of bound states. The dark matter candidate is realised in this low energy i.e. infrared (IR) spectrum and hence is a part of a larger dark sector (DS). These scenarios resemble composite Higgs scenarios, which may also present with a stable state which can be associated with DM. Strongly interacting dark matter scenarios are however distinct from composite Higgs theories. While composite Higgs scenarios feature a SM Higgs-like state and thus fixes the scale of composite sector, the strongly interacting dark matter scenarios do not have such association with and offer larger freedom in realisations.

Interactions between SM and non-Abelian sectors are introduced to ensure DM - SM thermal equilibrium, and they also present with interesting experimental signatures. No specific requirements for the mediator properties are yet established apart from ensuring the stability of DM and existing experimental constraints. Such scenarios, particularly featuring dark pions (π_D) as DM candidates offer interesting possibilities to reconcile required large DM self-interaction cross-sections with relic density requirements, while obeying stringent constraints on DM - SM interactions ¹⁾.

Strongly interacting dark matter scenarios thus not only present with interesting cosmological analysis but also with new experimental signatures. In the following sections, we will concentrate on QCD-like strongly interacting theories. By QCD-like scenarios, we mean, scenarios where the dark strong coupling becomes asymptotically free, similar to the strong running coupling (α_s) of the SM quantum chromodynamics sector (QCD). Under these conditions, for mass degenerate dark quarks the new non-Abelian sector can be characterised by four free parameters: they can be dark quark mass (m_{q_D}), dark strong coupling (α_D), the number of dark flavours (N_{f_D}) and the dimension of the gauge group (N_{c_D}) in the UV. The continuous parameters m_{q_D}, α_D can be traded for one dimensionless ratio e.g. m_{ρ_D}/m_{π_D} or m_{π_D}/Λ_D and one scale e.g. m_{π_D} or Λ_D , where Λ_D is the confinement scale of the theory. The low energy interactions of such theory can then be computed by means of chiral perturbation theory, the input parameters for this chiral Lagrangian such as the bound state masses or decay constants are however supplied by other means such as lattice calculations.

2 Standard Model mediators

It is possible to introduce SM - DS coupling using one of the existing mediators within the SM. Here, we take an example of the SM Higgs mediator which couples an $SU(N_{c_D})$ gauge groups with vector-like 4 Dirac fermions ($N_{f_D} = 4$). This model was first presented in ²⁾ and the results presented here were derived in ³⁾. In order to introduce SM Higgs mediator, part of the dark $SU(4)$ matter content needs to be charged under the SM gauge groups. This means electroweak symmetry breaking introduces small dark quark masses and breaks the $SU(4)$ flavour multiplet.

At low energies, the spectrum consists of 15 dark pions and rho mesons (corresponding to $N_{f_D}^2 - 1$ number of broken and unbroken generators), and the DM becomes lightest scalar baryons, which is stabilised by means of the dark baryon number. Since the $SU(4)$ flavour symmetry is broken the pion and rho multiplets are also broken as $15 \rightarrow (3, 1) \oplus (2, 2) \oplus (2, 2) \oplus (1, 3) \oplus (1, 1)$, where (3,1) and (1,3) triplets can be identified as triplets under custodial $SU(2)_L$ and $SU(2)_R$ subgroups of the overall $SU(4)$ symmetry. Depending on the gauging of the entire $SU(2)_L$ or $U(1)_Y$ part of the $SU(2)_R$ gauge group, either the entire rho triplet mixes with SM electroweak gauge bosons or only the neutral component mixes with the $U(1)_Y$ boson. More importantly, this introduces a production mechanism at the LHC, followed by the decays of dark rho mesons to two dark pions or to SM fermions depending on the threshold. The dark pions also undergo similar breaking pattern and decay to SM fermions through well-known chirality suppression, leading to tau-enriched final states at the LHC.

At direct detection experiments, the scalar baryon scatters off nuclei and can lead to signatures at e.g. Xenon experiment. These scattering amplitudes can be expressed as

$$\mathcal{M}_{p,n} = \frac{g_{p,n} g_{DM}}{m_h^2} \quad (1)$$

with

$$g_{p,n} = \frac{m_{p,n}}{v} \left[\sum_{q=u,d,s} f_q^{(p,n)} + \frac{6}{27} \left(1 - \sum_{q=u,d,s} f_q^{(p,n)} \right) \right] \quad (2)$$

and

$$g_{DM} \simeq y_{\text{eff}} f_f^{DM}, \quad (3)$$

where y_{eff} is the effective dark quark Higgs coupling and the dark baryon form factors f_f^{DM} are calculated on lattice. $m_{p,n}$ is the mass of SM proton/neutron, v is the Higgs vacuum expectation value, $f_q^{(p,n)}$ are the SM proton/neutron form factors. The lattice calculations are tabulated in table 1, which can be used for phenomenological analysis.

In this work, we used the measurements of SM differential cross sections via the public code CONTUR^{4, 5)} in order to evaluate the LHC constraints on the model parameter space. The resulting limits in the plane of DM mass and pion to rho mass ratio (η) are displayed in fig.1 (left panel). The two lines correspond to gauging of the $SU(2)_L$ or the $SU(2)_R$ subgroups. In the middle panel, we show the constrains on DM scattering cross section superimposed with the current limits from Xenon1T for $\eta = 0.77$ for $SU(2)_L$ gauged group only. Finally in the rightmost panel, the two limits are combined for $SU(2)_L$ group. For a fixed value of η , the regions below the dot-dashed lines are excluded by the LHC searches, while the regions above the solid lines are excluded by the direct detection constraints. In general it shows that the DM masses should be high or the couplings should be small for such scenarios to be viable.

η	$amps$	amv	$amS0$	f_f^{DM}
0.77	0.3477	0.4549	0.9828	0.153
0.70	0.2886	0.4170	0.8831	0.262
0.50	0.2066	0.3783	0.7687	0.338

Table 1: Lattice inputs for $\beta = 11.028$ on $32^3 \times 64$ lattices taken from²⁾ for this work. $amps$, amv and $amS0$ represent dimensionless pseudo-scalar, vector and dark baryon masses while $f_f^{(DM)}$ is lattice input for computing DM direct-detection cross-section via Higgs exchange.

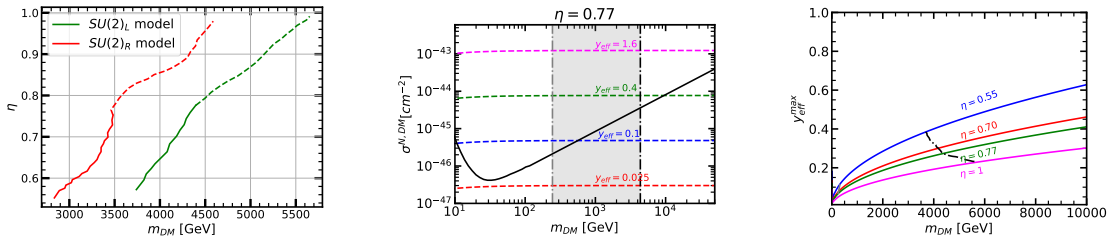


Figure 1: a) Constraints on DM mass as a function of dark pion to rho mass ratio (η) b) Colored contours show DM-SM scattering cross-sections for fixed value of y_{eff} , vertical lines represent m_{DM} limits derived from LEP limits on pion mass (grey dot-dashed line) and updated LHC constraints derived in this work (black dot-dashed line). Also overlaid are the recent Xenon1T constraints on DM-nucleon coherent scattering⁶⁾.

3 New mediators

The stringent constraints placed on the DM mass by means of SM mediators forces introduction of new mediators. The dark quarks are thus vector-like and are singlets under the SM gauge groups and any SM - DS interactions are only mediated by the new mediator. In particular we consider the case of a massive $U(1)_D$ gauge boson (Z').

3.1 New $SU(N_{c_D})$ sectors

We first consider SM extension by an $SU(N_{c_D})$ gauge group and couple it with the SM via a $U(1)_D$ boson (Z'). The SM is thus augmented by $SU(N_{c_D}) \times U(1)_D$ symmetry. In such cases, new experimental signatures can emerge. In particular, at colliders such as the LHC, these scenarios can give rise to new jet-like final states if $m_{Z'} \gg \Lambda_D$. Simulating such signatures needs great care, as unphysical input parameters may lead to unphysical correlations. We therefore summarise and discuss some of the suggestions for consistent definitions of the input parameters. These were first discussed in the snowmass darkshowers report ⁷⁾.

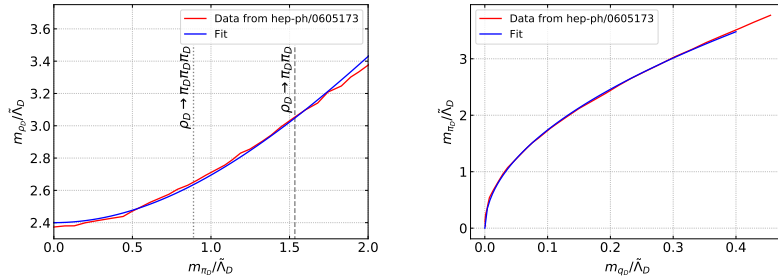


Figure 2: Fits given in Eq.4 for the ρ_D mass (left) and π_D mass (right) to results from lattice simulations ⁸⁾. The left panel also indicates the kinematic thresholds for ρ_D to decay to $\pi_D \pi_D$ and $\pi_D \pi_D \pi_D$. Figure taken from ⁷⁾.

The formation of darkjets, i.e. jets resulting from parton shower and hadronization of the dark sector quarks takes place under specific conditions. In particular, it needs $m_{Z'} \gg \Lambda_D$, assuming chiral limits. In the resulting hadronization, the masses of dark rho and pions are user defined quantities. Within the snowmass darkshowers project ⁷⁾, we embarked on setting first consistency conditions for darkjets simulations. The masses of dark rho and pions can be derived using lattice simulations. Current investigations of $SU(N)$ gauge groups with fermions in fundamental representations imply that the rho and pion masses are independent of the dimension of gauge group and number of flavours. With this observation, the fits to dimensionless rho and pion masses are given in eq. 4. These fits should be used for $m_{\pi_D}/\Lambda_D < 2$. Further details of the validity and limitations of these fits are explained in ⁷⁾ and we recommend the reader to carefully read the relevant sections of the report. The corresponding comparison between the analytical formulae and the lattice fits is shown in fig.2.

$$\frac{m_{\pi_D}}{\Lambda_D} = 5.5 \sqrt{\frac{m_{q_D}}{\Lambda_D}} \quad \frac{m_{\rho_D}}{\Lambda_D} = \sqrt{5.76 + 1.5 \frac{m_{\pi_D}^2}{\Lambda_D^2}} \quad (4)$$

The second important quantity for darkjet simulation is the decays of the dark rho and pions. The dark pions, if they decay, will decay via the well-known chirality suppressed modes, while the decays of

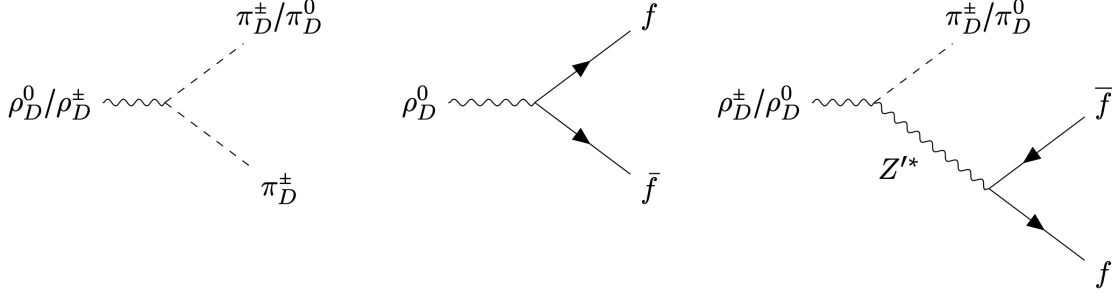


Figure 3: Decay modes of diagonal and off-diagonal dark rho mesons for regime 1 (left hand side) and regime 2 (middle and right hand side). Figure taken from ⁷⁾.

rho mesons are more varied and depend on the phase space and flavour breaking patterns. In particular, we show the decay modes qualitatively in fig.3. The diagram on the left is viable if the rho to pi decay mode is open, the diagram in the middle is applicable to all the singlet rho mesons which result due to coupling with the $U(1)_D$ mediator, while the diagrams on the right are applicable to the rho mesons decaying via the anomalous interactions. It is important to note that the three body decays of dark rho mesons have not been studied in the current darkjets literature.

3.2 New $Sp(N_{c_D})$ sectors

The $SU(N_{c_D})$ gauge groups with fermions in fundamental representations are worth studying due to the familiarity with them. For such theories, a minimum of 3 fermions are necessary in order to generate viable Wess-Zumino-Witten (WZW) term responsible for generating relic density through $3 \rightarrow 2$ cannibalisation processes. Could one construct a theory with more minimal matter content which can still lead to viable WZW term? An example of such construction is the $Sp(N_{c_D})$ gauge group with fermions fundamental representation. Since the fundamental representation in $Sp(N_{c_D})$ gauge group is pseudoreal, the flavour symmetry is enhanced and resulting coset space $SU(2N_{f_D})/Sp(2N_{f_D})$ contains $(2N_{f_D} + 1)(2N_{f_D} - 1)$ broken generators. This allows for a more minimal matter content while retaining the key features of strongly interacting theories. With this motivation, a consistent Lagrangian for $Sp(4)$ gauge group with $N_{f_D} = 2$ fermions was studied in detail in ⁹⁾. We summarise the key features here.

As alluded before, the flavour symmetry breaking patterns are different for complex versus pseudo-real representations. as an illustration, the breaking pattern for 2 flavours in the two representations is shown in fig.4. It is worth noting that the figure also illustrates breaking pattern for isospin symmetry breaking theories.

Another important feature of pseudoreal representations is the number of rho mesons. For complex representations, the number of broken and unbroken generators after chiral symmetry breaking is $N_{f_D}^2 - 1$, which leads to equal number of pion and rho mesons. For pseudoreal representations, the number of broken and unbroken generators are different and thus lead to different number of pion and rho mesons. In particular, the theories considered in ⁹⁾ contain five pions useful for generating WZW terms and ten rho mesons. The corresponding rho and pion multiplets are shown in 5. This figure also shows the effects of isospin symmetry breaking. In particular, it shows that under isospin symmetry breaking, both the complex representation ($SU(3)$ flavour symmetry) and the pseudoreal representation ($Sp(4)$) symmetry

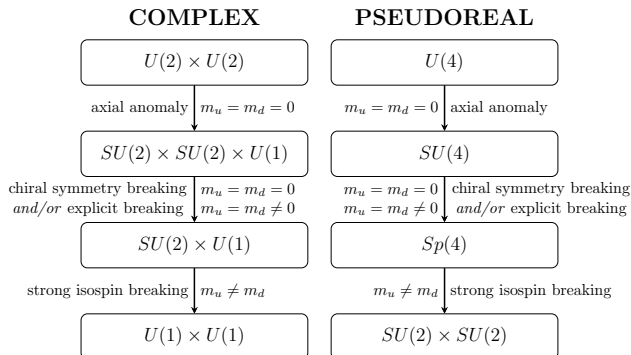


Figure 4: Illustration of the breaking of flavour symmetry for $N_{fD} = 2$ in case of a complex representation and comparison with the pseudoreal representation. Figure taken from ⁹).

contain a singlet which is not protected against decays.

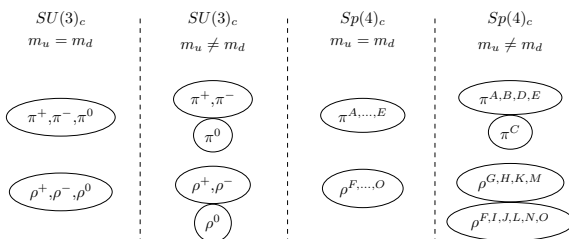


Figure 5: Comparison of dark rho and pion multiplets in $SU(3)$ gauge theory vs. $Sp(4)$ gauge theory. For comparison, we also show the multiplet breaking patterns in case of isospin symmetry breaking. Figure taken from ⁹).

Finally, charging such sectors under external $U(1)_D$ mediators also leads to flavour symmetry breaking. In case dark pions are required to be dark matter candidates, the $U(1)_D$ charges of the dark quarks are determined by requirement of pion stability. Requiring that anomalous decays of dark pion ($\pi_D \rightarrow Z'Z'$) vanish leads to dark quark charges of $Q = (+1, -1)$ for a two flavour theory. Under such $U(1)_D$ charging, the pion multiplets breaks into a $SU(2) \times U(1)$ for a complex representation while the multiplet breaks as $SU(2) \times SU(2) \times U(1)$ for a pseudoreal representation. The latter naturally preserves pion stability due to the multiplet structure.

The underlying chiral Lagrangian along with some of the low energy constants for this theory and detailed lattice investigations for isospin breaking scenario are detailed in ⁹).

4 Conclusions

Strongly interacting dark matter scenarios are an attractive theoretical landscape. They present new cosmological analysis and previously unexplored signatures at the experiments. Analysing these scenarios requires a combination of methods and results from different fields. In particular combining an analysis of symmetry breaking patterns and chiral perturbation theory, where applicable, sets a fertile ground for analytical calculations. The necessary inputs such as the masses and low energy constants however need

to be determined by non-perturbative techniques such as lattice calculations or holographic QCD. Setting up such a consistent theoretical framework is necessary to identify new experimental signatures and to draw meaningful conclusions on the underlying theory parameter space.

We presented several examples of such interplay between consistent theoretical setup supplemented by lattice calculations in the context of strongly interacting dark matter scenarios. In particular, we exemplified the role of SM - DS portals, the associated flavour symmetry breaking introduced by such portals and corresponding experimental signatures. Going beyond the well familiar $SU(N_{c_D})$ gauge group with fermions in fundamental representations, we also summarised an example of $Sp(4)$ gauge group where fundamental representation corresponds to pseudoreality. We sketched several attractive features of such theories and illustrated the stability of dark pion dark matter under coupling with an external $U(1)_D$ gauge group.

5 Acknowledgements

Suchita Kulkarni is supported by the FWF Austrian Science Fund research teams grant STRONG-DM (FG1).

References

1. Y. Hochberg, E. Kuflik, H. Murayama, T. Volansky and J. G. Wacker, *Model for Thermal Relic Dark Matter of Strongly Interacting Massive Particles*, *Phys. Rev. Lett.* **115** (2015) 021301, [1411.3727].
2. LATTICE STRONG DYNAMICS (LSD) collaboration, T. Appelquist et al., *Composite bosonic baryon dark matter on the lattice: $SU(4)$ baryon spectrum and the effective Higgs interaction*, *Phys. Rev. D* **89** (2014) 094508, [1402.6656].
3. J. M. Butterworth, L. Corpe, X. Kong, S. Kulkarni and M. Thomas, *New sensitivity of LHC measurements to composite dark matter models*, *Phys. Rev. D* **105** (2022) 015008, [2105.08494].
4. J. M. Butterworth, D. Grellscheid, M. Krämer, B. Sarrazin and D. Yallup, *Constraining new physics with collider measurements of Standard Model signatures*, *JHEP* **03** (2017), 078 doi:10.1007/JHEP03(2017)078 [1606.05296].
5. A. Buckley, J. M. Butterworth, L. Corpe, M. Habedank, D. Huang, D. Yallup, M. Altakach, G. Bassman, I. Lagwankar and J. Rocamonde, *et al. Testing new physics models with global comparisons to collider measurements: the Contur toolkit*, *SciPost Phys. Core* **4** (2021), 013 doi:10.21468/SciPostPhysCore.4.2.013 [2102.04377].
6. XENON collaboration, E. Aprile et al., *Dark Matter Search Results from a One Ton-Year Exposure of XENON1T*, *Phys. Rev. Lett.* **121** (2018) 111302, [1805.12562].
7. G. Albouy et al., *Theory, phenomenology, and experimental avenues for dark showers: a Snowmass 2021 report*, 2203.09503.
8. C. S. Fischer, *Infrared properties of QCD from Dyson-Schwinger equations*, *J. Phys. G* **32** (2006) R253–R291, [hep-ph/0605173].
9. S. Kulkarni, A. Maas, S. Mee, M. Nikolic, J. Pradler and F. Zierler, *Low-energy effective description of dark $Sp(4)$ theories*, 2202.05191.

Phases of condensed dark matter with a Yukawa interaction

Raghuveer Garani

INFN Sezione di Firenze, Via G. Sansone 1, I-50019 Sesto Fiorentino, Italy

Abstract

We explore possible phases of a condensed dark matter (DM) candidate taken to be in the form of a fermion with a Yukawa coupling to a scalar particle, at zero temperature but at finite density. This theory essentially depends on only four parameters, the Yukawa coupling, the fermion mass, the scalar mediator mass, and the DM density. At low fermion densities we delimit the Bardeen-Cooper-Schrieffer (BCS), Bose-Einstein Condensate (BEC) and crossover phases as a function of model parameters using the notion of scattering length. We further study the BCS phase by consistently including emergent effects such as the scalar density condensate and superfluid gaps. Within the mean field approximation, we derive the consistent set of gap equations valid in both the non-relativistic and relativistic regimes. Numerical solutions to the set of gap equations are presented, in particular when the mediator mass is smaller and larger than the DM mass. Finally, some possible astrophysical implications for asymmetric DM are discussed, including the case of a nightmare scenario where DM interacts only gravitationally with visible sector.

1 Introduction

The nature of DM remains unknown. This work is based on refs. ^{1, 2)} that details self-interacting DM models. Here, we focus mostly on the less studied possibility that condensed fermionic DM particles can manifest emergent phenomena. We will first setup the model and establish which phases (BCS or BEC) DM may form at low temperatures, depending on the model parameters. Next, We focus on the case where DM particles are in a BCS phase and derive the consistent set of gap equations, taking into account the change of DM mass at finite density due to the formation of a scalar condensate. Numerical solutions to the gap equation are then presented. Several technical results which may be of interest to a broad audience can be found in the appendix of ref. ¹⁾. Finally, tangential to the above topic we will also discuss the nightmare scenario for DM that arises from confining dark QCD.

2 Phase diagram in the Yukawa theory

The starting point is a degenerate gas of Dirac fermions ψ (the asymmetric DM) with a Yukawa coupling g to a real scalar ϕ (the mediator)

$$\mathcal{L} = i\bar{\psi}\not{\partial}\psi - m\bar{\psi}\psi + \mu\bar{\psi}\gamma^0\psi + \frac{1}{2}\partial_\mu\phi\partial^\mu\phi - \frac{1}{2}m_\phi^2\phi^2 - g\bar{\psi}\psi\phi. \quad (1)$$

The fermion ψ and the mediator ϕ are singlets of the Standard Model (SM) but ψ is charged under a global dark $U(1)$ symmetry. Therefore μ is the chemical potential conjugate to DM fermion number N in a volume V , corresponding to a DM density $n = N/V \equiv \langle\bar{\psi}\gamma^0\psi\rangle$. The expectation value $\langle\dots\rangle$ is on the ground state of the system, here taken to be at finite fermion density but at zero temperature. The motivation leading to these choices are phenomenological; for example, DM at the centers of galaxies or dwarf galaxies are at finite density and very cold (small velocity dispersions). For a degenerate gas of free fermions $g \rightarrow 0$, the chemical potential is equal to the Fermi energy E_F , $\mu = E_F \equiv \sqrt{m^2 + k_F^2}$ and $n = k_F^3/3\pi^2$. In eq. 1, m and m_ϕ denote the bare fermion and boson masses at zero density. Both are modified in a medium and, in particular, at finite density. The most dramatic effect is the change of the fermion mass. In this case, physically, the scalar operator $\bar{\psi}\psi$ has a non-zero mean, $n_s = \langle\bar{\psi}\psi\rangle > 0$ ³⁾.

In the non-relativistic limit, the nature of the low density phase can be qualitatively understood by examining the scattering length (a) of the fermions. While this is part of the standard toolbox of condensed matter physics, it is less common in the high energy physics literature. For a Yukawa

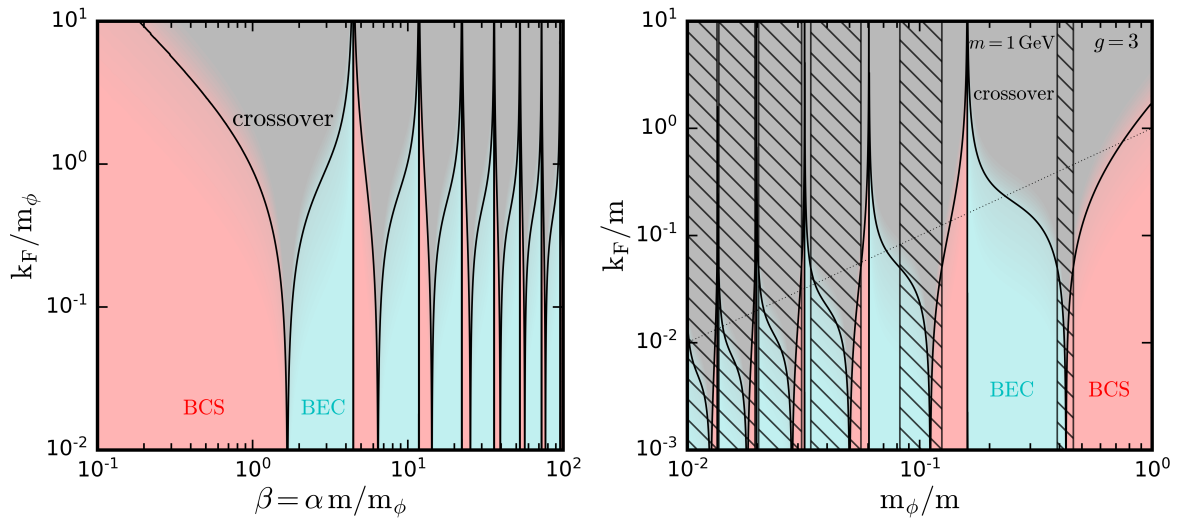


Figure 1: Contours of $(k_F a)^{-1}$. Red shaded regions are characterized by $(k_F a)^{-1} < -1$ indicating BCS regime. In the cyan shaded regions $(k_F a)^{-1} > 1$ indicating BEC regime, and the gray regions correspond to possible BEC-BCS crossover with $-1 < (k_F a)^{-1} < 1$. Contours of $(k_F a)^{-1}$ as a function of Fermi momentum and mediator mass. In the right panel we have set $m = 1$ GeV. The hatched shaded regions are excluded by Bullet Cluster limits on the self-interaction cross section of DM, $\sigma/m > 1$ cm²/g.

interaction, the s-wave scattering length for the singlet, spin 0 channel reads

$$\lim_{k \rightarrow 0} k \cot \delta_0(k) = -\frac{1}{a}, \quad (2)$$

where $\delta_0(k)$ is the s-wave phase shift. Obtaining this quantity requires solving the Schrödinger equation for the scattering problem. Applied to a degenerate system of fermions at finite density with Fermi

momentum k_F , the phases can then be characterized in terms of the dimensionless parameter $k_F a$. In this work, to map the model parameters of the theory described by eq. (1) to the possible phases of condensed DM, we go beyond the above contact interaction approximation and compute directly the scattering length by solving the Schrödinger equation. We can determine parameters of the Yukawa theory for which DM particles are clearly in the BCS (large negative $k_F a$) or in the BEC (large positive $k_F a$) phases. This result is depicted in fig. 1 as function of the dimensionless parameters $\beta = \alpha m/m_\phi$ with $\alpha = g^2/4\pi$ and the ratio of length scales k_F/m_ϕ . The Born approximation corresponds to $\beta \ll 1$, so we can expect the onset of bound state formation (and thus BEC phases) to be around $\beta \sim 1$. However, the sign of a changes each time a new bound state channel opens, so the relation between the possible phases and the parameters is complex. The other parameter (k_F/m_ϕ) is simply a measure of the mean particle separation over the range of the Yukawa potential, large k_F/m_ϕ corresponding to large densities. In fig. 1, the red shaded regions indicate the BCS phase, which we define to correspond to $(k_F a)^{-1} < -1$, a value motivated by the results obtained based on the contact interaction approximation, see e.g. (4). The cyan shaded regions are characterized by $(k_F a)^{-1} > 1$ and are delimiting the BEC phase. The gray shaded areas show the intermediate crossover phase, $-1 < (k_F a)^{-1} < 1$. The unitarity limit is reached when $k_F |a| \rightarrow \infty$, indicating crossover regime at all densities, which is seen as a feature in fig. 1. Further, for finite densities, the cases of anti-resonance $k_F a \rightarrow 0$ are captured by the peaks delimiting BEC to BCS transitions.

In the context of DM self interactions, in the right panel of fig. 1, we show the phase diagram of the Yukawa theory in the $k_F/m - m_\phi/m$ plane for a dark matter candidate of mass $m = 1$ GeV for $g = 3$. The gray dotted line corresponds to $k_F = m_\phi$. We overlay the constraints (hatched regions) on the dark matter self-interaction cross section at the scale of the Bullet Cluster, requiring $\sigma/m \lesssim 1$ cm²/g at a velocity of $v = 2000$ km/s. For such DM candidate, we find that $a m > 20$ is excluded. The corresponding excluded mediator mass range m_ϕ is shaded in gray. As could be expected, the unitarity regime are excluded, as is most of the very light mediator regime. The very fine viable intervals of m_ϕ correspond to vanishing self-interactions, *i.e.* $a \rightarrow 0$. This nicely illustrates the possibility for a dark sector to manifest emergent phenomenon like superfluidity, while being not entirely excluded by self interaction constraints on DM.

3 BCS phase: the consistent set of gap equations

We have so far described the low density phases of the Yukawa theory with no reference to the details of superfluidity. In this section, we study in detail the BCS gap matrix $\Delta \equiv \langle \psi_c \bar{\psi} \rangle$, with ψ_c being the charge conjugate of ψ .

3.1 Gap Dirac structure

We will consider a general ansatz for the 4×4 gap matrix $\Delta = \langle \psi_c \bar{\psi} \rangle$. We work in the rest frame of the fermion gas, which is assumed to be infinite and homogeneous. In this case, one can be easily convinced that the Δ matrix can be written as a sum of up to 8 translation invariant terms that can be expressed using the Clifford basis of matrices built upon the Dirac γ^μ and γ_5 (6, 5). As the Yukawa theory preserves parity, we expect that the gap matrix is also parity symmetric. Also, the ground state is expected to be rotationally invariant. This implies that pairing of fermions should be in $J^P = 0^+$ channel. This allows us to express the gap matrix Δ in terms of only 3 gap functions (the gaps in the sequel): $\Delta \equiv \langle \psi_c \bar{\psi} \rangle = \Delta_1 \gamma_5 + \Delta_2 \vec{\gamma} \cdot \hat{k} \gamma_0 \gamma_5 + \Delta_3 \gamma_0 \gamma_5$. The task is then to determine self-consistently these gaps, together with the scalar condensate $n_s = \langle \bar{\psi} \psi \rangle$. While this is not a new problem, to our knowledge it has not been worked out in the framework of the Yukawa theory. We will show that the

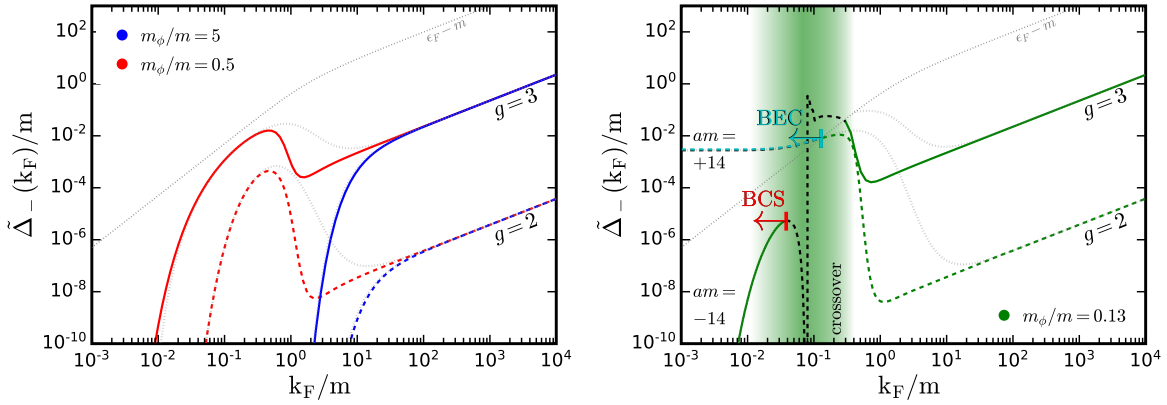


Figure 2: The solution to the gap equation including the effect of scalar density condensate is shown as function of dimensionless variable k_F/m . In the left panel we show the results for values of $g = 3$ (solid curves) and $g = 2$ (dashed curves). Blue (red) colored curves correspond to mediator mass $m_\phi = 5m$ ($m_\phi = 0.5m$). Dotted gray curves represent the solution to the gap equation with $m_* = m$. The right panel follows the same scheme as in the left panel but correspond to $m_\phi = 0.13m$. The green shaded region represents crossover regime.

Δ_i 's strongly depend on n_s though the effective fermion mass m_* , while the dependence of the scalar condensate on the gaps is mild, see below.

3.2 Quasi-particle dispersion relations

If the gaps are non-vanishing, it is tedious to derive the dispersion relations but the final result can be approximated by the following fairly simple expression

$$\epsilon_\pm^2 \approx (\omega \pm \mu)^2 + \left(\Delta_1 \pm \left(\frac{k}{\omega} \Delta_2 + \frac{m_*}{\omega} \Delta_3 \right) \right)^2, \quad (3)$$

where $-(+)$ corresponds to particle (anti-particle) excitations. We have assumed that the gaps are smaller than the chemical potential, which we expect to be the case in the BCS phase. As far as we could judge, our ansatz is consistent with results derived in (6), albeit with a distinct approach. It generalizes the results presented in (5), where the focus was only on the ultra-relativistic regime, $m = 0$ in which case only $\Delta_{1,2} \gg \Delta_3$ are relevant. This motivates the introduction of the new gap functions $\tilde{\Delta}_\pm = \Delta_1 \pm \left(\frac{k}{\omega} \Delta_2 + \frac{m_*}{\omega} \Delta_3 \right)$, and $\tilde{\kappa} = \frac{m_*}{\omega} \Delta_2 - \frac{k}{\omega} \Delta_3$.

Altogether, the gap functions and scalar condensate are thus determined by minimizing the free energy Ω , $\frac{\partial \Omega}{\partial \Delta_1} = 0$, $\frac{\partial \Omega}{\partial \Delta_2} = 0$, $\frac{\partial \Omega}{\partial \Delta_3} = 0$, $\frac{\partial \Omega}{\partial n_s} = 0$. Thus we obtain the following equations, which we have expressed using the $\tilde{\Delta}_\pm$ combination of gap functions,

$$n_s = \frac{-g^2}{m_\phi^2} \sum_{\eta=\pm} \int_0^\infty \frac{dk k^2}{2\pi^2} \left\{ \frac{m_*}{\omega_k} \left(\frac{\omega_k + \eta\mu}{\epsilon_\eta(k)} - 1 \right) - \eta \frac{k}{\omega_k} \frac{\tilde{\kappa}(k)}{\omega_k} \frac{\tilde{\Delta}_\eta(k)}{\epsilon_\eta(k)} \right\}, \quad (4)$$

$$\begin{aligned} \tilde{\Delta}_\pm(p) = & \frac{g^2}{32\pi^2} \sum_{\eta=\pm} \int_0^\infty dk \frac{k}{p} \left\{ \log \frac{m_\phi^2 + (p+k)^2}{m_\phi^2 + (p-k)^2} \mp \eta \frac{kp}{\omega_p \omega_k} \left(-2 + \frac{m_\phi^2 + k^2 + p^2}{2kp} \log \frac{m_\phi^2 + (p+k)^2}{m_\phi^2 + (p-k)^2} \right) \right. \\ & \left. \pm \eta \frac{m_*}{\omega_p \omega_k} \log \frac{m_\phi^2 + (p+k)^2}{m_\phi^2 + (p-k)^2} \right\} \frac{\tilde{\Delta}_\eta(k)}{\epsilon_\eta(k)}. \end{aligned} \quad (5)$$

3.3 Solutions to the gap equations

We present our findings in fig. 2, for various representative values of parameters of the theory, i.e. the Yukawa coupling and mediator mass. In the left panel we show the results for both heavy and moderately heavy mediator masses of $m_\phi = 5m$ (in blue) and $0.5m$ (in red), for $g = 3(2)$ in solid (dashed), respectively, including the effects of scalar density condensate. For the case of heavy mediator we recover the familiar BCS solution⁴⁾. In the case of the moderately heavy mediator, we obtain solutions which are parametrically different from the BCS case. We interpret this to be due to the fact that interactions are not point-like (or contact interaction) contrary to the standard BCS approximation.

In the right panel we present the results for light mediator with $m_\phi = 0.13m$ for the same values of couplings as in the left panel. As expected, the solution in the high density regime behaves parametrically as in the left panel. However, at low densities the situation could be drastically different from the left panel depending on the value of g . This is best understood through the low density phase diagram of the Yukawa theory put forward in fig. 1. For the case $g = 3$, corresponding to $\beta = 5.5$, we see that the system is in BCS phase at low densities. As we increase the density the system tends to be in a crossover regime at $k_F \approx |a^{-1}| = 0.07m$. In light of these observations, we can now understand the low density regions shown in the right panel of fig. 2. While not presented in fig. 1, we remark that for $g = 2$, at low densities, the system is in the BEC phase¹⁾. The solution yields the gap to be constant and much larger than $k_F^2/2m$. Although we get a solution for the gap, it does not represent a small perturbation to the Fermi surface, i.e. the chemical potential is no longer given by $\sqrt{k_F^2 + m^2}$ but should evolve towards the binding energy of the would-be DM molecules⁷⁾. Whereas, for $g = 3$, at low densities the gap is exponentially suppressed, indicative of the non-relativistic BCS phase. As we approach densities close to $k_F \approx |a^{-1}| = 0.07m$, the system goes to the crossover regime; for which we do not present any solution and it is shown as the shaded region. Regardless, at very large densities, the system becomes relativistic (this is further enhanced by the decrease of the effective mass) and, as the formation of true bound state becomes impossible, the system makes a transition to the relativistic BCS phase, a feature which seems to be novel.

4 Dark QCD

We now turn to the discussion of a nightmare scenario for DM, i.e. interacting only gravitationally with visible sector. The dark sector is governed by a dark $SU(3)$ symmetry akin to SM sector. The phenomenology of our scenarios is essentially determined by 3 parameters: f , M_π , ξ . The dark pion decay constant denoted by f is also approximately the temperature of the deconfinement phase transition. The mass of the baryon (pion) is $M_B \sim 10f$ (m_π), while ξ is the ratio of temperature of the dark sector to the visible one. The relic abundance formulae for both baryons and pions (when they are stable) impose a relation between these quantities so that ξ can be eliminated in terms of the other parameters as discussed in ref.²⁾. It is then useful to discuss these models in the plane (M_π, f) . We will discuss the phenomenology of our model in terms of these two parameters, determining ξ from the DM abundance constraint. The results of the phenomenological study of $SU(3)$ dark sector are summarized in figure 3. Remarkably we have shown that a simple gravitationally coupled dark QCD is already quite constrained through a combination of constraints from CMB, BBN, structure formation and self-interactions and can be further tested with future observations. The constraints depend on the initial temperature of the dark sector. If the pions are lighter than GeV they can make up all the DM and be as light as the mass scale currently tested with Ly- α forest observations. When the temperature of the dark sector is equal to the

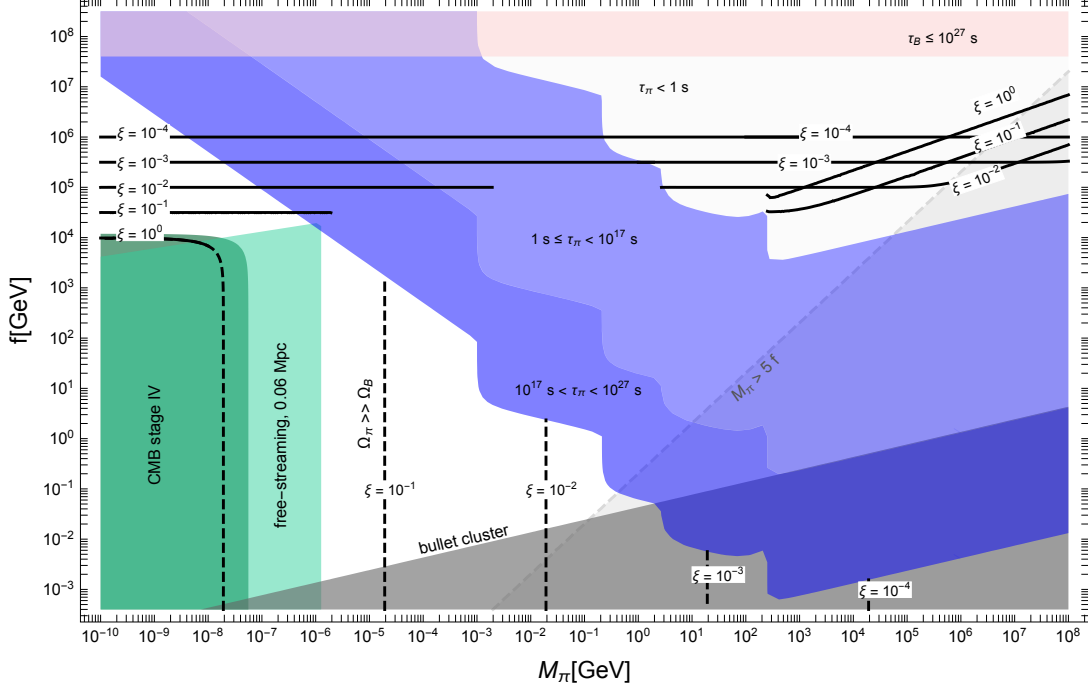


Figure 3: *Parameter space of (secluded) dark QCD as a function of M_π and f , with baryon mass fixed to $M_B = 10f$, $N_F = 3$ and $\Lambda_5 = 2.4 \times 10^{18}$ GeV. On the black solid isolines DM abundance is reproduced by dark baryons, while on the black dashed isolines by dark pions. Regions of instability are shaded in blue and pink. See ref ²⁾ for more details.*

SM pion DM would have mass around KeV and this is grossly excluded by structure formation. On the contrary, when the dark pions are heavier than the Higgs mass they decay before BBN but they can be sufficiently long lived to realize an early phase of matter domination. Upon decay to the SM such a phase ends with a large entropy injection into the SM plasma diluting DM abundance. This leads to baryon DM with mass 100 TeV or larger

5 Concluding remarks and prospects at colliders

Our visible sector is complex manifesting several phenomena. There is no reason for dark sector to be not as complex. In this work we have considered simple dark sector models, with minimal ingredients, and discussed possible emergent phenomena of condensed dark matter and cosmological phase transitions.

While the discussion of dark-QCD is truly a nightmare scenario with no possibility to probe such models at terrestrial experiments such as colliders, the story of condensed dark matter is more promising. So far, the only ingredients that we have discussed are related to DM self-interactions. However, notice that the Yukawa theory described by eq. (1) encompasses a scalar field. Such a field can be coupled to the standard model through the Higgs (e.g. $\lambda_{12}\phi^2|H|^2$) or through fermions (e.g. $g\phi\bar{t}t$). Therefore, this would represent a scenario akin to one of the simplified models widely considered in the literature. Typical strategies would include missing transverse energy searches or mono-jet searches. A detailed study that considers cosmological, astrophysical, and collider aspects is left for future work.

6 Acknowledgments

R.G. is supported by MIUR grant PRIN 2017FMJFMW and 2017L5W2PT.

References

1. R. Garani, M. H. G. Tytgat and J. Vandecasteele, Phys. Rev. D **106** (2022) no.11, 116003
2. R. Garani, M. Redi and A. Tesi, JHEP **12** (2021), 139
3. J. D. Walecka, Annals Phys. **83** (1974), 491-529
4. A. Schmitt, Lect. Notes Phys. **888** (2015), pp.1-155 2015
5. R. D. Pisarski and D. H. Rischke, Phys. Rev. D **60** (1999), 094013
6. D. Bailin and A. Love, Phys. Rept. **107** (1984), 325
7. P. Nozieres and S. Schmitt-Rink, J. Low Temp. Phys. **59** (1985), 195

Recent progress on the nonlocal power corrections to the inclusive penguin decays

$$\bar{B} \rightarrow X_s \gamma \text{ and } \bar{B} \rightarrow X_s \ell \ell$$

Michael Benzke

*Institute for Theoretical Physics, University Hamburg
Luruper Chaussee 149, D-26761 Hamburg, Germany*

Tobias Hurth

*PRISMA+ Cluster of Excellence and Institute for Physics (THEP)
Johannes Gutenberg University, D-55099 Mainz, Germany*

Abstract

We report on recent progress in the field of nonlocal (so-called resolved) contributions to the inclusive penguin decays which presently belong to the largest uncertainties in these inclusive decay modes. There is still a very large scale and a large charm mass dependence in the present leading order results which can in the future be decreased by including the α_s corrections.

1 Introduction

The inclusive decay modes $\bar{B} \rightarrow X_{s,d} \gamma$ and $\bar{B} \rightarrow X_{s,d} \ell^+ \ell^-$ are well known for being theoretically very clean modes of the indirect search for new physics via flavour observables and golden modes of the Belle-II experiment (for reviews see Refs. [1–3]). The Belle-II experiment at KEK will accumulate two orders of magnitude larger data samples than the B factories [4]. This will lead to a very high experimental precision in the penguin modes which has to be matched by the accuracy of theoretical predictions.

Within the heavy mass expansion (HME) these inclusive so-called penguin modes are dominated by the partonic contributions which can be calculated perturbatively and sub-leading contributions start at the quadratic level, $(\Lambda/m_b)^2$ only. However, it is well known that this operator product expansion breaks down in these inclusive modes if one considers operators beyond the leading ones. This breakdown manifests in nonlocal power corrections, also called resolved contributions. They are characterised by containing subprocesses in which the photon couples to light partons instead of connecting directly to the effective weak-interaction vertex [7].

These resolved contributions can be systematically calculated using soft-collinear effective theory (SCET). In the case of inclusive $\bar{B} \rightarrow X_s \gamma$ decay, all resolved contributions to $O(1/m_b)$ have been calculated some time ago [5–7]. Also, the analogous contributions to the inclusive $\bar{B} \rightarrow$

$X_{s,d}\ell^+\ell^-$ decays have been analysed to $O(1/m_b)$ [8,9]. In both cases an additional uncertainty of 4–5% was found, which represents the largest uncertainty in the prediction of the decay rate of $\bar{B} \rightarrow X_s\gamma$ [21] and of the low- q^2 observables of $\bar{B} \rightarrow X_{s,d}\ell^+\ell^-$ [11,12].

In both penguin decays there are four resolved contributions at $O(1/m_b)$, namely, from the interference terms $\mathcal{O}_{7\gamma} - \mathcal{O}_{8g}$, $\mathcal{O}_{8g} - \mathcal{O}_{8g}$, and $\mathcal{O}_1^c - \mathcal{O}_{7\gamma}$, but also from $\mathcal{O}_1^u - \mathcal{O}_{7\gamma}$.¹ The latter is CKM suppressed, however it was shown to vanish [5]. The $\mathcal{O}_1^c - \mathcal{O}_{7\gamma}$ piece is the largest contribution in both penguin decays. As was already noted in Refs. [8,9], there are subleading contributions due to the interference of $\mathcal{O}_{9,10}$ and \mathcal{O}_1^c at order $1/m_b^2$ which are numerically relevant due to the large ratio $C_{9,10}/C_{7\gamma}$ and which have to be added in the future.

Recently, a new theoretical input [18,19] allowed to reduce the impact of the $\mathcal{O}_1^c - \mathcal{O}_{7\gamma}$ contribution. However, in a more recent analysis of the $\mathcal{O}_1^c - \mathcal{O}_{7\gamma}$ resolved contribution a smaller reduction was found and additional uncertainties were identified [20]. We discuss the reasons for these discrepancies between the two analyses below [19,20]. In particular, a large scale dependence and also, a large charm mass dependence, were identified in the lowest order result of this resolved contribution, which calls for a systematic calculation of α_s corrections and renormalisation group (RG) summation [20]. For this task a factorisation formula for the subleading resolved corrections is needed which is valid to all orders in the strong coupling constant α_s . Here another new input was given in Ref. [13] where a previous failure of factorisation in specific resolved contributions was healed by using new refactorisation techniques [14–16].

We focus here on these two issues, namely the factorisation theorem for resolved contributions and the estimate of the $\mathcal{O}_1^c - \mathcal{O}_{7\gamma}$ contribution.

2 General properties of resolved contributions

The resolved contributions in the penguin decay $\bar{B} \rightarrow X_{s,d}\ell^+\ell^-$ were calculated in the presence of a cut in the hadronic mass M_X which is needed also at the Belle-II experiment in order to suppress huge background from double semi-leptonic decays. However it was shown [8,9] that the resolved contributions stay nonlocal when the hadronic cut is released. Therefore they represent an irreducible uncertainty. In addition it was shown that the support properties of the shape function imply that the resolved contributions (besides the $\mathcal{O}_{8g} - \mathcal{O}_{8g}$ one) are almost cut-independent. The analogous statements for the resolved contribution in the penguin decay $\bar{B} \rightarrow X_{s,d}\gamma$ are also valid when the photon energy cut is moved out of the endpoint region.

One finds a factorisation formula for the various contributions to the inclusive penguin decays [5]:²

$$d\Gamma(\bar{B} \rightarrow X_s\gamma, \ell^+\ell^-) = \sum_{n=0}^{\infty} \frac{1}{m_b^n} \sum_i H_i^{(n)} J_i^{(n)} \otimes S_i^{(n)} + \sum_{n=1}^{\infty} \frac{1}{m_b^n} \left[\sum_i H_i^{(n)} J_i^{(n)} \otimes S_i^{(n)} \otimes \bar{J}_i^{(n)} + \sum_i H_i^{(n)} J_i^{(n)} \otimes S_i^{(n)} \otimes \bar{J}_i^{(n)} \otimes \bar{J}_i^{(n)} \right]. \quad (2.1)$$

The first line describes the so-called direct contributions, while the second line contains the resolved contributions. The latter appear first only at the order $1/m_b$ in the heavy-quark expansion. Here hard functions $H_i^{(n)}$ describe physics at the high scale m_b . $J_i^{(n)}$ are the so-called jet functions which represent the physics of the hadronic final state X_s at the intermediate hard-collinear scale

¹For the definition of the operators the reader is guided to Ref. [9]

²The symbol \otimes denotes the convolution of the soft and jet functions.

$\sqrt{m_b \Lambda_{\text{QCD}}}$. The soft functions $S_i^{(n)}$, the so-called shape functions, parametrise the hadronic physics at the scale Λ_{QCD} . Within the resolved contributions we have new jet functions $\bar{J}_i^{(n)}$ due to the coupling of virtual photons with virtualities of order $\sqrt{m_b \Lambda_{\text{QCD}}}$ to light partons instead of the weak vertex directly.

However, the specific resolved $O_{8g} - O_{8g}$ contribution does not factorise because the convolution integral is UV divergent. The authors of Ref. [5] claimed that there is an essential difference between divergent convolution integrals in power-suppressed contributions of exclusive B decays and the divergent convolution integral in the present case, while the former were of IR origin, the latter divergence were of UV nature. Nevertheless, using a hard cut-off in the resolved contribution, the sum of direct and resolved $O_{8g} - O_{8g}$ contributions was shown to be scale and scheme independent at the lowest order. But the failure of factorisation did not allow for a consistent resummation of large logarithms. In a recent paper, the divergences in the resolved and in the direct contributions were identified as endpoint divergences. It was shown that also the divergence in the direct contribution can be traced back to a divergent convolution integral [13]. Recently new techniques [14–17] were presented in specific collider applications, which allow for an operator-level reshuffling of terms within the factorisation formula so that all endpoint divergences cancel out. This idea of refactorisation was now implemented in this flavour example of the resolved contributions which includes nonperturbative soft functions, the subleading shape functions, not present in collider applications [13]. A renormalised factorisation theorem on the operator level for these resolved contributions was derived to all orders in the strong coupling constant. This new result establishes the validity of the general factorisation theorem, given in Eq. 2.1, - also for the $O_{8g} - O_{8g}$ contributions. This theorem now allows for higher-order calculations of the resolved contributions and consistent summation of large logarithms [13].

3 Calculation of the resolved $\mathcal{O}_1^c - \mathcal{O}_{7\gamma}$ contribution to the penguin decay $\bar{B} \rightarrow X_s \gamma$

3.1 General strategy

Following the analysis in Ref. [21], the SM prediction for the branching ratio of $\mathcal{B}_{s\gamma}$ with a certain cut E_0 in the photon energy spectrum is based on the formula

$$\mathcal{B}(\bar{B} \rightarrow X_s \gamma)_{E_\gamma > E_0} = \mathcal{B}(\bar{B} \rightarrow X_c \ell \bar{\nu}) \left| \frac{V_{ts}^* V_{tb}}{V_{cb}} \right|^2 \frac{6\alpha_{em}}{\pi C} [P(E_0) + N(E_0)], \quad (3.2)$$

where the so-called semi-leptonic phase-space factor C is determined using the Heavy Quark Effective Theory (HQET) methods [23].

It is important to emphasise here that the perturbative contribution $P(E_0)$ is calculated using the local operators of the electroweak effective Hamiltonian, while the resolved contributions in the nonperturbative contribution $N(E_0)$ are calculated using SCET. Thus, scale choices and input parameters are in principle independent of each other in both contributions. One should keep this in mind when the uncertainty due to the resolved contributions relative to the perturbative decay rate is calculated. As in the original analysis in Ref. [5], the perturbative decay rate at leading order accuracy is used in the following. Moreover, the hard scale is chosen in this perturbative contribution.³ Because no α_s corrections or any RG improvements are considered in the calculation of the resolved power corrections, the scale choice is ambiguous. One first fixes

³The perturbative rate at higher orders is often calculated at a scale slightly smaller than the hard scale for other reasons, namely for the stabilisation of the charm mass renormalisation dependence (see for example Ref. [21])

the Wilson coefficients in the resolved contribution at the hard scale, then one varies the scale of the Wilson coefficients in the resolved contributions between the hard and the hard-collinear scale to make the scale dependence of the resolved contributions manifest.

In the following the focus will be on the most important contribution due to the interference of $\mathcal{O}_1^c - \mathcal{O}_{7\gamma}$. Using the original notation of Ref. [5] one can write this resolved contribution normalised to the perturbative leading order result as

$$\mathcal{F}_{b \rightarrow s\gamma}^{17} = \frac{C_1(\mu) C_{7\gamma}(\mu)}{(C_{7\gamma}(\mu_{\text{OPE}}))^2} \frac{\Lambda_{17}(m_c^2/m_b, \mu)}{m_b}, \quad (3.3)$$

where μ_{OPE} denotes the perturbative scale, μ the scale within the resolved contribution. At subleading power one finds [5]:

$$\Lambda_{17}\left(\frac{m_c^2}{m_b}, \mu\right) = e_c \text{Re} \int_{-\infty}^{\infty} \frac{d\omega_1}{\omega_1} \left[1 - F\left(\frac{m_c^2 - i\varepsilon}{m_b \omega_1}\right) + \frac{m_b \omega_1}{12m_c^2} \right] h_{17}(\omega_1, \mu), \quad (3.4)$$

with the penguin function $F(x) = 4x \arctan^2(1/\sqrt{4x-1})$. The shape function h_{17} is given by the following HQET matrix element:

$$h_{17}(\omega_1, \mu) = \int \frac{dr}{2\pi} e^{-i\omega_1 r} \frac{\langle B | \bar{h}(0) \not{n} i \gamma_{\alpha}^{\perp} \bar{n}_{\beta} g G^{\alpha\beta}(r\bar{n}) h(0) | B \rangle}{2M_B}, \quad (3.5)$$

where \bar{n} is one of the light-cone vectors, while h and G are the heavy quark and gluon field, respectively. Soft Wilson lines are suppressed in the notation. The variable ω_1 corresponds to the soft gluon momentum.

The general strategy to estimate the convolution integral of the perturbative jet functions and the nonperturbative shape function h_{17} is the derivation of general properties of the shape functions. One shows for example PT invariance in this case, which implies that the matrix element is real. Moreover, one finds moments of this HQET matrix element. While the zero-moment was already known in the first analyses of the resolved contributions, the second moment was recently derived using HQET techniques; moreover rough dimensional estimates of the higher order moments were proposed [18, 19]. One can also naturally assume that the support properties and the values of the soft shape function are within the hadronic range.

Besides these general properties and the estimates on the moments, nothing further is known about the structure of the subleading shape functions. Therefore, the two new analyses of the resolved contributions [19, 20] follow here exactly the same strategy; they use a complete set of basis functions, namely the Hermite functions in order to make a systematic analysis of all possible model functions fulfilling the known properties of the shape function. This systematic approach to the shape functions was already used in several previous analyses [24–26]. Obviously this systematic approach allows to avoid any prejudice regarding the unknown functional form of the shape functions and, thus, leads to a valid estimate of the resolved contribution. Any additional assumption calls for a clear justification.

3.2 Numerical results

In both the new analyses [19, 20], the maximum value of the convolution integral between jet and shape functions was found for Hermite polynomials of degree six. Higher degree polynomials do not lead to larger values. Both analyses found a significant reduction in the values of the resolved contributions due to the new input of the second moment of the shape function.

The final result for the resolved $\mathcal{O}_1^c - \mathcal{O}_{7\gamma}$ contribution in Ref. [20] is:

$$\mathcal{F}_{b \rightarrow s\gamma}^{17} \in [-0.4\%, 4.7\%], \quad (3.6)$$

which represents a large reduction compared to the original estimate in Ref. [5]. Some comments are in order:

- In the present result no α_s corrections are included and no RG improvements are done. Thus, this implies a large scale dependence in our results. In the leading order result the only scale is in the Wilson coefficients representing the hard function. Varying the LO Wilson coefficients $C_1(\mu)C_{7\gamma}(\mu)$ in the resolved contribution from the hard scale to the hard-collinear scale increases the result by more than 40%. This represents an additional uncertainty of the result **not** included in Eq. 3.6.
- The result in Eq. 3.6 includes a large kinematical $1/m_b^2$ contribution from the $\mathcal{O}_1^c - \mathcal{O}_{7\gamma}$ interference. One can show by inspection of all resolved $1/m_b^2$ contributions that this kinematical $1/m_b^2$ term is the only one with the same shape function of the order $1/m_b$ as in the $1/m_b^1$ term. All other resolved $1/m_b^2$ contributions in the interference of $\mathcal{O}_1^c - \mathcal{O}_{7\gamma}$ include shape functions of the order $1/m_b^2$. Those terms are not calculated yet. Therefore, the significantly large $1/m_b^2$ term due to kinematical factors in the $\mathcal{O}_1^c - \mathcal{O}_{7\gamma}$ term was included in the result 3.6 as conservative estimate of those higher order resolved contributions. This $1/m_b^2$ term was already included in the original analysis in Ref. [5], where it was also shown that other $1/m_b^2$ contributions due to the interference of $\mathcal{O}_1^c - \mathcal{O}_{8g}$ and $\mathcal{O}_1^c - \mathcal{O}_1$ are numerically negligible.

The authors of the new analysis in Ref. [19] find a much larger reduction and end up with ⁴

$$\mathcal{F}_{b \rightarrow s\gamma}^{17} \in [-0.4\%, 1.9\%], \quad (3.7)$$

There are two main reasons for this difference with the result of Ref. [5], given in Eq. 3.6:

- The charm mass dependency originates from the anti-hard-collinear jet function $\bar{J}_i^{(n)}$ represented by the charm loop with a soft gluon emission. Therefore it is appropriate to use the running charm mass at the hard-collinear scale $m_c^{\text{MS}}(\mu_{\text{hc}})$. The charm mass ambiguity of the charm mass was made manifest by the variation of the hard-collinear scale $\mu_{\text{hc}} \sim \sqrt{m_b \Lambda_{\text{QCD}}}$ from 1.3 GeV to 1.7 GeV within the recent analysis in Ref. [5]. Using the present PDG value of the charm mass being $m_c^{\text{MS}}(m_c) = (1.27 \pm 0.02)$ GeV and using three-loop running with $\alpha_s(m_c) = 0.395$ and $\alpha_s(m_Z) = 0.1185$ down to the hard-collinear scale, one finds $m_c^{\text{MS}}(1.5 \text{ GeV}) = 1.19$ GeV as central value at 1.5 GeV. The change of the hard-collinear scale indicated above then leads to [5]

$$1.14 \text{ GeV} \leq m_c \leq 1.26 \text{ GeV}. \quad (3.8)$$

The parametric errors of $m_c^{\text{MS}}(m_c)$ and α_s are neglected in view of the larger uncertainty due to the change of the hard-collinear scale μ_{hc} .

In the recent analysis in Ref. [19], two-loop running leads to the central value $m_c^{\text{MS}}(1.5 \text{ GeV}) =$

⁴We translated this result to our scale fixing. The authors of Ref. [19] find $\mathcal{F}_{b \rightarrow s\gamma}^{17} \in [-0.3\%, 1.6\%]$ in their paper using the hard-collinear scale in the resolved and the perturbative contribution instead of the hard scale.

(1.20 + 0.03) GeV. The parametric uncertainties, but no change of the hard-collinear scale is taken into account. One then finds the following variation of the charm mass

$$1.17 \text{ GeV} \leq m_c \leq 1.23 \text{ GeV}, \quad (3.9)$$

which was used in the analysis in Ref. [19], but it is unnaturally small and, thus, represents an underestimation of the charm mass dependence.

- The second reason is that the authors of Ref. [19] did not include any estimate for the $1/m_b^2$ corrections. In view of the fact that the only resolved $1/m_b^2$ term with the same shape function as in the $1/m_b$ term is very large, this may lead to a further underestimation of the overall uncertainty.

Finally, it is important to note that the local Voloshin term is subtracted from the resolved contribution $\mathcal{F}_{b \rightarrow s\gamma}^{17}$. This has been done in all analyses of this specific resolved contribution to the $\bar{B} \rightarrow X_s \gamma$ decay rate. Therefore this nonperturbative contribution has still to be added to the decay rate. It is given by $\Lambda_{17}^{\text{Voloshin}} = (-1)(m_b \lambda_2)/(9m_c^2)$ and corresponds to

$$\mathcal{F}_{b \rightarrow s\gamma}^{\text{Voloshin}} = -\frac{C_1(\mu) C_{7\gamma}(\mu) \lambda_2}{(C_{7\gamma}(\mu_{\text{OPE}}))^2 9 m_c^2} = +3.3\%, \quad (3.10)$$

If one neglects the shape function effects and treats the charm quark mass as heavy, one can derive the local Voloshin term from the resolved contribution $\mathcal{O}_1^c - \mathcal{O}_{7\gamma}$ (see section 3.2 of Ref. [9] for more details). But the local Voloshin term, derived in Refs. [27–30], does not account for the complete resolved contribution as one can read off from the additional contribution given in Eq. 3.6.

We close this progress report by another recent improvement of estimates of the resolved contribution. Based on Ref. [34] an estimation of the resolved contribution to the \mathcal{F}^{78} was offered in Ref. [5] using experimental data on Δ_{0-} of the isospin asymmetry of inclusive neutral and charged $B \rightarrow X_s \gamma$ decay [31, 32]. In the recent analysis [19], the authors derived new bounds by taking into account a new Belle measurement of Δ_{0-} [33], which leads to the experimental determination of \mathcal{F}^{78} being the same order of magnitude as the determination using the vacuum insertion approximation (VIA) [5] but includes the prospect to be improved by more precise data.

References

1. T. Hurth, “Present status of inclusive rare B decays,” *Rev. Mod. Phys.* **75** (2003) 1159 [arXiv:hep-ph/0212304].
2. T. Hurth and M. Nakao, “Radiative and Electroweak Penguin Decays of B Mesons,” *Ann. Rev. Nucl. Part. Sci.* **60** (2010) 645 [arXiv:1005.1224 [hep-ph]].
3. T. Hurth and F. Mahmoudi, “New physics search with flavour in the LHC era,” *Rev. Mod. Phys.* **85** (2013) 795 [arXiv:1211.6453 [hep-ph]].
4. E. Kou *et al.* [Belle-II], “The Belle II Physics Book,” *PTEP* **2019** (2019) no.12, 123C01 [erratum: *PTEP* **2020** (2020) no.2, 029201] [arXiv:1808.10567 [hep-ex]].

5. M. Benzke, S. J. Lee, M. Neubert and G. Paz, “Factorization at Subleading Power and Irreducible Uncertainties in $\bar{B} \rightarrow X_s \gamma$ Decay,” JHEP **1008** (2010) 099 [arXiv:1003.5012 [hep-ph]].
6. M. Benzke, S. J. Lee, M. Neubert and G. Paz, “Long-Distance Dominance of the CP Asymmetry in $\bar{B} \rightarrow X_{s,d} \gamma$ Decays,” Phys. Rev. Lett. **106** (2011) 141801 [arXiv:1012.3167 [hep-ph]].
7. S. J. Lee, M. Neubert and G. Paz, “Enhanced Non-local Power Corrections to the $\bar{B} \rightarrow X_s \gamma$ Decay Rate,” Phys. Rev. D **75**, 114005 (2007) [arXiv:hep-ph/0609224].
8. T. Hurth, M. Fickinger, S. Turczyk and M. Benzke, “Resolved Power Corrections to the Inclusive Decay $\bar{B} \rightarrow X_s \ell^+ \ell^-$,” Nucl. Part. Phys. Proc. **285-286** (2017) 57 [arXiv:1711.01162 [hep-ph]].
9. M. Benzke, T. Hurth and S. Turczyk, “Subleading power factorization in $\bar{B} \rightarrow X_s \ell^+ \ell^-$,” JHEP **1710** (2017) 031 [arXiv:1705.10366 [hep-ph]].
10. M. Misiak *et al.*, “Updated NNLO QCD predictions for the weak radiative B -meson decays,” Phys. Rev. Lett. **114** (2015) no.22, 221801 [arXiv:1503.01789 [hep-ph]].
11. T. Huber, T. Hurth and E. Lunghi, “Inclusive $\bar{B} \rightarrow X_s \ell^+ \ell^-$: complete angular analysis and a thorough study of collinear photons,” JHEP **1506** (2015) 176 [arXiv:1503.04849 [hep-ph]].
12. T. Huber, T. Hurth, J. Jenkins, E. Lunghi, Q. Qin and K. K. Vos, “Long distance effects in inclusive rare B decays and phenomenology of $\bar{B} \rightarrow X_d \ell^+ \ell^-$,” JHEP **1910** (2019) 228 [arXiv:1908.07507 [hep-ph]].
13. T. Hurth and R. Szafron, “Refactorisation in subleading $\bar{B} \rightarrow X_s \gamma$,” [arXiv:2301.01739 [hep-ph]].
14. Z. L. Liu and M. Neubert, “Factorization at subleading power and endpoint-divergent convolutions in $h \rightarrow \gamma \gamma$ decay,” JHEP **04**, 033 (2020) [arXiv:1912.08818 [hep-ph]].
15. Z. L. Liu, B. Mecaj, M. Neubert and X. Wang, “Factorization at subleading power and endpoint divergences in $h \rightarrow \gamma \gamma$ decay. Part II. Renormalization and scale evolution,” JHEP **01**, 077 (2021) [arXiv:2009.06779 [hep-ph]].
16. M. Beneke, M. Garny, S. Jaskiewicz, J. Strohm, R. Szafron, L. Vernazza and J. Wang, “Next-to-leading power endpoint factorization and resummation for off-diagonal “gluon” thrust,” JHEP **07**, 144 (2022) [arXiv:2205.04479 [hep-ph]].
17. G. Bell, P. Böer and T. Feldmann, “Muon-electron backward scattering: a prime example for endpoint singularities in SCET,” JHEP **09** (2022), 183 [arXiv:2205.06021 [hep-ph]].
18. A. Gunawardana and G. Paz, “On HQET and NRQCD Operators of Dimension 8 and Above,” JHEP **1707** (2017) 137 [arXiv:1702.08904 [hep-ph]].
19. A. Gunawardana and G. Paz, “Reevaluating Uncertainties in $\bar{B} \rightarrow X_s \gamma$ Decay,” arXiv:1908.02812 [hep-ph].
20. M. Benzke and T. Hurth, “Resolved $1/m_b$ contributions to $\bar{B} \rightarrow X_{s,d} \ell^+ \ell^-$ and $\bar{B} \rightarrow X_s \gamma$,” Phys. Rev. D **102**, 114024 (2020) [arXiv:2006.00624 [hep-ph]].
21. M. Misiak *et al.*, “Updated NNLO QCD predictions for the weak radiative B -meson decays,” Phys. Rev. Lett. **114** (2015) 221801 [arXiv:1503.01789].

22. M. Czakon, P. Fiedler, T. Huber, M. Misiak, T. Schutzmeier and M. Steinhauser, “The $(Q_7, Q_{1,2})$ contribution to $\bar{B} \rightarrow X_s \gamma$ at $\mathcal{O}(\alpha_s^2)$,” JHEP **1504** (2015) 168 [arXiv:1503.01791].
23. A. Alberti, P. Gambino, K. J. Healey and S. Nandi, “Precision Determination of the Cabibbo-Kobayashi-Maskawa Element V_{cb} ,” Phys. Rev. Lett. **114** (2015) 061802 [arXiv:1411.6560].
24. Z. Ligeti, I. W. Stewart and F. J. Tackmann, “Treating the b quark distribution function with reliable uncertainties,” Phys. Rev. D **78** (2008), 114014 [arXiv:0807.1926 [hep-ph]].
25. K. S. M. Lee and F. J. Tackmann, “Nonperturbative m_X cut effects in $B \rightarrow X_s l^+ l^-$ observables,” Phys. Rev. D **79** (2009), 114021 [arXiv:0812.0001 [hep-ph]].
26. F. U. Bernlochner *et al.* [SIMBA], “Precision Global Determination of the $B \rightarrow X_s \gamma$ Decay Rate,” [arXiv:2007.04320 [hep-ph]].
27. M. B. Voloshin, “Large $\mathcal{O}(m_c^{-2})$ non-perturbative correction to the inclusive rate of the decay $B \rightarrow X_s \gamma$,” Phys. Lett. B **397**, 275 (1997) [arXiv:hep-ph/9612483].
28. Z. Ligeti, L. Randall and M. B. Wise, “Comment on non-perturbative effects in $\bar{B} \rightarrow X_s \gamma$,” Phys. Lett. B **402**, 178 (1997) [arXiv:hep-ph/9702322].
29. A. K. Grant, A. G. Morgan, S. Nussinov and R. D. Peccei, “Comment on non-perturbative $\mathcal{O}(1/m_c^2)$ corrections to $\Gamma(\bar{B} \rightarrow X_s \gamma)$,” Phys. Rev. D **56**, 3151 (1997) [arXiv:hep-ph/9702380].
30. G. Buchalla, G. Isidori and S. J. Rey, “Corrections of order $\Lambda_{\text{QCD}}^2/m_c^2$ to inclusive rare B decays,” Nucl. Phys. B **511**, 594 (1998) [arXiv:hep-ph/9705253].
31. B. Aubert *et al.* [BaBar Collaboration], “Measurements of the $B \rightarrow X_s \gamma$ branching fraction and photon spectrum from a sum of exclusive final states,” Phys. Rev. D **72**, 052004 (2005) [arXiv:hep-ex/0508004].
32. B. Aubert *et al.* [BaBar Collaboration], “Measurement of the $B \rightarrow X_s \gamma$ branching fraction and photon energy spectrum using the recoil method,” Phys. Rev. D **77**, 051103 (2008) [arXiv:0711.4889 [hep-ex]].
33. S. Watanuki *et al.* [Belle Collaboration], “Measurements of isospin asymmetry and difference of direct CP asymmetries in inclusive $B \rightarrow X_s \gamma$ decays,” Phys. Rev. D **99**, no. 3, 032012 (2019) [arXiv:1807.04236 [hep-ex]].
34. M. Misiak, “B-bar \rightarrow X(s) gamma: Current Status,” Acta Phys. Polon. B **40** (2009), 2987-2996 [arXiv:0911.1651 [hep-ph]].

PRECISION MEASUREMENT OF THE W BOSON MASS: STATUS AND PROSPECTS

Lorenzo Bianchini

Dipartimento di Fisica “E. Fermi”, Università di Pisa

Abstract

In this talk, I will review the current status of the direct measurement of the W boson mass, with particular emphasis on recent results and opportunities from future measurements.

1 Introduction

A precision measurement of the W boson mass (m_W) plays an important role in the test of the electroweak theory ¹): as of today, the indirect determination of m_W is more precise (by a factor of about two) than its direct measurement ²), so that even a twofold reduction in the experimental uncertainty, albeit challenging from an experimental standpoint, would have a non-negligible impact on the global fit of the electroweak theory.

It is well-known that the SM tree-level prediction of m_W can be expressed in terms of just three parameters, which can be chosen to be e.g. the well-measured values of the Fermi constant (G_μ), of the electromagnetic running coupling at the Z mass ($\alpha(m_Z)$), and of the Z boson mass itself (m_Z). Radiative corrections to the tree-level prediction introduce a further dependence on the Higgs boson and on the top-quark masses, overall shifting the predicted value by about 500 MeV. Overall, the SM prediction has a relative precision of 10^{-4} , where the dominant sources of uncertainty come from missing higher-order EWK corrections (~ 4 MeV) and the limited precision of the direct top-quark and Z boson mass measurements ¹). However, contributions from new particles of a yet-unknown physics sector, where new interactions might contribute to the breaking of the custodial symmetry (e.g. new Higgs multiplets with $T > \frac{1}{2}$, new non-degenerate $SU(2)$ -doublets, extra $U(1)'$ symmetries, etc..) could, at least in principle, modify the SM prediction.

Recently, the CDF Collaboration has released a new measurement of m_W which improves over their previous result, and happens to be largely inconsistent with the SM prediction of m_W , as well as in substantial tension with other existing measurements at the LHC ³⁾. The current situation is well illustrated by Figure 1.

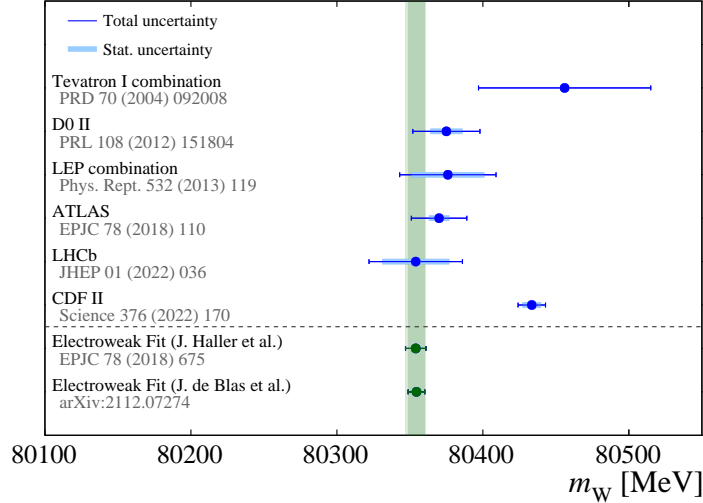


Figure 1: *Status of W boson mass measurements* ⁴⁾.

2 W boson production at colliders

Differently from other short-lived particles, m_W cannot be reconstructed from the full decay chain of W bosons, being the neutrino from the decay undetectable and the initial velocity of the decaying boson unknown on an event-by-event basis. This leads to a dependence of any possible mass estimator on the mechanism of production and decay of W bosons. The latter can be however calculated in pQCD: perturbative calculations, jointly with modern predictions of the proton PDFs, an improved treatment of soft and collinear gluon radiation, and the inclusion of higher-order EWK corrections, can now achieve an outstanding level of accuracy ⁵⁾.

Interestingly, the two accelerators which can nowadays measure m_W (Tevatron and LHC) differ enough in terms of both the initial-state and the environmental conditions so that common sources of systematic uncertainty affect the two measurements usually at different levels and with different correlation schemes. In particular, while uncertainties on the modeling of the hard-scattering event can be assumed uncorrelated between the two experiments because of the substantially different center-of-mass energy and flavour composition of the initial-state, the PDFs should be the same (if PDFs are really meant to provide a universal description of the proton).

While the result of a measurement should be code-independent (provided that any of the codes in use is bug-free and that the quoted uncertainties provide the right coverage), recent studies have shown that this is not always the case, and special care should be put to understand the impact of specific codes to the central values as well as to the uncertainty budget quoted by the experiments. Finally, the necessity to tune the QCD prediction to match the well-measured kinematic distributions of Z decays (a

practice which is common to all existing measurements) represent a potential source of common “bias”, the size of which has been estimated on different grounds by each experiment, but without a conclusive theoretical understanding.

In the following, the most recent measurements of m_W at hadron colliders will be shortly reviewed in a comparative way.

2.1 CDF-II

The recent measurement by CDF-II ³⁾ is based on their full data sample of electron and muon events. The analysis relies on MC-based templates of three kinematic quantities. These templates are obtained by using a rather old generator (**ResBosP**) and PDF set (**CTEQ6M**). A correction to a more modern PDF set (**NNPDF3.1**) is accomplished by shifting the measured value of m_W based on a theory-to-theory comparison. Non-perturbative parameters of **ResBosP** are tuned to match the measured q_T spectrum in Z events. A custom simulation of the CDF detector is used to allow for a fast generation of events. Based on the comparison between measured and simulated mass distributions of reconstructed J/Ψ , $\Upsilon(1s)$ and Z events, the absolute momentum scale of charged-particle tracks in data is adjusted by a relatively large (and still unexplained) factor, amounting to a relative correction of about 10^{-3} . The surprisingly large value of this correction, as well as the validity of the linear extrapolation assumed to correct the momentum scale over a broad range of values, has been extensively debated within the community. The final uncertainty on m_W is estimated to be 9 MeV.

2.2 D0

The latest D0 ⁶⁾ result is based on the electron-channel only. It uses the **ResBosCP** program interfaced to the **CTEQ6.6** PDF set. Non-perturbative parameters of **ResBosCP** are tuned to the measured Z data. The uncertainty on m_W is estimated to be 23 MeV. Differently from CDF, the D0 collaboration won't be able to update its 2012 result on a larger sample.

2.3 ATLAS

The ATLAS Collaboration has published a measurement of m_W based on their 7 TeV data ⁷⁾. The physics modeling is based on the **Powheg** event generator interfaced to **Pythia8** and the **CT10** PDF set. The helicity cross sections are corrected differentially in rapidity and transverse momentum of the W boson, as to match the predictions of **DYNNLO**, which has higher-order accuracy on the angular coefficients. Non-perturbative parameters of **Pythia** are tuned to the measured Z p_T spectrum. The absolute momentum and energy scale of simulated muons and electrons is corrected to match the mass distributions measured in Z decays. A total of 28 statistically independent channels are combined to give an overall uncertainty of about 19 MeV.

2.4 LHCb

The LHCb Collaborations has published a measurement of m_W based on a sub-sample of their Run2 data ⁸⁾. The physics modeling is based on the **Powheg** event generator interfaced to **Pythia8** and the **NNPDF3.1** set. The **DYTurbo** program is used to correct the angular coefficients. Non-perturbative parameters of **Pythia** are profiled by including the ϕ^* ⁹⁾ spectrum measured in $Z \rightarrow \ell\ell$ events into a combined fit with the data sensitive to m_W , which is chosen to be the distribution of q/p_T (where q is

the charge of the muon). A nuisance parameter which rescales the overall value of the A_3 coefficient ¹⁰⁾ is included in the fit. The total uncertainty on m_W is estimated to be 32 MeV.

2.5 Towards a combined result

The use of different codes and prescriptions to tame modeling uncertainties poses a non-trivial problem in sight of a common interpretation of the results. A joint effort between Tevatron and LHC collaborations has been addressing this problem ⁵⁾. The proposed solution is to compute δm_W shifts to the published values which effectively update (or correct) to more recent codes. This solution allows to treat the various measurements on the same footing, paving the way towards a proper combination and assessment of a combined theory uncertainty. Interestingly, a non-negligible, i.e. $O(10)$ MeV, impact of using an outdated version of their generator (`ResBos1`) instead of a more recent one (`ResBos2`) has been highlighted in the context of the D0 measurement.

3 Tevatron vs LHC

It is instructive to compare the breakdown of the systematic uncertainties affecting the Tevatron and LHC measurements. Considering just the two best measurements from each collider ^{3, 7)}, which happen to have very similar statistical uncertainty, one can easily see that the LHC measurements are affected on average by larger systematic uncertainty both of modeling and experimental origin. While the latter can be ascribed to the cleaner environment at the Tevatron (e.g. lower pile-up and \sqrt{s} and less material budget in the tracking volume), the variability in the estimation of modeling uncertainties can be only in part accounted for by environmental effects: the largest source of difference still arises from specific choices made by each collaboration in terms of code and correlation schemes between theory nuisance parameters. For example, if the LHC Collaboration had chosen to apply the full-NLO scale variation uncertainty on A_3 instead of fitting a unique freely-floating parameter, the error budget on m_W from just this parameter would have increased from 9 MeV to about 30 MeV ⁸⁾. Likewise, if a same nuisance parameter were chosen to modify the input value of α_s in the `Pythia` generator of W and Z events, instead of two independent parameters, the shift on the measured value of m_W would have been of about 40 MeV, which is larger than the overall uncertainty quoted by the LHCb measurement. Similar features are reported by the ATLAS Collaboration ⁷⁾.

While most of these choices are claimed to improve the overall agreement between data and simulation in either the signal region or in closely related calibration regions, the tuning of model parameters in the context of a shape-based analysis like this one should be taken with some caution, since tuning come with the risk of hiding intrinsic limitations of the models.

The implication of the CDF-II choice of using a rather old code is still under investigation and no conclusive statement has been made yet. However, from all studies to date, ⁵⁾ there doesn't seem to be an easy way to change the modeling in the recent CDF measurement such to reconcile it with the SM expectation.

In the near future, we will hopefully get new insights on the impact of mixed QCD-EWK corrections ¹¹⁾ (so far neglected by all codes) and on the flavor-dependence of the non-perturbative corrections ¹²⁾.

4 The role of CMS

The CMS Collaboration has already given proof of its capability to measure m_W with competitive precision thanks to an end-to-end measurement of m_Z in the so-called W -like topology ¹³⁾, i.e. in fully reconstructed di-lepton events where one lepton at the time is treated as a neutrino. Since then, the guideline followed by CMS has been to reduce model-uncertainties by means of more (and more-differential) data and the use of state-of-the-art developments in pQCD calculations. Along this road, the measurement of the rapidity cross section of W^\pm at 13 TeV for two helicity states stands up as an intermediate milestone towards m_W ¹⁴⁾. Indeed, this measurement has proved that a strong *in situ* constraint of the PDFs is possible with just a tiny fraction of the Run2 data collected by CMS. The measurement of m_W from the same data was precluded by the lack of a precise enough calibration of the muon momentum scale and by limitations of the MC samples available at that time.

5 Future measurements

The planned Phase2 upgrades of the ATLAS and CMS experiments offer the potential to improve on some of the weak points affecting the present measurements. In particular, an extended low-PU run during the HL-LHC era (or earlier, during the Run3) might provide a powerful data sample to perform a precise measurement of m_W , especially if joined with the extended pseudo-rapidity coverage offered by the upgraded tracking detectors and improvements on the theory and PDF side ¹⁵⁾.

Finally, one should not give up on the idea of using the larger-than-ever statistical power of the high-PU data collected during the Run2 and 3 of the LHC. To this aim, however, something has to be done to evade the model-dependence of the traditional approach. For example, the idea behind the ASYMOW project ¹⁶⁾ is to replace the prediction of a particular code by a theory-agnostic QCD model, which can be e.g. written in terms of double-differential helicity cross sections:

$$\frac{\Delta^2 \sigma}{\Delta p_T^\ell \Delta \eta^\ell} = \sum_{\Delta q_T, \Delta |y|} \frac{\Delta^2 \sigma_{-1}}{\Delta q_T, \Delta |y|} \left[T_{-1}(p_T^\ell, \eta^\ell; m_W) + \sum_{k=0..4} A_{k, \Delta q_T, \Delta |y|} T_k(p_T^\ell, \eta^\ell; m_W) \right], \quad (1)$$

where T_k are normalized templates defined in a narrow bin of q_T and $|y|$ of the W boson, and as such virtually independent from the QCD model used to build them. The dependence of the templates on m_W is parametric. Within this framework, m_W and the production model can be disentangled at the price of an increased statistical uncertainty on the former. We remark that a (large) MC sample is still needed to account for QED FSR and detector effects. Preliminary studies show that the data collected at the Run2 and Run3 of the LHC should be enough to achieve a statistical-only uncertainty of about 6 MeV from this new method.

Finally, it should be mentioned that the ultimate precision on m_W is expected to come from the next generation of lepton-lepton colliders. For example, with a two-year run at the WW production threshold, FCC-ee is expected to achieve a sub-MeV precision on m_W ¹⁷⁾.

6 Conclusions

The recent result by CDF has turned a tempting tension into a stunning anomaly. While BSM interpretations of the observed excess seem feasible, the inconsistency between this measurement and the LHC ($\approx 3.5\sigma$) or D0 measurement ($\sim 2.5\sigma$) still deserves some deeper understanding. The CMS Collaboration has now the potential to corroborate or exclude the CDF-II result. Yet, the modeling of W production

remains the bottleneck of this analysis. Although a major effort of the theory community is ongoing to tackle this problem, it's likely that only more data in the future will be able to set a final word.

7 Acknowledgements

The participation to this very interesting and stimulating conference has been partly supported by a project that received funding from the European Research Council (ERC) under the European Unions Horizon 2020 research and innovation programme (Grant agreement No. 101001205).

References

1. J. Haller et al. (GFitter Collaboration), *Eur. Phys. J. C* **78**, 675 (2018).
2. R. L. Workman et al. (Particle Data Group), *Prog. Theor. Exp. Phys.* **2022**, 083C01 (2022).
3. CDF Collaboration, *Science* **376**, 6589 (2022).
4. LHCb-FIGURE-2022-003 available through <https://cds.cern.ch/>.
5. The LHC-TeVatron W-boson mass combination working group, CERN-LPCC-2022-06, FERMILAB-TM-2779-V.
6. D0 Collaboration, *Phys. Rev. D* **89**, 012005 (2014) .
7. ATLAS Collaboration, *Eur. Phys. J. C* **78**, 110 (2018).
8. LHCb Collaboration, *JHEP* **01**, 036 (2022).
9. Banfi et al., *Eur. Phys. J. C* **71** 1600 (2011).
10. E. Mirkes, *Nucl. Phys. B* **387** 3 (1992).
11. A. Behring et al., *Phys. Rev. D* **103**, 113002 (2021).
12. G. Bozzi, A. Signori, *AHEP* 2526897 (2019).
13. The CMS Collaboration, CMS-PAS-SMP-14-007 (2014).
14. The CMS Collaboration, *Phys. Rev. D* **102**, 092012 (2020).
15. The ATLAS Collaboration, ATL-PHYS-PUB-2018-026 (2018).
16. <https://cordis.europa.eu/project/id/101001205>
17. A. Abada et al., *Eur. Phys. J. C* **79**, 474 (2019)